

# **Ion sculpting of Cu(001)**

**Mikhail Mikhaylovich Ovsyanko**

Samenstelling promotiecommissie:

Rector Magnificus - voorzitter

Prof. dr. ir. Bene Poelsema

Dr. ir. H. Wormeester

Prof. dr. T. Michely

Prof. dr. ir. R. Hoekstra

Prof. dr. ir. J. Huskens

Prof. dr. ir. H.J.W. Zandvliet

This thesis is the result of work performed in the MESA+ Research Institute, Solid State Physics group, Faculty of Science and Technology at the University of Twente, The Netherlands.

This work has been funded by the "Stichting Fundamenteel Onderzoek der Materie" (FOM).

M.M. Ovsyanko  
Ion sculpting of Cu(001)  
ISBN 90-365-2307-9

Published by the Solid State Physics Group, University of Twente  
Printed in the Netherlands by PrintPartners Ipskamp B.V., Enschede

Copyright © 2006 by M.M. Ovsyanko

All rights reserved. No part of the material protected by this copyright notice may be reproduced or utilized in any form or by any means, electronic or mechanical, including photocopying, recording or by any information storage and retrieval system, without the prior permission of the author.

Author email: `m.m.ovsyanko@alumnus.utwente.nl`

Cover: "Art in a stone", Photo by A.Galey.

# Ion sculpting of Cu(001)

PROEFSCHRIFT

ter verkrijging van  
de graad van doctor aan de Universiteit Twente,  
op gezag van de rector magnificus,  
prof. dr. W.H.M. Zijm,  
volgens besluit van het College voor Promoties  
in het openbaar te verdedigen  
op donderdag 23 februari 2006 om 15.00 uur

door

Mikhail Mikhaylovich Ovsyanko  
geboren op 28 april 1974  
te Simferopol (de Krim, Sovjetunie)

Dit proefschrift is goedgekeurd door de promotor:  
prof. dr. ir. Bene Poelsema  
en door de assistent-promotor:  
dr. ir. Herbert Wormeester

*To memory of M.V. Gil'manov*

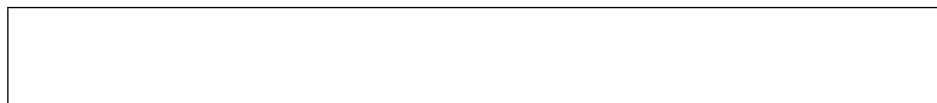


*if I had waited long enough I probably never would have written anything at all since there is a tendency when you really begin to learn something about a thing not to want to write about it but rather to keep on learning about it always and at no time, unless you are very egotistical, which, of course, accounts for many books, will you be able say: now I know all about this and will write about it. Certainly I do not say that now; every year I know there is more to learn, but I know some things which may be interesting now, and I may be away from the bullfights for a long time and I might as well write what I know about them now.*

Ernest Hemingway  
Death In The Afternoon  
(1932)







# Contents

<b>1</b>	<b>Introduction</b>	<b>1</b>
1.1	Mass Transport . . . . .	3
1.2	Ion impact . . . . .	5
1.3	Pattern formation . . . . .	6
<b>2</b>	<b>Experimental</b>	<b>13</b>
2.1	Introduction . . . . .	13
2.2	Low Energy Electron Diffraction . . . . .	14
2.2.1	Kinematic approximation . . . . .	15
2.2.2	Probing the Average Morphology . . . . .	17
2.2.3	Interface Roughness Determination . . . . .	20
2.2.4	Spot Profile Analysis . . . . .	23
2.2.5	SPA-LEED . . . . .	26
2.2.6	Transfer width . . . . .	29
2.3	Set Up . . . . .	31
2.3.1	UHV . . . . .	31
2.3.2	Sample Preparation . . . . .	34

<b>3</b>	<b>Nanopatterning through oblique incidence sputtering</b>	<b>35</b>
3.1	Introduction . . . . .	35
3.2	Experimental . . . . .	37
3.3	Step edge selection . . . . .	38
3.4	Normal incidence sputtering . . . . .	41
3.5	Oblique incidence sputtering along $\langle 110 \rangle$ . . . . .	54
3.6	Sputtering along $[100]$ . . . . .	61
3.7	Conclusion . . . . .	63
<b>4</b>	<b>Creation and temporal evolution of ripples on Cu(001)</b>	<b>67</b>
4.1	Introduction . . . . .	67
4.2	Experimental . . . . .	70
4.3	Results . . . . .	70
4.3.1	Ripples along $[110]$ . . . . .	70
4.3.2	Scenario . . . . .	80
4.3.3	Ripples along $[100]$ . . . . .	81
4.3.4	Influence of ion flux on the ripple evolution . . . . .	83
4.3.5	Annealing of ripples . . . . .	85
4.4	Discussion . . . . .	89
4.5	Conclusion . . . . .	97
<b>5</b>	<b>Nanogrooves enabled reconstruction on Cu(001)</b>	<b>99</b>
5.1	Introduction . . . . .	99
5.2	Grazing incidence sputtering . . . . .	101
5.3	A first layer reconstruction . . . . .	105
5.4	Conclusion . . . . .	115
	<b>Bibliography</b>	<b>117</b>

<b>Summary</b>	<b>129</b>
<b>Samenvatting</b>	<b>133</b>
<b>Acknowledgements</b>	<b>137</b>
<b>Curriculum Vitae</b>	<b>141</b>



# Chapter 1

## Introduction

The controlled production of regular surface structures on the nanometer lengthscale is a prerequisite for many present and future technological applications ranging from optics to electronics, to tribology, to magnetism and to chemistry. In particular, the great interest that these nanostructured interfaces have recently attracted, derives from realizing that their principal physical and chemical features heavily depend on their morphology [1–3]. The nanostructure morphology can be set by properly controlling the production process and thus the possibility of manufacturing new materials with tailored electronic, optical and magnetic properties is feasible. Many different approaches for this control have been proposed, but only few can be used on areas of macroscopic scale and have process parameters which are easily controllable. Only techniques which meet these requirements may have some chance to be actually considered as a means for practical implementation. Present patterning technology originates from microelectronic: lithographic techniques using UV-light or X-rays in future production. However, this technique requires heavy investment. Focused ion beams are also employed today

and scanning probe lithography has been proposed in order to engrave features on a surface with nanometer resolution. However, this can only be done in a limited scan area, typically of a few micrometers and with very slow throughput [4, 5]. Much more promising for nanopatterning appears the exploitation of self-assembly where the regularity and the size of the surface structures are built-in properties of a production process that can be conducted on large areas. Such very regular patterns have a limited applicability compared to for instance lithographic techniques with which virtually any pattern can be made. However, many applications in the area of tribology, self-cleaning and memories are feasible with ordered nanopatterning.

Growth and ion etching under the right conditions can show self organization on the nanometer scale. Arrays of two- and three - dimensional structures have been produced on a variety of substrates both by means of molecular deposition and of controlled ion erosion. Apart from promising technological applications, epitaxial growth and low energy ion sputtering represent also a very interesting object from a more fundamental point of view. In fact the nanostructures which form by exposing a surface to a molecular beam during deposition, or to a beam of accelerated ions during sputtering, result from a complicated interplay of a number of elementary diffusion processes and single ion-hit events. Understanding which kinetic pathways lead to the formation and the evolution of these structures is an extremely challenging task. By its solution one gains, on one side, the ability of predicting and thus controlling the surface morphology and, on the other, a deeper insight in the fundamental atomic-scale processes which are responsible for its evolution.

## 1.1 Mass Transport

Growth, erosion and coarsening are all processes in which mass transport on the surface determines the actual morphology. One of the first considerations is by Mullins who considered the smoothening of surfaces. The surface strives in this continuous description of mass transport to a flat surface. In the last decades an atomistic picture of mass transport has developed. The transport over the surface can be divided in two main components intra- and interlayer mass transport. The intralayer mass transport involves for instance the kinetically driven movement of adatoms over surfaces, the creation of stable clusters, and the movement along step edges. Many of these processes have been identified and quantified in the early stages of growth [6–8]. The interlayer mass transport concerns the communication between various layers present on a surface. After the formation of initial adatom islands, also material will be deposited on these islands during a growth experiment. The chance that this material will cross a step edge highly depends on the existence and height of a so-called Ehrlich-Schwoebel barrier, usually an extra barrier that obstructs the crossing of a step edge. For Cu and Ag(111) this barrier is so large that hardly any material can cross a step edge. For Cu(001) two different pathways for descent over a step edge have been identified, over the closed packed step edge and / or via kink, the latter being much easier. Also exchange processes at the step edge should be taken into consideration. A few of these processes and their barriers are shown in Fig. 1.1. The local surrounding has been shown to play a very prominent role in the various descent probabilities for the kinetically activated species.

The influence of vacancies is usually neglected in growth. Their presence and abundance on Cu(001) was nicely demonstrated in a

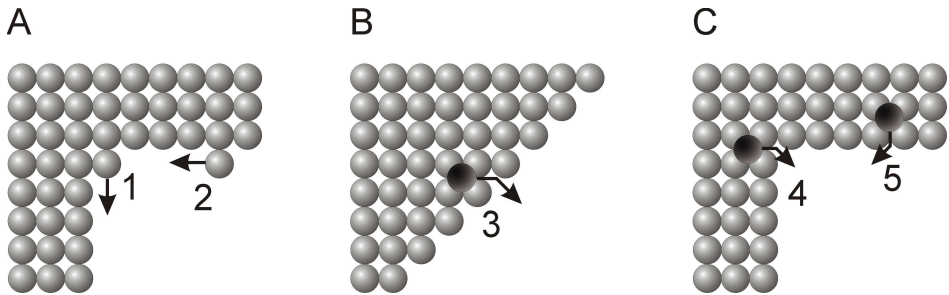


Figure 1.1: Important adatom geometries on the Cu(001) surface. The energies of these geometries are given in Table 1.1. a) intralayer diffusion, b) and c) interlayer diffusion

series of experiments involving In deposition. The movement of these atoms could only be explained with visits by moving vacancies. For Cu(001) the energy barrier for vacancy movement is similar to that of an adatom. In an erosion experiment, the influence of vacancies and vacancy clusters is of course very prominent. The interplay of vacancy and adatom transport will contribute to the pattern that evolves after erosion and makes the understanding of the formation of these patterns more complicated.

On a crystalline surface a further complication arises from the directional dependence of the diffusion. Anisotropy in diffusion readily occurs on (110) oriented surfaces and leads directly to anisotropic patterns. This has been extensively studied for sputtered structures on Ag(110) by Rusponi et al. [9]. For Cu(110) they reported that the anisotropy in the diffusion process is responsible for a temperature dependent orientation of the elongated structures [10]. A detailed theoretical analysis of anisotropy in diffusion processes was recently provided [11]. A multitude of structures was explained within a kinetic phase diagram depending on the relative strength of anisotropic diffusion transport.



Number	Process	Value
1	Diffusion away from kink site	0.60 eV
2	Diffusion along the $\langle 110 \rangle$ step	0.30 eV
3	Diffusion across the $\langle 100 \rangle$ step	0.54 eV
4	Descent of adatom at kink site	0.38 eV
5	Diffusion across the $\langle 110 \rangle$ step	0.77 eV

Table 1.1: Values of the activation energy for the diffusion of atoms for the fcc(001) surface [12].

## 1.2 Ion impact

The effect of an ion impact is very often condensed in the sputter rate: the average number of particles from the substrate emitted in to vacuum by an incident ion. This yield depends on various factors related to both the incoming ion and the substrate, like the mass of the ion and its energy, the chemical composition of the substrate and the specific crystal orientation as well as the incidence angle of the ion. Detailed analysis of that factor is a prerequisite for employing techniques as Secondary Ion Mass Spectroscopy and ion sputter profiling as routinely done in electron spectroscopy. However, this information is usually only available for particles incident with energies of several keV. The impact of an ion and its consequences, is globally described with Sigmund's theory [13], relating the distribution of the incoming ion's energy over the atoms in the vicinity of the impact. This includes the average depth reached by the incident particle. Detailed analysis on an atomic scale is very limited. One of the first reports in this context is the STM work on Pt(111) by Michely and Teichert [14]. They determined the damage on an atomic scale and observed that next to vacancies also adatoms are produced. In a low temperature experiment, the damage produced by single ion impacts of 1 keV Ne ions on Ag(001), was probed [15]. The damage produced

by a single ion extends over an area of about  $12 \times 12$  atoms. In this area a vacancy cluster with a size of 810 monovacancies and the 34 adatom clusters of 67 atoms each is observed. With a positive sputter yield, this indicates that many bulk vacancies have to be created. The observed crystallinity of the surface indicates that this is not affected by the presence of these bulk vacancies. Both adatoms and vacancies thus have to be considered as mass transport species in sputter experiments. In chapter 3 are described STM measurements performed after a small dose sputtering of a Cu(001) surface with 800 eV  $\text{Ar}^+$  ions. Both adatom and vacancy islands are created in the temperature range between 200 and 330K. The area of the vacancy islands is larger than the area of the adatom islands, indicating a net formation of vacancy islands in this case. However, both adatoms and vacancies play an important role in the structures created.

### 1.3 Pattern formation

Sputter etching by means of energetic ionized particles is a long-standing technique in the field of surface science and technology, whose applications extend from surface cleaning to depth profiling analysis and the creation of well ordered surface patterns. Many investigations have been devoted to the observation of roughness evolution with time under various conditions [16–24]. Such experiments are usually interpreted with various scaling theories [25]. Well ordered patterns in the form of periodic ripples on a surface under the influence of ion sputtering was already reported in the early seventies [26–28]. Since that time ripple formation upon ion bombardment has been reported of a large variety of substrates ranging from isolators to semiconductors and metals, including both crystalline and amorphous materials [10, 29–47]. The explanation for the evolution

of these patterns formation is usually provided in terms of morphological instabilities on the surface. Bradley and Harper (BH) were the first to provide a theoretical frame work for the observation of ripples and their dependence on experimental parameters [48]. Their analysis starts by using Sigmund's theory of sputtering [13, 49] to relate the sputter yield to the energy deposited in the near surface region by the incoming ion. A sputter yield variation with the local surface curvature was obtained, which induces an instability. This is at the basis of periodically modulated structures as different erosion rates for troughs and crests are predicted, the former being eroded faster than the latter (see Fig. 1.2). Consequently, any surface perturbation increases exponentially in time. This sputter process leads to the first three terms in their continuous equation describing the change with time of the local height  $h$  of the surface:

$$\frac{\partial h}{\partial t} = -v(\Theta) + v_x(\Theta)\partial_x^2 h + v_y(\Theta)\partial_y^2 h - K\nabla^4 h \quad (1.1)$$

Here  $v_x(\Theta)$ ,  $v_y(\Theta)$  are the effective surface tensions generated by the erosion process, dependent on the angle of incidence  $\Theta$  of the ions. Surface smoothening counters the erosion induced growth of the surface roughness by a general surface smoothing mechanism due to surface diffusion as introduced by Herring and Mullins [50, 51]. The diffusion rate is given by  $K$  and completes the so-called Bradley Harper equation given by eq. 1.1.

The solution of this differential equation predicts the formation of ripples with a wavelength that scales with the square root of the ratio of the diffusion and sputter rate. The great success of this model lies in the prediction that the ripple direction is a function of the angle of incidence: for small  $\Theta$  the ripples are parallel to the ion direction, while for large  $\Theta$  they are perpendicular to it. This feature and the

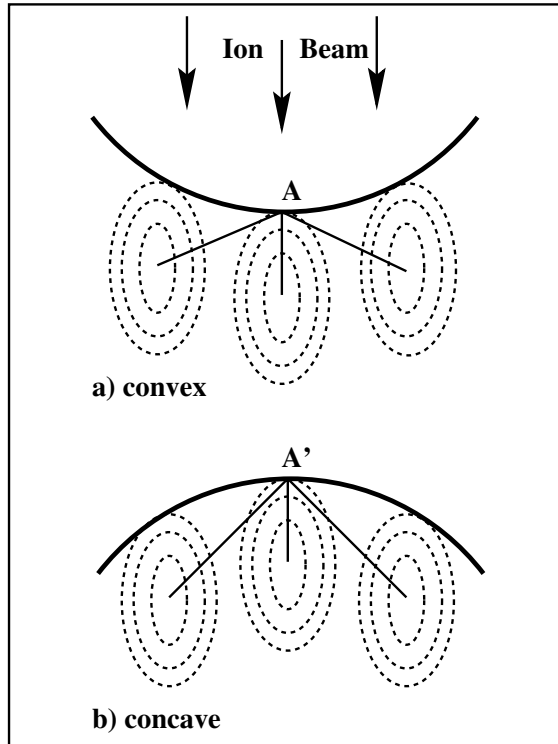


Figure 1.2: Schematic illustration of the physical origin of the instability during ion erosion of nonplanar surfaces. A surface element with convex geometry (a) is eroded faster than that with a concave geometry (b), due to the smaller distances (solid lines) the energy has to travel from the impact point to the surface (A or A' points).

transition angle have been confirmed by numerous experiments. The linear form of the BH Eq. 1.1 results in an unbounded exponential growth of the ripple amplitude, different from experimental observation. Modifications to this equation were suggested and an overview of continuous models is provided by Makeev et al. [52].

In the recent article Aste and Valbusa [53] presented approach contains, and extends, the Bradley - Harper approach [48] and its nonlinear extension by Rost and Krug [54] and by Park et al. [55] (based on a Kuramoto - Sivashisky and Kardar - Parisi - Zhang type equations [56–58]). This approach describes the dynamical behaviour experimentally observed in metals. They find that the ripples grow exponentially fast at constant wavelength  $\lambda$  up to a critical roughness (the root mean square of the height profile)  $W_c$  and then, if the Erlich - Schwoebel barrier is active, observed a transition between an initial exponential to a slower growth of the root mean square of the height profile.

Not only ripples, but also hexagonally ordered 1D patterns have been created through rotation of the sample while sputtering [3, 59]. As for the creation of ripples, the amount of ordering, characteristic length etc. depends on the substrate and the experimental conditions.

One of the great drawbacks of the BH ripple formation theory is that inherent to its continuous nature, the diffusion process is strongly simplified. Especially for crystalline materials, the diffusion is not azimuthally isotropic. Various studies on crystalline substrates have been performed. Rusponi et al. [45] studied for instance the influence of low energy ( $\geq 800$  eV)  $\text{Ar}^+$  ion bombardment on  $\text{Ag}(110)$ . Ripples with a wavelength of approximately  $600\text{\AA}$ , oriented along the  $[110]$  crystallographic direction were observed in a temperature range from  $270\text{K} \leq T \leq 320\text{K}$  at normal ion incidence. The ripple structure was found to be unstable at room temperature, i.e. substantial smooth-

ing of the surface with time takes place. Similar results are available for ion-sputtering of Cu(110) using a 1 keV Ar<sup>+</sup> ion beam [46]. For normal incidence a well-defined ripple structure was observed. However, the ripple wave vector changes direction from [001] to [110] as the temperature of the substrate is raised. This is the result of different diffusion processes active at elevated temperature. A detailed study of the morphology of Pt(111) after ion bombardment was done by the Michely group [60], while also the effects of grazing incidence sputtering were studied [61].

The influence of crystalline surfaces is also observed in the specific role adatoms produced in the sputter process can play. Under specific conditions, the number of adatoms can even outweigh the number of surface vacancies, resulting effectively in a growth like behaviour [62, 63]. The role of adatoms was also discussed by Costantini et al. [64] upon sputtering a Ag(001) surface. This surface has also been studied a decade earlier by Teichert et al. [12], who also reported an indication of a change in orientation of their square patterns as a function of temperature. This observation was made with Low Energy Electron Diffraction. In this thesis this reorientation after normal incidence sputtering is investigated for the Cu(001) surface with high resolution diffraction. This enabled the observation of various facets that occur as a function of temperature. It will also be shown experimentally that a strong reorientation of the sputtered morphology takes place at temperatures above 250 K upon switching off the ion beam. This result is interpreted in view of the particular diffusion processes active on the Cu(001) surface through which inter-layer mass transport is especially active along specific orientations. Also the influence of the angle of incidence of the ions on the morphology is studied.

At grazing incidence a very different sputter process takes place as many ions will be reflected by a flat surface without an actual sputter

event. This is in strong contrast with an ion incident on a protrusion on the surface, like ascending step edges, which provide a large sputter target. This leads to the formation of vary shallow ripples, as already reported by van Dijken [65]. The temporal evolution at various temperatures and azimuths is investigated. Also the temporal evolution of these ripples in absence of the ion beam is studied and used to explain the change in wavelength observed for these ripples in terms of atomic process on the surface. Such an explanation is only feasible if both mobile adatoms and vacancies are considered.

For shallow ripples created along the [100] azimuth not only the ripple wavelength is observed in the diffraction pattern. An additional feature at 1% of the Brillouin zone was found independent of the creation history, indicating that this feature is of thermodynamic origin. It is explained as the possibility of strain relief in the upper layer of a nanogroove without the necessity of the formation of dislocations. This is the first verification of van der Merwe's prediction of step facilitated reconstruction [66, 67]. The energy required for the latter blocks the strain relief on a smooth Cu(001) surface. Within the framework of the Frenkel - Kontorova spring - ball model a quantitative analysis of the strain relief is given, leading to a slight height modulation of the first layer atoms.





# Chapter 2

## Experimental

### 2.1 Introduction

Low energy electron diffraction was used as principal technique for the investigation of the surface morphology of patterned Cu(001) surfaces. With Low-Energy Electron Diffraction (LEED) one probes in reciprocal space and information on symmetry, surface unit cell dimensions, periodicity of structure, atomic roughness of a surface and facets is readily obtained. The diffraction pattern contains information averaged over a macroscopic surface area of about  $1 \text{ mm}^2$  (the size of the electron spot on the surface). High resolution diffraction is used in this work in order to obtain information on structures with a length scale up to several hundreds of atoms.

To obtain sufficient surface sensitivity the energy of probing electrons is typically chosen between 50 and 500 eV. A price has to be paid by multiple scattering effects on the intensity of the diffraction peaks. To extract information from electron diffraction patterns there are two major methods known as the kinematic and the dynamic approach: The kinematic theory is an approximation of the complete

scattering process as a single scattering event. The dynamic theory accounts for multiple scattering events and involves the total scattering intensity as a function of energy [68, 69]. This opens for instance the possibility to evaluate the atomic distribution within the unit cells. These multiple scattering effects are strongly electron energy dependent. However, the angular dependency of this multiple scattering is only small. Therefore, the shape of the diffraction peak at a specific energy can quite well be described with a kinematic approach. This shape contains information on the surface morphology. As a consequence only the diffraction spot positions and their intensity profile  $I(k_{\parallel})$  at a specific energy are analyzed.

Inelastic scattering of electrons breaks the phase and  $k$  - vector relations between the incoming and outgoing electron. This process thus limits the probing depth in electron diffraction. For the low energy regime, up to 300 eV, only electrons scattered from the first few surface layers will be scattered elastically and contribute to the diffraction pattern.

In the following chapter the basics of the kinematic approximation will be introduced as well as the instrument used. More detailed information can be found in the cited literature sources [68–71]. Furthermore, the set-up as well as the sample preparation procedures will be described.

## 2.2 Low Energy Electron Diffraction

The basics of electron diffraction theory will be discussed below, but limited to the evaluation of surface morphology. For energies between 30 eV and 500 eV, the electron wavelength is of the order the interatomic distance in typical crystal structures. This renders into a good technique for crystal surfaces as depth information is lim-

ited in this energy range. The limited probing depth of electrons still means that electrons will scatter from the first few layers, providing a difference in height of the scatterers even for a smooth surface. Also terraces bounded by step edges present on the surface will provide different height positions of scatterers. This difference in height provides constructive and destructive interference conditions. With  $k_{\perp}$  the component of the electron wavevector change perpendicular to the surface the interference condition can be expressed by the reduced perpendicular phase  $S_z$ .

$$S_z = \frac{k_{\perp} \cdot d}{2\pi} \quad (2.1)$$

where  $d$  is the interlayer spacing. Integer values of  $S_z$  correspond to constructive interference of waves diffracted from adjacent terraces, denoted as the in-phase condition (or Bragg). Half-integer values of  $S_z$  correspond to destructive interference, known as anti-phase condition (or anti-Bragg). Any other value is referred to as out-of-phase. The De Broglie relationship provided the electron wavelength  $\lambda = \sqrt{\frac{h^2}{2mE}}$  of particles with mass  $m$  and kinetic energy  $E$ . In the LEED experiments presented, the incident electron beam is always close to normal incidence. This implies that only  $k_{\perp}$  is significant to characterize the incoming beam and  $S_z$  can be given as function of the electron energy used (with  $E$  in eV):

$$S_z = 2d \cdot \sqrt{\frac{E}{150.4}} \quad (2.2)$$

### 2.2.1 Kinematic approximation

A brief review of diffraction theory within the kinematic approximation is now presented. In the kinematic diffraction theory, the surface is divided into identical unit cells. The wavevector of the scattered ‘particles’ can be described by plane waves, since the dis-

tance source-surface and surface-detector are much larger than the atomic distances. The wavefunction of a particle, scattered from the initial wavevector  $\mathbf{k}_i$  into the final wavevector  $\mathbf{k}_f$  by the surface atoms can then be written as [71]:

$$\Psi(\mathbf{K}, \mathbf{k}_i) = \frac{1}{N} \sum_{\mathbf{n}} \psi_{\mathbf{n}}^{unit}(\mathbf{K}, \mathbf{k}_i) e^{i\mathbf{K} \cdot \mathbf{r}_{\mathbf{n}}} \quad (2.3)$$

where  $\mathbf{r}_{\mathbf{n}}$  is the position of the  $n$ th unit cell,  $\mathbf{K} = \mathbf{k}_f - \mathbf{k}_i$  the scattering vector and  $N$  a normalization constant determined by the number of scatterers.

The scattering amplitude or structure factor  $\psi_{\mathbf{n}}^{unit}$  of the  $n$ th unit cell  $U_c(n)$  is given by

$$\psi_{\mathbf{n}}^{unit}(\mathbf{K}, \mathbf{k}_i) = \sum_{\varepsilon \in U_c(n)} f_{\varepsilon}(\mathbf{K}, \mathbf{k}_i) e^{i\mathbf{K} \cdot \mathbf{r}_{\varepsilon}} \quad (2.4)$$

The structure factor describes the scattering contributions to the outgoing wave due to scattering from the atoms within the unit cell. The atomic scattering factor  $f_{\varepsilon}$  describes the scattering properties of the single atoms within the unit cell. Multiple scattering effects and contributions due to the finite probing depth of the used particles can be incorporated in  $\psi_{\mathbf{n}}^{unit}$ . In that case eq. 2.4 would become more complicated.

The measured intensity is proportional to the square of the wavevector  $\Psi(\mathbf{K}, \mathbf{k}_i)$ ,

$$I(\mathbf{K}, \mathbf{k}_i) \simeq |\Psi(\mathbf{K}, \mathbf{k}_i)|^2 \quad (2.5)$$

The intensity is usually separated into the dynamical form factor  $F(\mathbf{K}, \mathbf{k}_i)$  and the lattice factor  $G(\mathbf{K})$ . This is possible if it is assumed that the scattering amplitudes of all unit cells are identical. The

intensity can now be simplified to:

$$I(\mathbf{K}, \mathbf{k}_i) \simeq F(\mathbf{K}, \mathbf{k}_i) \cdot G(\mathbf{K}) \quad (2.6)$$

with the dynamical form factor

$$F(\mathbf{K}, \mathbf{k}_i) = |\psi_{\mathbf{n}}^{unit}(\mathbf{K}, \mathbf{k}_i)|^2 \quad (2.7)$$

containing information on the scattering properties of the atoms within the unit cell. The lattice factor

$$G(\mathbf{K}) = \frac{1}{N^2} \left| \sum_{\mathbf{n}} e^{i\mathbf{K} \cdot \mathbf{r}_{\mathbf{n}}} \right|^2 \quad (2.8)$$

contains only information about the arrangement of identical scatterers at the surface.

The form factor  $F(\mathbf{K}, \mathbf{k}_i)$  depends strongly on energy as  $|\mathbf{K}| \sim \sqrt{E}$ , where  $E$  denotes the energy of the particles, but varies only slowly with the parallel component of the scattering vector  $\mathbf{K}_{\parallel}$  [72, 73]. Therefore the intensity can be written as:

$$I(\mathbf{K}, \mathbf{k}_i) \simeq F(E) \cdot G(\mathbf{K}) \quad (2.9)$$

In conclusion, the shape of the spot profiles is almost exclusively governed by the lattice factor. Thus, properties concerning the surface morphology will be found in this lattice factor.

## 2.2.2 Probing the Average Morphology

The average morphology of a surface is provided by the so-called correlation function of the morphology. This correlation function gives the probability of finding two scatterers on the surface separated by a certain distance vector. This distance contains components

parallel and perpendicular to the surface plane.

Within the kinematic approximation the scattering factor is the same for all exposed surface atoms;  $F(E) = 1$ . The incorporation of the surface morphology is started by identifying each unit cell as either a scatterer or not. If a scatterer is present, an equal scattering factor is given [74–77]:

$$\begin{aligned} f(\mathbf{r}) &= 1 && \text{if there is a surface scatterer at } \mathbf{r} \\ &= 0 && \text{otherwise} \end{aligned} \quad (2.10)$$

where  $\mathbf{r}$  gives the position of a surface scatterer. The correlation function  $C(\mathbf{u})$  expresses the probability of finding two surface scatterers separated by a displacement vector  $\mathbf{u}$  which spans over all the  $N$  surface positions:

$$C(\mathbf{u}) = \frac{1}{N} \sum_{\mathbf{r}} f(\mathbf{r}) f(\mathbf{r} + \mathbf{u}) \quad (2.11)$$

The diffracted intensity as evaluated by eq. 2.9 can now be written as:

$$\begin{aligned} I(\mathbf{K}) &= \frac{1}{N^2} \sum_{\mathbf{r}} f(\mathbf{r}) e^{-i\mathbf{K}\cdot\mathbf{r}} \sum_{\mathbf{r}'} f(\mathbf{r}') e^{i\mathbf{K}\cdot\mathbf{r}'} \\ &= \frac{1}{N} \sum_{\mathbf{u}} C(\mathbf{u}) e^{-i\mathbf{K}\cdot\mathbf{u}} \end{aligned} \quad (2.12)$$

In the further analysis a simple cubic lattice will be used, but the approach can simply be extended to other types of lattices. The displacement vector can with this approximation be rewritten in  $\mathbf{u} = \mathbf{x} + \mathbf{h}$ , where  $\mathbf{x}$  is a vector parallel to the surface,  $\mathbf{x} = am_x\hat{\mathbf{x}} + am_y\hat{\mathbf{y}}$

and  $\mathbf{h}$  is the height perpendicular to the surface plane,  $\mathbf{h} = al\hat{\mathbf{z}}$ . In these expressions of  $\mathbf{x}$  and  $\mathbf{h}$ ,  $a$  denotes the lattice constant and  $\hat{\mathbf{x}}$ ,  $\hat{\mathbf{y}}$  and  $\hat{\mathbf{z}}$  are unit vectors.

Two limits in the behavior of the correlation function have to be taken into account;  $C(\mathbf{u}) = C(\mathbf{x}, l)$  must vanish at the origin unless  $x = 0$  and at large separations between two scatterers ( $x \rightarrow \infty$ ), no correlation between the heights of the scatterers exists [78]. Consequently, the correlation function in the latter limit must equal the product of one-site probabilities  $p$  for scatterers at level  $l_1$  and  $l_1 + l$ :

$$C(\mathbf{x} \rightarrow \infty, l) = C_\infty(l) = \sum_{l_1} p(l_1)p(l_1 + l) \quad (2.13)$$

Now, by separating  $\mathbf{K}$  into its parallel and perpendicular components the diffracted intensity can be divided into the Bragg intensity  $I_B(\mathbf{K})$  and the quasi-diffuse intensity  $I_D(\mathbf{K})$ , which gives the information of the lateral surface morphology [77]:

$$\begin{aligned} I(\mathbf{K}) &= \sum_{\mathbf{x}} e^{-i\mathbf{K}_{\parallel} \cdot \mathbf{x}} \left[ \sum_{l=-\infty}^{\infty} C_\infty(l) e^{-iK_z l a} \right] + \\ &\quad + \sum_{\mathbf{x}} e^{-i\mathbf{K}_{\parallel} \cdot \mathbf{x}} \left\{ \sum_{l=-\infty}^{\infty} [C(\mathbf{x}, l) - C_\infty(l)] e^{-iK_z l a} \right\} \\ &= I_B(\mathbf{K}) + I_D(\mathbf{K}) \end{aligned} \quad (2.14)$$

To simplify the expressions for  $I_D(\mathbf{K})$  and  $I_B(\mathbf{K})$ , the equalities  $\sum_{l=-\infty}^{\infty} C_\infty(l) = 1$  and  $C(x, l) = C(x, -l)$  will be used. The last expression accounts for so-called reversible surfaces. A reversible surface is one in which the correlation function of the surface is symmetric with respect to positive and negative directions [78]. Except for some

macroscopic surfaces tilted with respect to the  $(x, y)$ -plane, these simplifications are justified.

The Bragg intensity can then be written as:

$$I_B(\mathbf{K}) = \sum_{\mathbf{G}_{\parallel}} \delta(K_{\parallel} - G_{\parallel}) \cdot \left\{ 1 - \sum_{l \neq 0} C_{\infty}(l) [1 - \cos(\mathbf{K}_z l a)] \right\} \quad (2.15)$$

The Bragg intensity arises from the Fourier transform of the constant part of the correlation function  $C_{\infty}(l)$ . This part of the intensity yields only a value when the condition  $K_{\parallel} = G_{\parallel}$ , i.e., the Bragg condition, is fulfilled. The intensity of the Bragg peaks is dependent on the one-site probabilities of a surface and therefore does not give any information about the microscopic arrangement of atoms at the surface, only about their distribution among the various layers.

The quasi-diffuse intensity can be simplified to:

$$I_D(\mathbf{K}) = \sum_{\mathbf{x}} e^{-i\mathbf{K}_{\parallel} \cdot \mathbf{x}} \sum_{l \neq 0} [C_{\infty}(l) - C(\mathbf{x}, l)] \cdot [1 - \cos(\mathbf{K}_z l a)] \quad (2.16)$$

Because of the dependence on  $C(\mathbf{x}, l)$ , the quasi-diffuse intensity  $I_D(\mathbf{K})$  contains the information on the morphology of the surface.

### 2.2.3 Interface Roughness Determination

With a surface diffraction tool, the average morphology is probed. This average morphology can be quantified by several parameters, like the surface roughness and characteristic length scales. The roughness has a direct influence on the intensity of the Bragg peak, as its strength, as already mentioned, reflects the distribution of the exposed layers, through the correlation function  $C_{\infty}(l)$ . The roughness



of a surface with a topography function  $z = z(r)$  is in real space usually expressed by the height-height correlation function  $H(r)$ . This function is defined as:

$$H(r) = \langle [z(r) - z(0)]^2 \rangle \quad (2.17)$$

This height - height correlation function reflects characteristic length scales and the roughness of the surface. The long-range asymptotic behaviour provides a constant value,  $2w^2$ , with  $w$  denoted as the root mean square roughness (rms) of a surface. This asymptotic behaviour gives

$$w^2 = \langle [z(\mathbf{r}) - \langle z \rangle]^2 \rangle, \quad (2.18)$$

where  $\langle z \rangle$  is the average height of the surface.  $w$  is also referred to as the interface width and is intimately related to the previously defined correlation function  $C_\infty(l)$ . The latter provides detailed knowledge on the presence of various exposed layers, while  $w$  provides its weighted average.

The determination of the interface roughness from a diffraction experiment was extensively discussed by Yang et al. [79, 80]. They argued that for a statistically rough surface, the distribution of the presence of various layers usually follows a Gaussian distribution. For this distribution, the Bragg intensity for the specular beam can be written as:

$$I_B(\mathbf{K}) = \sum_{\mathbf{x}} e^{-i\mathbf{K}_\parallel \cdot \mathbf{x}} e^{-K_z^2 w^2} = (2\pi)^2 e^{-K_z^2 w^2} \quad (2.19)$$

The  $\delta$  Bragg peak is thus proportional to a Debye-Waller like factor which is extremely sensitive to the global surface roughness. Also for a one dimensional Markovian distribution of surface steps a similar

attenuation is obtained [80].

The intensity measured in one Brillouin zone is the summation of the Bragg intensity and the diffuse intensity, the distribution over the two depending on the actual morphology. However, in the kinematic approximation, their sum only depends on the intensity of the incident electron beam and the reflectivity of the surface. This intensity can be normalized to  $(2\pi)^2$ . The ratio of the Bragg intensity to the total intensity in a Brillouin zone thus directly provides a measure for the surface roughness. Experimentally this procedure is limited by the fact that both energy and incidence / exit angle influence the measured intensity [80]. However, through normalisation of the intensity by measuring the ratio and the use of only small angle variations, such deviations from the kinematic results should be negligible. This ratio can be transferred to a property  $\Omega$  that can be evaluated as a function of electron energy.

$$\frac{I_B(\mathbf{K})}{I(\mathbf{K})} = e^{-\Omega(\mathbf{K}_z)} \quad (2.20)$$

$$\Omega(\mathbf{K}_z) = (w \cdot \mathbf{K}_z)^2 \quad (2.21)$$

In the LEED experiment, the ratio is evaluated from a series of line scans as a function of energy. The spectra are normalized to the intensity of the Bragg peak. From the in-phase condition, the shape of the (delta) Bragg peak can easily be evaluated and separated from the diffuse background. The shape of the Bragg peak is similar in all line scans and due to the normalization of the spectra also their areas have become equal, within experimental error. The inverse of the integration over the total intensity in one Brillouin zone directly provides the required ratio,  $e^{-\Omega}$ . For a one dimensional pattern, this integration is simply established. For a two dimensional pattern, the

integration has to be over the 2D area of the Brillouin zone. However, if the diffraction pattern has no or only slight azimuthal dependence, a series of energy dependent line scans suffices.

### 2.2.4 Spot Profile Analysis

A qualitative description of the influence of morphology on the electron diffraction pattern starts with the clean, crystalline surface. The intensity observed along the  $[110]$  azimuth as a function of the energy in the form of the reduced perpendicular phase  $S_z$  is depicted in Fig. 2.1. This picture is the result of a calculation using the kinematic approximation and a finite penetration depth of the electrons. Only at the Bragg positions, i.e. the depicted  $(00)$ ,  $(10)$  and  $(-10)$  spots show an intensity variation as a function of  $S_z$ , related to in-phase and out-of phase conditions.

Point defects (e.g. vacancies, interstitials and impurities), produce a homogeneous background at the expense of the Bragg peak intensities but do not cause a broadening of peaks. The diffraction rods from the clean surface will show the instrumental broadening, which is about 0.1% BZ. The observed width on a real clean surface is typically 0.3% BZ. The larger width is due to the presence of steps, i.e. the finite width of terraces. The additional broadening observed indicates that the average terrace width is typically 330 times the interatomic distance, i.e about 100 nm.

Defects on the atomically smooth surface cause a splitting and / or broadening of diffraction peaks. A schematic drawing of one - dimensional surface defects in the form of monolayer high adatom islands with a separation distance  $L$  is shown in Fig. 2.1. The intensity in the  $[110]$  azimuth as a function of  $S_z$  is also shown. At not exactly in-phase scattering conditions, the regular step array looks like a su-

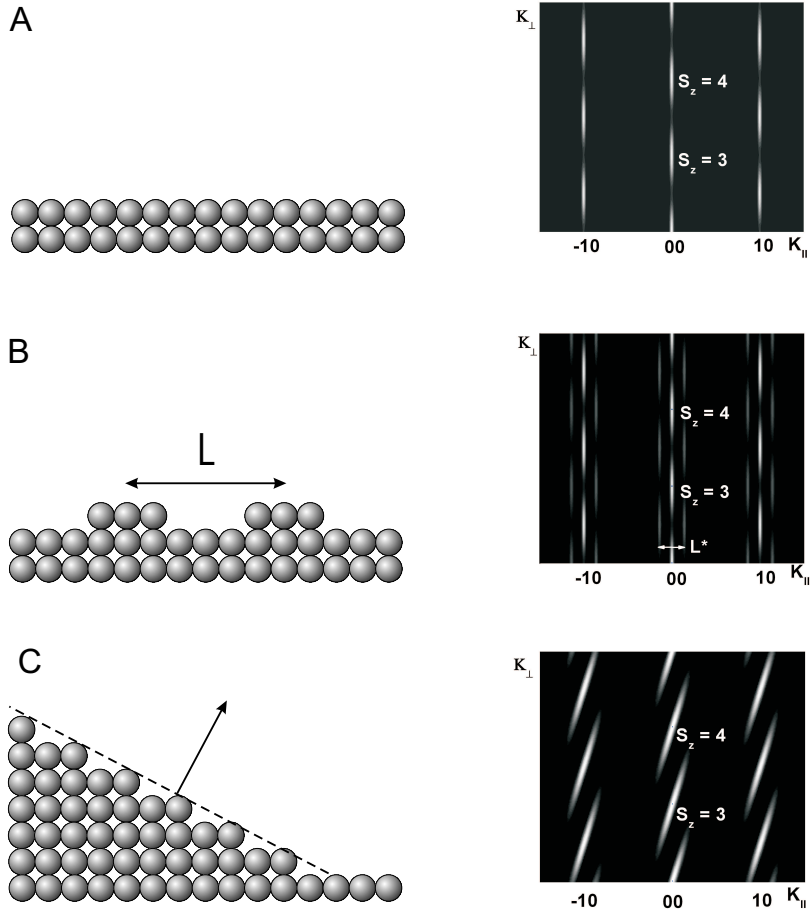


Figure 2.1: A schematic representation of one-dimensional surface defects and corresponding reciprocal lattices and intensity distributions: (a) flat surface, (b) regular up-and-down step array in two layers, (c) monoatomic regular step array.

perlattice with period  $L$ . This ordered superlattice gives rise to a splitting of the diffraction peaks, i.e., quasi-diffuse diffraction peaks, usually close to the Bragg peaks, appear. In particular, at anti-phase scattering conditions, the waves scattered from the upper terraces of the array destructively interfere completely with the waves scattered from the lower terraces. As a consequence, the Bragg diffraction peaks disappear and only the superlattice remains. The splitting of the diffraction peaks  $L^*$ , is related to the separation  $L$  via  $L^* = 4\pi/L$ . A distribution of  $L$  in real space is directly reflected in the width and intensity distribution of the ordering peak.

For multilayer surfaces, still a diffraction feature related to the average distance between structures can be observed. An additional ordering in these multilayer structures can occur, with the result that terraces of similar width are formed. In case at least two neighbouring terraces of similar width occur, a so-called facet can be defined: a local surface orientation different from a low Miller index surface. Such facets can be found in grown structures, in which case both sequences of step-up and step-down occur, or for vicinal surfaces. An example of facets with a regular step-down sequence is shown in Fig. 2.1c. The inclination of the local surface plane gives in diffraction rise to tilted Bragg rods in reciprocal space. At in-phase scattering conditions, all terraces interfere constructively and the position of the Bragg diffraction peaks is identical to those of clean surface. At other scattering conditions, however, also intensity is observed on the tilted Bragg rods. Observing the diffraction pattern at a specific electron energy provides a picture that is similar for ordered structures and faceted structures. Only variation of  $S_z$  provides a difference. In case of facets, the diffraction features are increasing their distance from the Bragg rod of the low Miller index surface with increasing out-of-phase condition, see Fig. 2.1. The inclination of the facet Bragg rod

directly provides the facet angle in real space.

It should be noted that thermal effects, i.e., inelastic scattering at vibrational lattice modes, do not contribute to a diffraction spot broadening but to a reduction in intensity and therefore increase the diffuse background.

Besides the usual  $k_{\parallel}$  images, i.e., diffraction patterns at constant energy,  $k_{\perp}$  vs.  $k_{\parallel}$  scans are directly accessible by recording a set of line-scans along a particular  $k_{\parallel}$ -direction at varying energy. Equivalent to the 2D diffraction patterns, the  $k_{\parallel}$  value is determined by the voltage applied at the deflection unit. Hence, the lattice rods of the surface run perpendicular in this representation. Facet structures can thus be resolved easily [70], as their lattice rods are inclined with respect to those of the macroscopic surface and the angle of inclination can directly be taken from such a type of scan. Moreover, this representation is useful for the determination of step heights, since in- and out-of phase conditions can directly be observed.

### 2.2.5 SPA-LEED

In the middle of the seventies of the last century Henzler and coworkers started the development of a new instrument for increased resolution Low Energy Electron Diffraction. The advantage of a High Resolution Low Energy Electron Diffraction (HR-LEED) apparatus over a conventional LEED set-up is the possibility of spot profile analysis. The transfer width of the used commercial High Resolution LEED - Omicron SPA-LEED amounts to about 1200 Å (the transfer width of a conventional LEED set-up is one order of magnitude smaller). The transfer width will be discussed in details in next subsection 2.2.6.

A schematic drawing of the cross-section of the SPA-LEED instru-

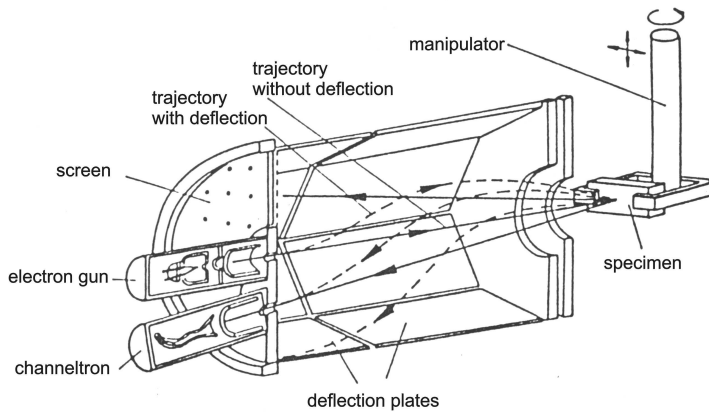


Figure 2.2: Schematic SPA-LEED set-up: the electron gun, the channeltron detector, the deflection unit, and the sample position are indicated. The path of the electrons from the gun to the detector is illustrated. The angle of incidence is varied by the voltage at the octupole deflection unit. The spot position on the sample remains constant during scanning.

ment is shown in Fig 2.2. The SPA-LEED can be operated in two modes. The diffraction pattern can be made visible on a fluorescent screen or the intensity of a very small area can be recorded in the channeltron mode. The visual mode is mainly used to adjust the position of the sample in front of the SPA-LEED and to find the right focus conditions for the electron beam. A qualitative inspection of the diffraction pattern can be made in this mode. Irrespective of the high resolution, the large advantage of the SPA-LEED compared with a conventional LEED is the possibility to determine quantitatively the scattered electron intensity distribution. The diffraction peaks can be swept across a channeltron with a high angular resolution. Instead of a mechanical rotation of the sample, the reflected electron beam is moved across the entrance aperture of the channeltron by means of three octupole fields. The octupole also deflects the incident electron beam on the surface before the reflected beam is recorded at the channeltron (see Fig. 2.2). The octupole is constructed in such a way that during a scan the electron beam stays at the same position on the sample. The angle of incidence of the electron will change during a scan. The angle of incidence is also electron energy dependent, which does not make this construction suitable for measurements used to evaluate electron diffraction within dynamic LEED theory.

The octupole deflection system does show several non-linearities like cushion and barrel distortion [81]. Especially for larger voltages on the octupole, i.e. outside the first Brillouin zone, the distortions can be quite dramatic. However, the measurements presented here are performed in proximity of the specular reflected beam. The sample is placed in such a position that the specular reflected beam is monitored by the channeltron without a voltage on the octupole.



### 2.2.6 Transfer width

In a diffraction experiment the observed pattern is the superposition of the scattering of each individual particle. As any real instrument exhibits an energy and angular spread, the scatter patterns are not all perfectly the same. This leads to an instrumental broadening of the diffraction spots. The transfer width is a measure of this broadening effect. It describes the theoretical length on a surface which would lead to a width of the diffraction spots, calculated without any spread in incident  $k$ -vectors, being identical to instrumental width. Information on length scales larger than the transfer width cannot be obtained without deconvolution of the instrumental response function. Therefore, the transfer width can be regarded as the resolution limit in a diffraction experiment. Comsa has investigated the problem of the determination of the transfer width in detail for atom scattering experiments [82]. The transfer width is determined by energy spread and geometrical factors. The influence of the energy spread of the beam, stems from the fact that particles of different energy each provide overlapping diffraction patterns. This leads to a transfer width  $\omega_E$  [82]

$$\omega_E \approx \frac{\lambda}{|\sin \Theta_i - \sin \Theta_f| \sqrt{(\Delta E_0)^2 / (E_0)^2}} \quad (2.22)$$

where  $(\Delta E_0)^2$  is the mean squared energy spread of the beam with primary energy  $E_0$  and wavelength  $\lambda$ .

In the second, a geometrically derived contribution to the transfer width was derived. In this case the information length scale is limited by diffraction patterns that overlap as a result of different geometric paths due to finite apertures [82]

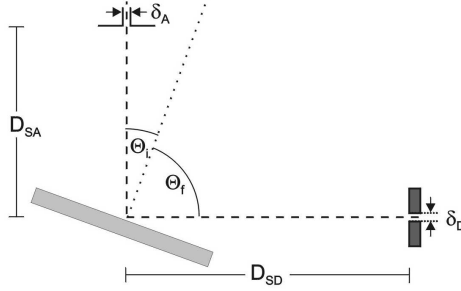


Figure 2.3: Schematic scattering geometry:  $\delta_A$ ,  $\delta_D$  denote the diameter of the electron beam collimator aperture and the detector aperture, respectively, and  $D_{SA}$  and  $D_{SD}$  the distance electron beam collimator aperture - sample and sample - detector, respectively.

$$\omega_{\Theta} = \frac{\lambda}{|\Delta\Theta_f| \cos \Theta_f} \quad (2.23)$$

with

$$\begin{aligned} (\Delta\Theta_f)^2 = & \left( \frac{\cos \Theta_i}{\cos \Theta_f} \frac{\delta_A}{D_{SA}} \right)^2 + \\ & + \left( \frac{\cos \Theta_i}{\cos \Theta_f} \frac{\delta_A}{D_{SA}} \frac{D_{SA}}{D_{SD}} \right)^2 + \left( \frac{\delta_D}{D_{SD}} \right)^2 \end{aligned} \quad (2.24)$$

for which the corresponding aperture widths and distances are indicated in figure 2.3. The resulting total transfer width  $\omega = \sqrt{\omega_{\Theta}^2 + \omega_E^2}$  thus yields

$$\omega \approx \frac{\lambda}{\sqrt{(\Delta\Theta_f)^2 \cos^2 \Theta_f + (\sin \Theta_i - \sin \Theta_f)^2 (\Delta E_0)^2 / E_0^2}} \quad (2.25)$$

In the high resolution experiments performed, the diffraction pattern is evaluated close to the specular beam. In this case  $\Theta_i \approx \Theta_f$  and the influence of the energy spread is negligible. This provides thus the experimental situation with the largest resolution.

The transfer width of the SPA-LEED used can thus be calculated to amount to a maximum of  $1200\text{\AA}$  at  $\Theta_i = 2^\circ$ .

## 2.3 Set Up

### 2.3.1 UHV

The experiments were performed using low energy electron diffraction, in an ultra-high vacuum (UHV) environment. The ultra-high vacuum chamber has a base pressure or less than  $2 \cdot 10^{-10}$  mbar. In Figure 2.4 a schematic drawing of the apparatus is given. It includes:

- Spot Profile Analysis Low Energy Electron Diffraction (SPA-LEED), manufactured by Omicron (Germany): this technique allows us to study the surface structure and morphology.
- Argon ion gun (Leybold): used for cleaning and patterning the sample's surface.
- Auger Electron Spectroscopy (AES): technique used to study the chemical composition of the sample.

The Auger effect is a non-radiative electron emission process of excited atom, mediated by electrostatic interaction. When an atom is irradiated either by high energy photons or electrons, with subsequent core hole formation, it rearranges its electronic structure such that a deep initial hole in the core level is filled by an electron from one of the outer shells. This transition may be accompanied by the emission

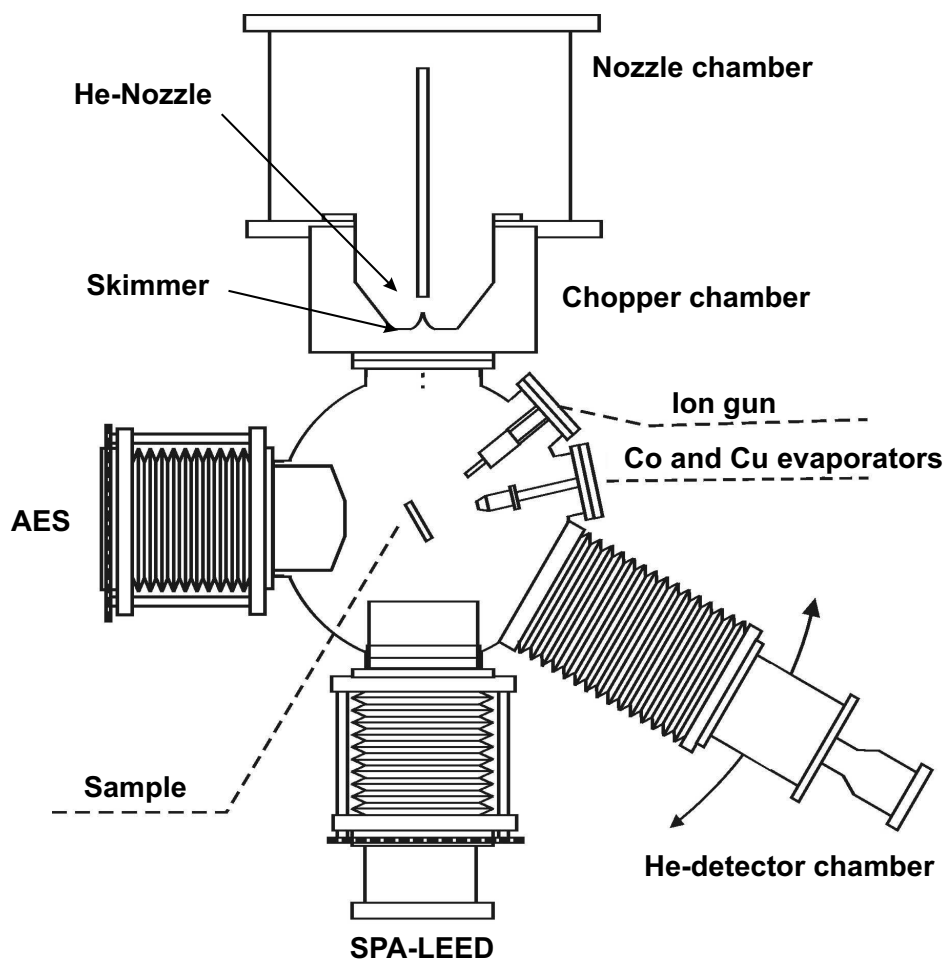


Figure 2.4: Schematic illustration of the experimental set-up.

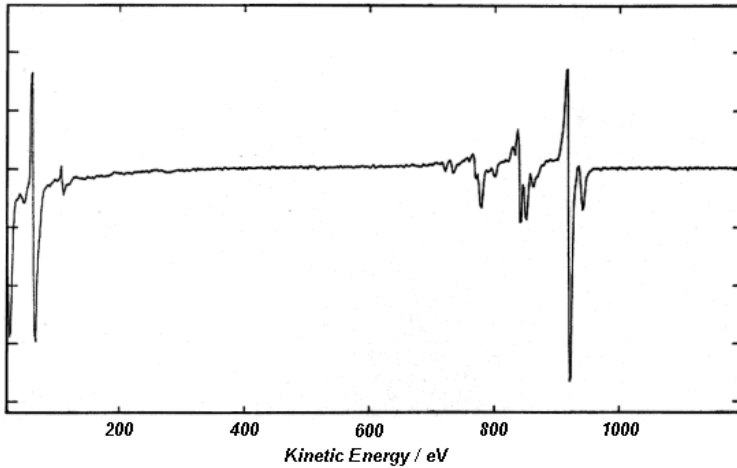


Figure 2.5: AES spectrum from the clean Cu(001) substrate.

of a characteristic X-ray photon or alternatively, the de-excitation process might be a radiationless Auger transition. In this latter case, the excess energy is transferred to another electron, which is ejected from the atom with a well-defined kinetic energy, directly related to differences in energy levels of the particular emitting atom. In our set up a primary beam of electrons with energy of 2.0 keV is focused on the sample surface while the backscattered electrons are collected and analysed in energy with CMA. A typical Auger spectrum contains a number of peaks at very precise values of energy, corresponding to the de-excitation processes activated. It's clear how this techniques is very sensitive to the various elements as each element has its own, easy identifiable, Auger peaks (see Fig.2.5). For this reason Auger spectroscopy is important to establish the surface composition and to identify the presence of impurities.

- Quadrupole Mass Spectrometer (QMS): used for analyzing the residual gases in the system.

- Thermal energy He Atom Scattering (TEAS): technique used for monitoring surface morphology during growth and sputtering. It was used in experiments to measure the sputter rate at normal angle incidence.
- Copper and cobalt evaporators.
- The system is also provided with cooling (liquid nitrogen) and heating facilities, which permit the variation of the sample's temperature from 100K up to 900K.

### 2.3.2 Sample Preparation

The Cu-sample is cut out of a Cu-crystal in the (001)-plane with an accuracy of  $\leq 0.1^\circ$ , whereafter it is mechanically polished. Prior to mounting into the UHV system the sample is heated to 900K in a H<sub>2</sub>/Ar environment for a few days. This treatment results in a very low impurity level of sulphur in the sample. The sample is cleaned in vacuum initially by prolonged sputtering with 800 eV Ar<sup>+</sup> ions at 600K. When no impurities can be detected anymore on the surface with AES, the sample is simultaneously sputtered and annealed at 900K. This treatment is needed to prevent sulphur, which segregates to the surface at temperatures above 800 K, of pinning of the step edges. When the sulphur impurity level on the surface is below the detection limit of AES ( $\leq 1\%$ ), an average terrace width of  $\gtrsim 1000 \text{ \AA}$  is usually obtained with this treatment. The average terrace width has been deduced from the width of the anti-phase specular SPA-LEED peak. After every growth experiment, the grown layer is completely removed by sputtering at 500K. After this sputtering process of the surface, the sample is annealed during a prolonged period to 750K. This procedure results in reproducible conditions for all growth experiments.

# Nanopatterning through oblique incidence sputtering

## 3.1 Introduction

Ion beam induced erosion is a very versatile technique in surface science. It is not only used for surface cleaning, but also for structuring on the nanoscale and for controlled removal of layers for sputter profile analysis [3, 41, 52, 83–87]. The fundamental understanding of the sputter process is of vital importance for the application of ion induced erosion in these areas. On many surfaces, patterning of the surface results in the formation of stripe patterns. The orientation of these stripes has been shown to depend dramatically on the polar angle of incidence [41, 52, 83]. These patterns are usually explained by the mechanisms introduced by Bradley and Harper [48]. Although the Bradley Harper theory has been and is still quite successful, it bears also all the disadvantages of continuum models. Therefore, it fails in identifying the rich detail of diffusion processes active on the surface essentially determining its morphology. Also in the initial

stages of the erosion process, different diffusion processes may be important. As stated by Bradley and Harper [48], their theory is also not applicable in the case of glancing incidence sputtering as they do not include reflection of ions. At glancing incidence the formation of a well ordered stripe pattern in the direction of sputtering was reported [65].

The formation of this pattern is argued to depend strongly on ion reflection and, most important on, anisotropic sputtering. In this chapter, a detailed experimental study of the morphology of a Cu(001) surface after erosion of some 20 ML of material is described as a function of both sample temperature and polar and azimuthal angles of incidence. We concentrate on the initial stages of the erosion process. A fourfold symmetry as on the initially flat Cu(001) surface is observed at normal incidence sputtering, but this changes to mirror symmetry with respect to the ion's plane of incidence when the sputtering geometry changes from normal to oblique incidence.

The orientation of the observed structures also depends markedly on temperature from normal incidence up to  $75^\circ$ . Beyond this angle, we observe a stripe pattern that is temperature independent. For near normal sputtering, difference in orientation observed at low and high temperature is attributed to the kick-in of kinetic limitations at low temperature, at intermediate temperature swift post bombardment processes are active, these lead to a substantial alteration of the morphology in the short time span between breaking-off the ion erosion process and freezing in the surface [12, 88] for analysis. The processes active during the erosion process and also during this short time span are sufficiently fast to enable a dramatic change of the surface morphology. The underlying diffusion processes will be highlighted with the aid of a generic rule in crystal growth, that links crystal shapes to the various advancement rates of specific crystal planes and step edges



[89]. This generic rule will be clarified first for a few representative situations. The surface evolution at normal incidence ion bombardment will then be discussed and subsequently the erosion at oblique incidence along the close packed [110] azimuth. Finally, we evaluate the results obtained during oblique incidence sputtering along [100].

## 3.2 Experimental

Our experimental method of choice to characterize the surface morphology is high - resolution electron diffraction (HR- or SPA-LEED), with a transfer width of about 1000 times the Brillouin Zone (BZ), see chapter 2. All experiments have been conducted in ultrahigh vacuum (base pressure well below  $10^{-10}$  mbar). The investigated substrate is a Cu(001) surface which has been prepared anew before each experiment by 30 min. of 800eV  $\text{Ar}^+$  ion sputtering and subsequent annealing up to 800K for 5 minutes. This initial procedure routinely yields a clean surface with an average terrace width exceeding 100 nm. Unless otherwise mentioned,  $\text{Ar}^+$  ion beams with an energy of 800eV and an ion flux of  $3 \cdot 10^{12}$  ions/s  $\text{cm}^2$  at normal incidence have been used. The sputter rate at normal incidence was determined from the recorded real time intensity change of a specular reflected thermal He beam. A maximum of the reflected intensity was observed after 6 min. of sputtering, and is attributed to the removal of one monolayer. This gives a yield of 1.4 removed atom per incident ion. With a fluence of  $2.2 \cdot 10^{16}$  ions/ $\text{cm}^2$  used in the experiments, a total of 20 ML is removed. At oblique incidence the sputter time was enlarged to achieve a fluence similar to the typical one at normal incidence. In the standard experiment the substrate temperature is quenched to 100K immediately after switching off the ion beam. Quenching from 330K to 235K takes about one minute. Below 235K no changes of the

morphology occur on the time scale relevant to the experiment.

### 3.3 Step edge selection

Crystal growth and erosion of crystalline solids are governed by the formation of quite well defined planes. Close to equilibrium, the structures assume their energetically around shapes and their facets with lowest free energy elongated. Under kinetic growth or etching conditions the final crystal shape is determined by those planes by growth or etching rates of the relative constitutively planes (in 3D) or steps (2D) [89]. A generic textbook rule states that for an expanding crystalline solid sphere the planes with the lowest advancement rate remain and thus determine the final kinetic shape. In contrast for shrinking spheres those with the highest retraction rate survive. The expansion part of this rule was shown to hold also in 2D with the orientation of growing adatom islands on a Pt(111) surface. The difference in island shape observed at various temperatures was explained by the temperature difference of the growth rates [90]. For sake of completeness, we note that the surface cleanliness has been shown to play a decisive role in the diffusion along the step and thus in their advancement rates [91]. The density of adatoms attached to a step edge can also vary due to interlayer mass transport over step edges with different diffusion barriers, which in turn depends on the decoration of the steps too [91]. Due to the nature of our sputtering experiments, we emphasize that impurity effects can be neglected in here. We stress that the kinetic growth situation described above, should be distinguished from the situation in which thermodynamics governs the island shape. At sufficiently high temperatures rearrangement processes can be very fast and the islands assume equilibrium shapes, with the domination of steps possessing the lowest line ten-

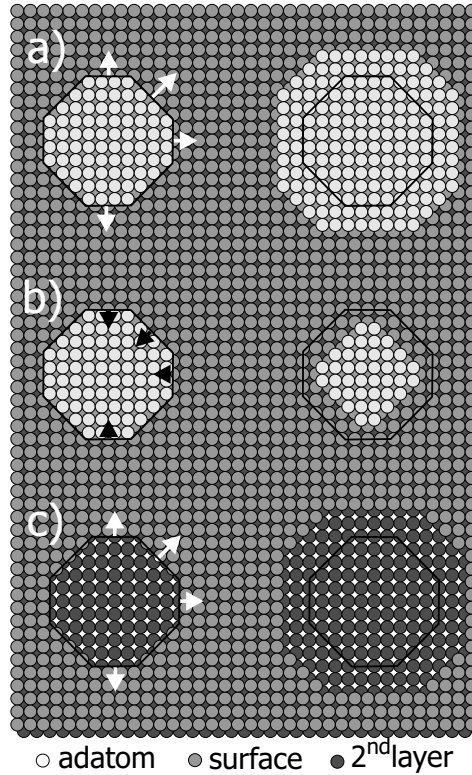


Figure 3.1: Schematic picture of the change in island shape for different growth rates of step edges. On the left is the approximately octagonal start shape and on the right the shape after expansion or shrinking. a) an expanding adatom island b) a shrinking adatom island c) an expanding vacancy island. The length of the arrows mimic the step edge advancement (a, c) / retraction rates (b).

sions. Under these conditions, step edges with a preferential  $\langle 110 \rangle$  orientation are expected and observed on a  $(001)$  oriented Cu surface.

The incident flux obviously is an important act which determines the temperature window in which the transition from thermodynamic to kinetic shape occurs. Under kinetic growth conditions, the shape of an expanding adatom island on a Cu(001) surface will be determined by the diffusion of adatoms attached to  $\langle 110 \rangle$  oriented step edges. Figure 3.1a shows this situation schematically for an initially almost symmetric octagonally shaped island. Diffusion of a ledge atom along  $\langle 110 \rangle$  steps is very fast. If corner-rounding is not providing a significant barrier, as should be expected here, adatoms will preferentially be incorporated in the  $\langle 100 \rangle$ -steps. This leads to a higher advancement rate of the latter, even enhanced by preferential descent of adatoms from the top of the island across  $\langle 100 \rangle$  steps [92]. One of the possible erosion processes on a surface is the shrinking of adatom islands. This leads to the opposite situation, which one may identify as negative growth as the step edge advancement rates are in the direction of the center of the island, i.e. the steps do not advance but rather retract, see Fig. 3.1b. Now as in 3D, the highest step edge retraction rate determines the shape. Again considering step edge diffusion as the dominant process, the fastest  $\langle 100 \rangle$  step edge retraction rate determines the kinetic adatom island shape with preferentially  $\langle 100 \rangle$  oriented step edges. However, the experimental observation of this is quite problematic as this has to occur in the kinetic erosion regime. On-top of that the surface is rather heterogeneous since a second form of erosion on a surface is the creation of vacancy islands. The kinetic shape of an expanding vacancy island is, similar to growth, determined by the slowest step edge advancement rate, see Fig. 3.1c. The close packed  $\langle 100 \rangle$  step edges thus determine

its shape.

It is by now well known that ion bombardment gives rise to adatom structures [62–64, 93–95]. Under certain favourable conditions the surface may even show a net expansion [62, 63]. We have carefully looked into this possibility and have found that under all conditions of interest here, we have a situation with net erosion (see below).

### 3.4 Normal incidence sputtering

Erosion through ion sputtering of a surface is more complicated than growth due to the fact that two different species relevant for the resulting morphology are created: (clusters of) vacancies and (clusters of) adatoms. Experimental results indicate that we can expect that at normal incidence an 800eV  $\text{Ar}^+$  ion bombardment of Cu(001) initially 2-3 adatoms are created per atom that is physically removed from the surface [14, 64]. Our STM measurements reveal that indeed adatom clusters do evolve together with vacancy clusters, see fig 3.2. However, in all cases relevant to this paper a net etching occurs! This implies that as a result vacancy islands always expand during ion bombardment.

It is also evident from these images that the average distance between vacancy islands increases with temperature and the orientation of the step edges of both adatom and vacancy islands is along the  $\langle 110 \rangle$  direction. Applying the generic rule described above, the step edge advance rate of the  $\langle 110 \rangle$  step edge is the smallest one for both adatom and vacancy islands, probably due to the high mobility of atoms attached to these step edges.

The influence of the adatoms on the morphology for further erosion was discussed by Costantini et al. [64] for Ag(001). Their comparison between the structures observed after growth and erosion at low

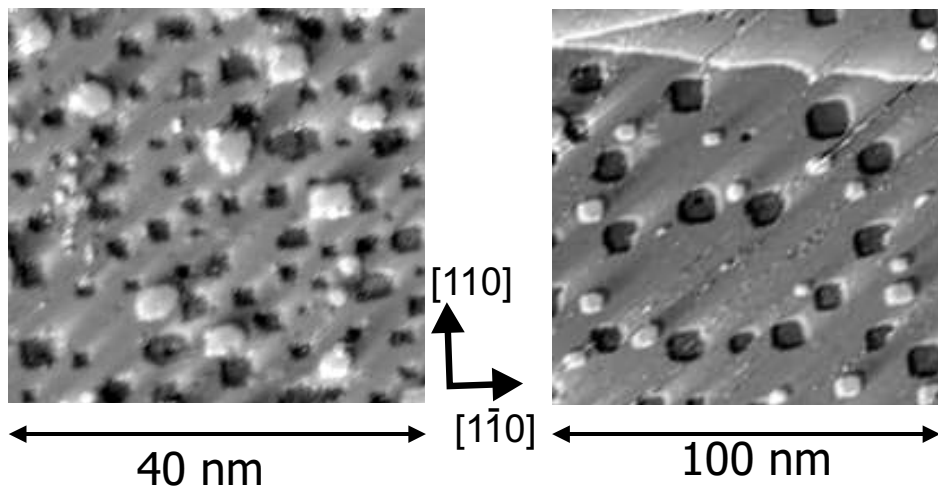


Figure 3.2: STM images of Cu(001) obtained after submonolayer erosion at 200K (left) and 325K (right).

temperature led them to the conclusion that the adatoms created in the ion sputtering process play the dominant role in the morphology obtained after erosion. At elevated temperatures etch pits with step edges along  $\langle 110 \rangle$  azimuths were observed, similar to previous STM measurements on Cu(001) [96, 97]. Previous to these measurements a "conventional" LEED study on normal incidence ion bombardment on Ag(001) was performed by Teichert et al. [12]. These latter experiments suggested that the azimuth orientation of defect structures depend on the preparation temperature. Sputtering at "elevated" temperature (300K) leads to structures with base lines parallel to the thermodynamically most stable  $\langle 110 \rangle$  directions. Ion bombardment at lower temperature (170K) results in structures with step edges preferentially orientated along the less densely packed silver rows along  $\langle 100 \rangle$  [12].

Figure 3.3 shows SPA-LEED profiles under slightly out-of-phase

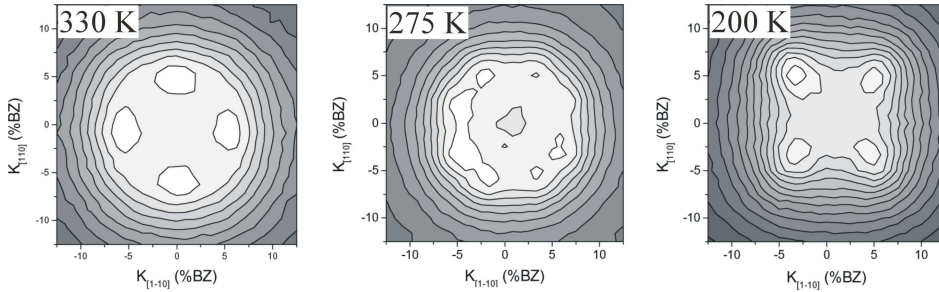


Figure 3.3: SPA-LEED contour plots of the specular beam acquired after normal incidence  $\text{Ar}^+$  sputtering of 20 ML Cu at 330K, 275K and 200K. The peak profiles were obtained at  $E=267$  eV ( $S_z = 4.79$ ).

conditions,  $S_z = 4.79$  taken after ion erosion of 20 ML Cu at 200K, 275K and 330K, respectively. Here  $S_z$  represents the so-called perpendicular scattering factor indicating the phase difference for electron scattering specularly from adjacent terraces in units of  $2\pi$ . It is immediately evident that ion bombardment at these temperatures, followed by the above mentioned standard quench procedure, leads to a fundamentally different surface morphology.

After sputtering at elevated temperature (330K) a fourfold symmetric spot profile is obtained with sub-spots aligned along the high symmetry  $\langle 110 \rangle$  axes. In contrast, the surface structuring at 200K leads to a fourfold spot profile with sub-spots lying along  $\langle 100 \rangle$  directions. For intermediate sputter temperatures (275K) a more complex intermediate state is observed with intensity maxima along  $\langle 310 \rangle$  directions. By increasing the electron energy and thus going to an in-phase condition ( $S_z = 5$ ) the sub-spots move to the center of the image consistently for all three temperatures. This implies that the observed diffraction patterns are related to facets rather than to a lateral ordering of defects as suggested in ref. [12]. The presence of

facet spots confirms the 3D-character of these defects, characterized by a relatively sharp terrace width distribution function. A quantitative analysis of the change in wavevector of these facet spots parallel to the surface,  $k_{\parallel}$ , as a function of the perpendicular wavevector,  $k_{\perp}$ , is presented in Fig. 3.4.

Facet angles of  $19^{\circ}$  for 235K and  $16^{\circ}$  for 300K are determined, corresponding quite well to (103)- and (115)-facets, respectively. Note that in these facets the atomic steps are oriented along  $\langle 100 \rangle$  and along  $\langle 110 \rangle$ , respectively. The (103) facet has been observed up to 240K. In the temperature range up to 320K, we have found diffraction patterns similar to the one at 275K, Fig. 3.3. From 300K up to 400K the (115) facet is observed, while above 400K the annealing during the cooling down procedure is so effective that no diffraction features beside the substrate Bragg spots can be observed. The insets in Fig. 3.4 show idealized hard-sphere models of the etch craters.

The roughness of the surface layer can be extracted from a diffraction experiment by a procedure outlined by Yang and coworkers [79, 80] and discussed in chapter 2.2.3. They argued that for a statistical distribution of exposed layers, this distribution usually has a gaussian shape. The intensity of the Bragg spot is then attenuated by a Debye-Waller like factor that contains the root mean square roughness  $w$  of an interface and the perpendicular scattering momentum  $k_z$ :

$$I_B \propto e^{-k_z w^2} \quad (3.1)$$

The reflected intensity thus depends on the electron energy, the angle of incidence and the reflectivity of the substrate. These experimental factors can be eliminated by normalizing the intensity of the Bragg peak to the total intensity scattered in the Brillouin zone surrounding the Bragg peak,  $I_{tot}$ . This approach does take advantage of



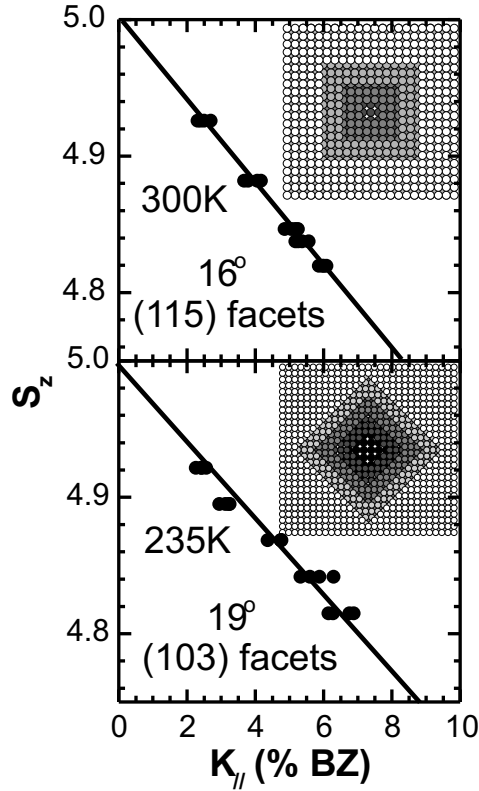


Figure 3.4: Change in wavevector of the facet spot positions (see Fig. 3.3) parallel to the surface,  $k_{||}$ , as a function of the perpendicular scattering phase  $S_z$  for a substrate temperature of 300K (top) and 235K (bottom). The data points at a specific electron energy represent the position of all 4 facet features present. The insets represent idealized hard-sphere models of the assumed defects.

the fact that the scattering vector depends only slightly on  $k_{\parallel}$ . We can thus obtain from the intensity ratio the rms roughness:

$$k_z w = \sqrt{\Omega} = \sqrt{\ln \left( \frac{I_{tot}}{I_B} \right)} \quad (3.2)$$

Energy dependent linescans were used to evaluate the intensity ratio expressed in  $\sqrt{\Omega}$ . In the analysis, line scans along both [110] and [100] azimuths were used. However, no significant difference between these two was found in the energy range studied, i.e. between 4.91 and 5.08. In 2D scans in this region, the facet features are difficult to distinguish, indicating that the diffraction pattern is azimuthally isotropic. The result is shown in Fig. 3.5. A symmetric feature shape of  $\sqrt{\Omega}$  around the 5th in-phase condition, as should be expected, is observed. The roughness at the two sputter temperatures of 235 and 300K can be extracted from the linear dependence of  $\sqrt{\Omega}$  to  $S_z$ . The roughness is similar for these two temperatures and amounts to  $w = 2.86$  in units of the height difference between adjacent terraces. One would expect a higher roughness in the low temperature case. However, this can be counteracted by the wider separation of structures at 300K. Below  $S_z = 4.91$ , a strong deviation of the linear behaviour is observed, which is attributed to the visible appearance of facets.

A 10-fold reduction of the ion flux did not influence the facet angle, i.e. at 235K and 330K facets with (103) and (115) orientation have been found, respectively. A reduction of the ion energy to 200eV, which in our case is accompanied by a 10-fold reduction of the flux compared to the standard sputter conditions leads to (117) facets at 300K. The latter value is similar to the one observed by Ernst [98] with 350eV  $\text{Ar}^+$  ions similar erosion conditions. In line with common sense, the lower sputter yield related to lower energy ions, apparently leads to smaller slopes, i.e. structures closer to equilibrium. At 235K

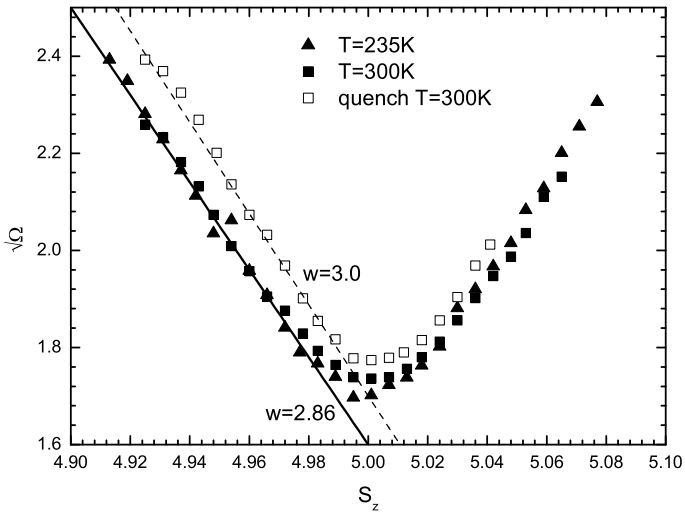


Figure 3.5: Roughness determination from the ratio of the Bragg intensity to the total scattered intensity in the first Brillouin zone. Results are shown after sputtering at 235K, 300K and the alternative cooling procedure, denoted quench.

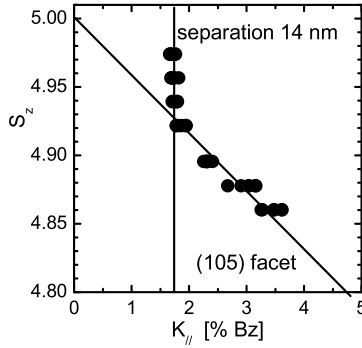


Figure 3.6: Change in perpendicular scattering phase  $S_z$  as a function of the wavevector of the facet spot positions parallel to the surface,  $k_{||}$  after sputtering at 235K, 200eV.

and 200eV  $\text{Ar}^+$  ions, (105) facets are observed as shown in Fig. 3.6. However in this case, near in phase condition,  $k_{||}$  no longer depends on  $S_z$ . This value of  $k_{||}$  represents the average lateral distance of 14 nm between the centers of the erosion structures. Apparently the lateral order has improved with the lower sputter rate accompanying sputtering at 200eV. Note that both flux and yield are reduced. In line with this, after sputtering at 800eV with 10 fold reduced flux an average separation distance of 10 nm can be evaluated. These values reflect the limited extension of the erosion structures and show the tendency for a lesser overall roughness of the surface after bombardment at lower ion energy.

The erosion process for  $\text{Ag}(001)$  has also been studied by Teichert et al. [12] with kinetic Monte Carlo simulations. The erosion process was modeled by a single atom removal event, while the probability of diffusion paths was determined from first principle calculations. The

production of adatoms following the ion impact was not included in the model. These simulations do reveal the different characteristics of the morphological evolution at low and high temperatures we observed for the closely related Cu(001) surface. Site selective interlayer mass transport was identified as the responsible ingredient for the emerging surface morphology. The descent of adatoms does predominantly occur at certain kink sites, naturally present in abundance at  $\langle 100 \rangle$  rather than across close packed  $\langle 110 \rangle$  steps. In other words, the Ehrlich - Schwoebel barrier for the descent of adatoms is significantly lower for the  $\langle 100 \rangle$ -ledges as compared to that for  $\langle 110 \rangle$  -ledges.

The importance of highly selective interlayer diffusion paths for the surface morphology of Cu(001) was demonstrated recently by Li et al. [92] by means of STM. SPALEED data shows that even after erosion of approximately 0.8 ML at 200K,  $\{103\}$  facets are present. Application of the above discussed geometric rule reveals that the step advancement rate of the  $\langle 100 \rangle$  oriented steps must be lower than that of the close packed  $\langle 110 \rangle$  ledges. This is the result of the preferential interlayer mass transport current across the  $\langle 100 \rangle$  step edges. Consequently, the advancement rate of  $\langle 100 \rangle$  step edges is smaller than that of the  $\langle 110 \rangle$  step edges leading to the observed dominance of the  $\langle 100 \rangle$  step edges.

The application of the geometric rule provides straightforward evidence for enhanced interlayer diffusion across  $\langle 100 \rangle$  steps from the persistence of these steps even after etching as little as 0.8 ML and afterwards. However, up to 0.5 ML, SPA-LEED and STM show that even at low temperature (235K) structures with  $\langle 110 \rangle$  step edges dominate. STM reveals that in this range more vacancy- than adatom - clusters are present and various vacancy and adatom clusters start to coalesce. The observation of dominant  $\langle 110 \rangle$  step edges indicates that initially (up to 0.5 ML) the selective interlayer diffusion across  $\langle 100 \rangle$

plays a subordinate role. The erosion is characterized by expanding vacancy clusters and advancement rates of the close packed steps will, similar to growth, be the dominant kinetic process: vacancy islands bounded by  $\langle 110 \rangle$  steps are observed, Fig. 3.1c. The observed lower interlayer mass transport during initial stages of erosion can be rationalized as follows: the adatoms generated as a result of ion impact diffuse, nucleate and form initially expanding adatom islands. At the same time the created vacancies also diffuse, nucleate and form expanding islands. Note that under the conditions relevant to our experiments, the integrated areas of the vacancy clusters always outweighs that of the adatoms clusters. Due to an always non - zero Ehrlich - Schwoebel barrier the adatoms will initially be incorporated more easily in the adatom island rather than contribute to shrinking of the vacancy islands. With proceeding etching the vacancy islands become predominant and interlayer diffusion apparently is increasing. The latter process takes place preferentially across  $\langle 100 \rangle$  steps. We emphasize that during, or just preceding coalescence paths with lower energy barriers become available too [12], further contributing to enhanced and site specific interlayer mass transport across  $\langle 100 \rangle$  ledges. So it appears, that the reversal of the kinetic island orientation, occurring between etching of 0.5 and 0.8 ML, can be well accounted for in terms of site specific interlayer mass transport across the open  $\langle 100 \rangle$  step edges.

The different predominant step orientations observed after ion bombardment induced erosion at low and high temperature was attributed to fast post erosion annealing effects at high temperatures by Teichert et al. Their simulations suggest that a less than one second annealing at room temperature is sufficient to change the surface morphology from a  $\{10n\}$  faceted structure to a  $\{11m\}$  faceted structure [12]: The transition from kinetically favored steps along  $\langle 100 \rangle$

to the thermodynamically favored ones along  $\langle 110 \rangle$  can be unexpectedly fast. In a recent experimental study the possibility and thus the consequences of such fast annealing processes have been disregarded [94]. However, exactly these events could well be responsible for the preference for the different step orientations, observed at high and low temperature, Fig. 3.3. In other words, the morphology observed after erosion at 330K may be determined by a swift drive towards equilibrium, while the 200K data still represent the kinetic shape of the clusters. To check this issue experimentally a quite different cooling procedure has been applied to avoid undesired annealing effects. We started cooling down the sample after an initial erosion of about 20 ML of the Cu(001) surface at 330K, while the erosion was continued until a critical sample temperature (for self-annealing) of 235K was reached. Subsequently, the cooling down was continued without sputtering down to 100K. During simultaneous sputtering and quenching from 330K to 235K a total of only 0.15 ML of copper was additionally removed. Hence, the amount of additionally etched material is insignificant and we expect to obtain a morphology of the surface closely resembling the in-vivo one during ion bombardment at 330K. The result of this experiment is given in Fig. 3.7a and shows clearly a SPA-LEED profile indicative of facets with steps along the  $\langle 100 \rangle$  directions similar to the patterned surface at 200K (Fig. 3.3). Therefore, we conclude that the orientation of step edges *during* sputtering is similar for temperatures between 200K to 330K. The evolution of  $\langle 100 \rangle$  ledges during sputtering is apparently kinetically favoured up to  $\approx 330$ K. The observed qualitative differences in morphology apparent from the peak profiles (Fig. 3.3) recorded at 275K and 330K are artificial and are assigned to the *annealing processes after the ion bombardment* at elevated temperatures leading to a swift transition from a  $\{10n\}$  faceted structure to a  $\{11m\}$  faceted structure, in accordance

with ref. [12].

Obviously the question whether during ion bombardment the kinetic cluster shape with  $\langle 100 \rangle$  oriented steps or the thermodynamically favored  $\langle 110 \rangle$  steps prevails, is determined by the rate at which the system is driven towards equilibrium and the time scale set by the experimental conditions. In general, higher temperatures and lower erosion rates naturally lead to vacancy cluster shapes closer to the equilibrium one. An illustration of the latter is provided in Fig. 3.7b. It exemplifies the diffraction profile of the Cu(001) surface at 330K after ion bombardment with a, compared to Fig. 3.7a, 10 times reduced flux but equal fluence. The quenching procedure is the same as described for Fig. 3.7a. In this case the amount of eroded material between the start of quench and stopping the sputtering is only 0.015 ML. The observed spot profile is similar to the one obtained after ion bombardment at 275K at a 10 times larger flux (see Fig. (3.3), i.e., indeed indicative of being closer to the equilibrium cluster shape, in line with the more efficient role of step edge diffusion during sputtering.

The influence of this alternative cooling down procedure on the interface roughness was determined by measuring the ratio of the Bragg peak intensity to the total scattered intensity in the first Brillouin zone. The result of this measurement is depicted in Fig. 3.5. A rms roughness value  $w = 3.0$  in units of the height difference between adjacent terraces is found. This value is only slightly larger than in case of the standard cool-down procedure. This indicates that, as expected, the cool down process does not influence so much the roughness but changes dramatically the orientation of the structure.

Extension of our findings for the ion bombardment induced erosion of Cu(001) to the closely related Ag(001) system provides a direct framework to understand the anomalous roughening behavior



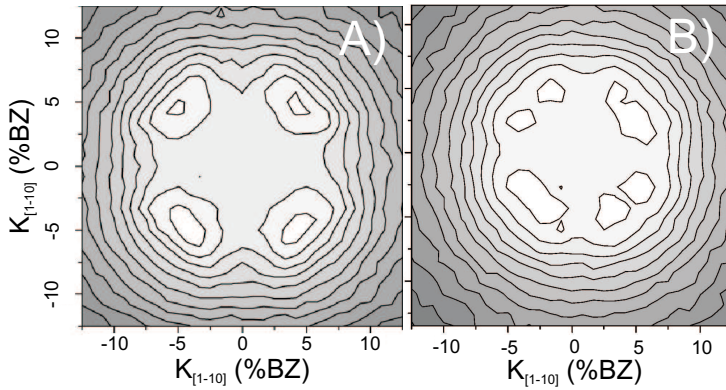


Figure 3.7: SPA-LEED contour plot of the specular beam acquired after  $\text{Ar}^+$  sputtering of 20 ML Cu for sputter rate of 0.16 ML/min (a) and 0.016 ML/min (b). at a temperature of 330K. The alternative cooling procedure as described in the text is applied.

observed for the latter as reported by Costantini et al. [64, 94]. They have found that the width of the eroded  $\text{Ag}(001)$ -vacuum interface shows a pronounced maximum around 325K. By definition, the width of the surface morphology is intimately related to the probability for interlayer diffusion. As noted further above this applies to the lateral length scale: a higher density of etch / growth structures leads to a smaller rms roughness. Application of our observations for  $\text{Cu}(001)$  to the  $\text{Ag}(001)$  data leads to the following physical picture: At low temperatures,  $\langle 100 \rangle$ -oriented steps, allowing fast interlayer diffusion, prevail. Around and above room temperature the thermodynamically favored  $\langle 110 \rangle$  ledges become dominant. The latter are associated with a higher Ehrlich - Schwoebel barrier, causing reduced interlayer diffusion and rougher interfaces further enhanced by increasing length scale. With increasing temperature thermal excitations gradually suffice to overcome the Ehrlich - Schwoebel barrier, leading to increased

interlayer mass transport and thus smoother interfaces. In the end the gain of interlayer diffusion with increasing temperature overrules the counteracting increase of lateral length scale. We do note also, that our model implies that the adatom islands initially growing on Cu(001) during normal incidence always have predominantly close packed steps. Only impurities, which can have an important impact on adatom island shapes [91] may alter this conclusion. However, the presence of such impurities is highly improbable in our sputtering experiments.

### 3.5 Oblique incidence sputtering along $\langle 110 \rangle$

The fourfold symmetry observed at normal incidence is changed into mirror symmetry by sputtering at oblique incidence. Figure 3.8 shows the diffraction image at various polar angles of incidence ranging from normal to glancing incidence.

The diffraction spots remain at the same position up to a polar angle of incidence of  $50^\circ$ . The relative intensity of the spots, however, has changed and the fourfold symmetry is clearly broken. The two less intense spots relate to the illuminated side of the erosion structure, indicating a less well defined facet at this side compared to the shadow side (left hand side spots). Beyond  $50^\circ$ , the facet spots move closer to the center indicative of the evolution of less steep facets. This movement is only in the plane of the incident ion beam, i.e. along the  $[110]$  direction. In the  $[1\bar{1}0]$  direction the spots remain at a similar position. Up to an angle of  $73^\circ$  four spots can still be distinguished. At and beyond  $80^\circ$  only two subspots can be observed, whose position no longer depends on the electron energy. At this glancing angle a well defined pattern of shallow stripes is formed, i.e. a 1D nanostructure [65, 99], with a separation distance of 6 nm at

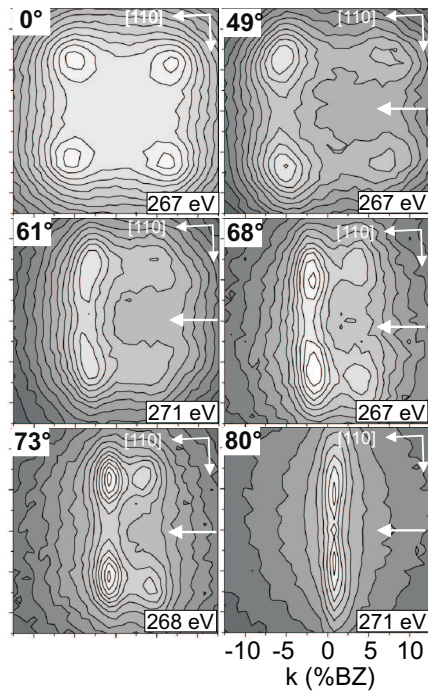


Figure 3.8: SPA-LEED contour plot of the specular beam acquired after oblique incidence  $\text{Ar}^+$  sputtering of 20 ML Cu at 235K. Indicated is the polar angle of incidence. The peak profiles were obtained at the electron energies indicated. For off-normal incidence the ions impinge from right to left (white arrows).

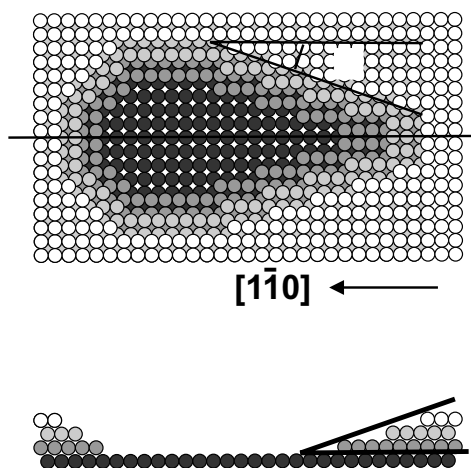


Figure 3.9: Real space hard-sphere model of the crater after oblique incidence sputtering. The top view shows the definition of the angle  $\beta$  and the side view that of the angle  $\gamma$ . The plane of incidence is along  $[1\bar{1}0]$

235K. These nanogrooves are oriented along the plane of incidence of the bombarding ions.

A hard-sphere model in real space of the etch structure is shown in Fig. 3.9. In this etch structure two characteristic angles,  $\beta$  and  $\gamma$ , correspond to well defined facets at the shadow side of the incoming ion beam. Both angles are easily extracted from the diffraction patterns at various ion angle of incidence for both the shadow and illuminated side. Qualitatively we observed that angles  $\gamma$  and  $\beta$  are larger for the illuminated side than for the shadow side. This means that steeper facets are observed for the less well defined illuminated side.

The change in diffraction pattern with increasing polar angle of the  $\text{Ar}^+$  ions at 320K is shown in Fig. 3.10. Again the fourfold symmetry observed after bombardment at normal incidence is lost

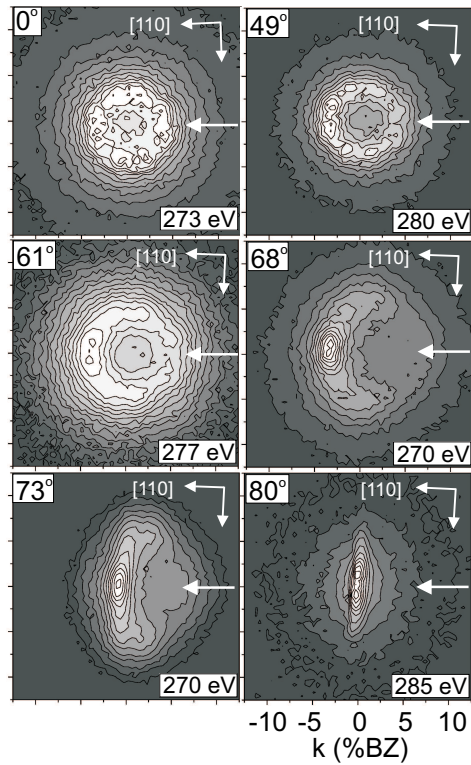


Figure 3.10: SPA-LEED contour plot of the specular beam acquired after oblique incidence  $\text{Ar}^+$  sputtering of 20 ML Cu at 320K. Indicated is the angle of incidence with respect to the normal. The peak profiles were obtained at the electron energies indicated. The ions move from right to left.

completely at polar angles of incidence of  $50^\circ$  and higher. Instead a two-fold symmetric pattern develops, leading finally at grazing incidence, similar to glancing incidence sputtering at low temperatures, to the formation of a regular pattern of shallow stripes parallel to the plane of incidence. The average distance of the stripes at 320K is about 20 nm. At 330K and glancing incidence, no stripe pattern could be observed, probably due to the resolution limitations of the used SPA-LEED instrument. At polar angles of  $49^\circ$ ,  $61^\circ$  and  $68^\circ$  the spot splitting relative to the facets on the shadow side can be seen. At this temperature this splitted spot becomes more and more intense with increasing angle of incidence, indicating a very well defined facet at the side of the incoming ion beam, while the illuminated side becomes less defined. The diffraction pattern at  $73^\circ$  shows that the etched structures become elongated, with a facet angle  $\gamma = 2^\circ$ . Obviously,  $\beta$  can not be derived with appreciable accuracy in this case.

As discussed above, the cool down procedure for the structures created at elevated temperatures and normal incidence sputtering determined the observed diffraction pattern. The alternative cooling procedure in which first the temperature is lowered and the sputtering is abruptly when the temperature has reached 235K, results in a different structure than with the normal cooling procedure. The same cooling procedure was also used after sputtering at 330K at an angle of incidence of  $49^\circ$  and  $61^\circ$ . The result of this shown in Fig. 3.11, and shows a structure very different from the one observed with the standard cooling procedure. As at normal incidence, the observed diffraction pattern after this quench procedure is quite similar to the one observed at low temperature. This implies that also after oblique incidence sputtering the morphology dramatically changes due to the short anneal during cooling down of the sample after sputtering. The

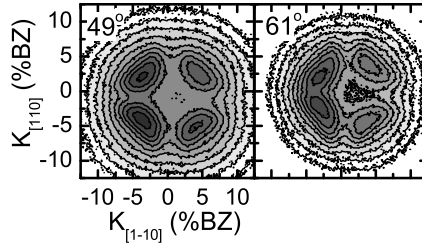


Figure 3.11: SPA-LEED contour plot of the specular beam acquired after  $\text{Ar}^+$  sputtering of 20 ML Cu at 330K at polar angles of incidence of  $49^\circ$  and  $61^\circ$  and the cooling procedure as described in the text. The peak profiles were obtained at an electron energy of 273 eV.

peak profiles in Fig. 3.11 are believed to closely represent the *kinetic* shapes of the ion bombardment induced surface structures.

The dependence of  $\beta$  and  $\gamma$  on the angle of incidence of the ion beam is shown in Fig. 3.12.

The general behaviour of  $\gamma$  can be explained by considering the interaction of low energy ions with surfaces. Behind each surface atom a shadow cone is casted. The consequence is that within this cone no atoms are visible to the incident ions, yielding a minimal facet angle on the shadow side of the etch structure. This leads to a critical angle [100]. A rough estimate of the critical angle is given by the cut-off of  $\gamma$  at  $70\text{-}75^\circ$ . This implies a critical angle of  $\approx 15^\circ$ , which is very reasonable for 800eV  $\text{Ar}^+$  ions interacting with copper. The behaviour of  $\beta$  is obviously linked to  $\gamma$  and is further thought to be determined by an interplay between edge diffusion and local sputter rate.

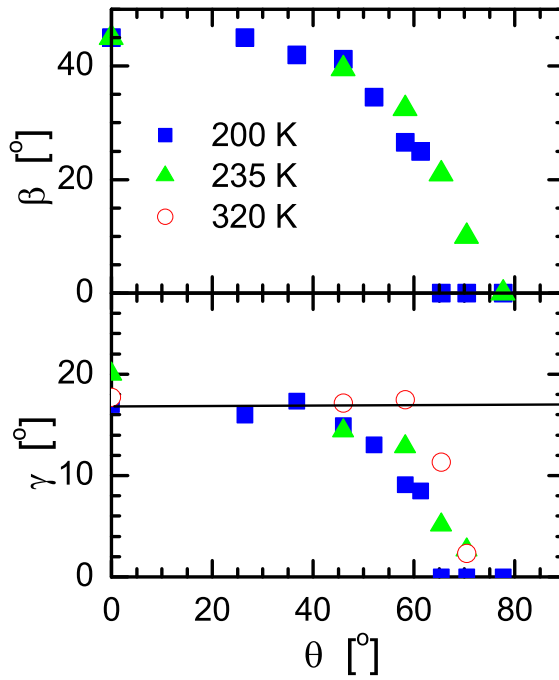


Figure 3.12: The angles  $\beta$  and  $\gamma$  as defined in Fig. 3.9 as a function of the sputter angle for 200, 235 and 320K.



## 3.6 Sputtering along [100]

Figure 3.13 shows specular beam profiles representing the created etch structures with the ion beam incident along the  $\langle 100 \rangle$  azimuth at various polar angles of incidence. The angles of the facet peaks with respect to the (001) surface associated with the various discernible spots are given. At a polar angle of incidence of  $30^\circ$ , both the facet peak originating from the shadow side and from the illuminated side are visible. The latter is clearly no longer visible at  $49^\circ$ . At  $61^\circ$  spots along the [010] direction become visible, while the strong spot along the [100] direction starts to move towards the center. The latter is no longer visible beyond  $70^\circ$ . At first it would seem that a stripe pattern develops similar to glancing incidence bombardment induced features along the [110] azimuth. These latter measurements show a striped pattern with only 3 atomic layers involved [65, 99]. In contrast however, changing the electron energy for both the measurements at  $73^\circ$  and  $78^\circ$  results in a movement of the diffraction spots, indicating the evolution of quite well defined facets in the [010] direction of the otherwise 1D structure. The occurrence of these facets already indicates that more than 3 layers are involved in this pattern, as confirmed by I-V measurements of the specular spot. A further increase of the incidence angle shows that above about  $80^\circ$  a stripe pattern without facets in the [010] direction is observed. Under these conditions the position of the peaks do not depend on the electron energy and therefore relate to the distance between the stripes.

The facet angles are steeper for the [100] azimuth compared to sputtering along the [110] azimuth. A maximum of  $27^\circ$  is observed in the [100] direction for sputtering at  $49^\circ$ . This implies a stronger roughening of the surface when not sputtered along the close packed direction. A further increase of the ion's polar angle of incidence leads

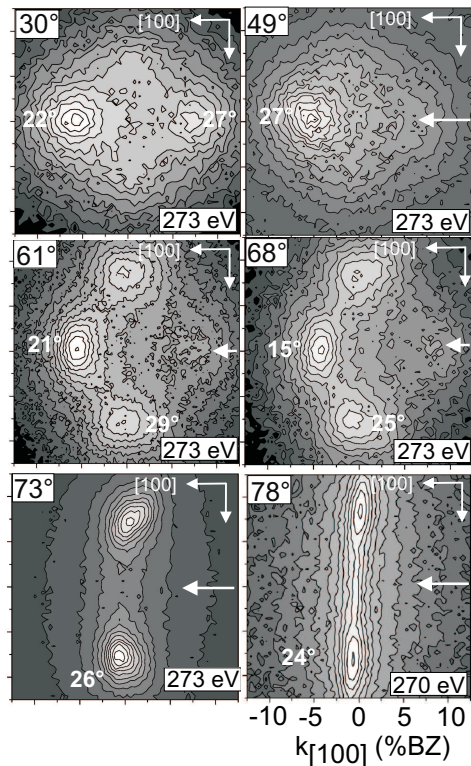


Figure 3.13: SPA-LEED contour plots of the specular beam acquired after  $\text{Ar}^+$  sputtering of 20 ML Cu at 235K along the [100] azimuth for the indicated polar angles of incidence. The peak profiles have been obtained at the indicated electron energies. The angles represent the orientation of the facets they relate to, with respect to the (001) surface. The incident ions impinge from right to left (white arrows).

again to better defined etch structures.

## 3.7 Conclusion

In conclusion, we have investigated the shape of the vacancy islands on Cu(001) as the result of ion bombardment induced erosion under kinetic limitations. The derived favorable step directions allow conclusions about relative step motions rates. This information has been derived from application of a well known rule, relating the presence of persisting step (facet) orientations to the lowest advancement (growth) rates. During the initial etching stages (up to 0.5 ML) the close packed  $\langle 110 \rangle$  ledges dominate. As soon as the surface is roughened to a stage at which interlayer diffusion becomes significant, the advancement rate of the  $\langle 100 \rangle$  steps is reduced due to the site selective descent of adatoms. Under kinetic erosion conditions the  $\langle 100 \rangle$  advancement rate tends to be slowed down below that of the close packed  $\langle 110 \rangle$  ledges which is attributed to preferential descence of atoms across  $\langle 100 \rangle$  ledges as compared to  $\langle 110 \rangle$  one's. As a result  $\langle 100 \rangle$  ledges then dominate the surface morphology. We emphasize that on Cu(001), even at temperatures as low as room temperature, annealing can be unexpectedly fast, leading to dramatical changes of the surface morphology. Therefore, one may be easily misled by measured scanning probe images obtained under these conditions.

We have also studied the dependence of the morphology of the roughened surface on the polar angle of incidence. At both (near) normal incidence and for polar angles up to  $\approx 70^\circ$ , Bradley and Harper predicted the formation of a stripe pattern [48]. The orientation of the ripples was shown to depend on the polar angle of incidence, confirmed by several groups [41, 52, 83]. In our experiments, we do not observe such ripples near normal incidence, let alone an orientation

of these ripples perpendicular to the sputter plane of incidence. At polar angles in the range of  $50-70^\circ$  one might be tempted to interpret the elongated erosion structures observed as the precursor of the ripple structure. Above  $\approx 80^\circ$  ion reflection plays a very dominant role leading to a well defined stripe pattern. However, the development of this pattern can certainly not be interpreted along the lines of the Bradley Harper model, as was also indicated by them. A prominent characteristic of this well defined stripe pattern is that it consists of shallow nanogrooves of only 2 atomic layers deep. It is essentially a surface confined, 2D, structure. The height of the nanogrooves does not enlarge with time as one expects and observed for the 2D ripple structure described by Bradley and Harper.

Two reasons for the failure of describing the present experiments at polar angles below  $\approx 70^\circ$  can be given. First of all, the morphologies studied after ion erosion are obtained after only a moderate ion fluence compared to studies where ripple patterns are observed with typically a 1000 times larger flux and a 100 times larger fluence. However, the much smaller fluence itself can not explain the differences. A detailed study of the erosion of a Pt(111) surface by Kalff et al. [93] in which 30 times more material was removed compared to our experiment still showed no indication of the formation of a ripple pattern. Instead, the morphology of the eroded structures still reflect the symmetry of the (111) surface and is regarded to be the result of the various diffusion processes active on the surface.

The observation of the remaining fourfold morphology on Cu(001) for a wide range of polar incidence angles and the sixfold symmetry observed on Pt(111)[93] after extensive erosion points towards the second reason for the failure of the Bradley Harper model, the crystalline nature of the substrate. At the combination of temperature and flux used in these experiments, no amorphisation of the substrate

occurs. This implies that a multitude of diffusion processes occurs on the surface that are not contained in the continuous description of the Bradley Harper model. The complexity of this is highlighted by the observation of the temperature dependent erosion structures observed at normal incidence for Cu(001). The continuous description of the evolution of the surface morphology with a ripple structure as a consequence will be valid if the crystalline nature of the substrate does not play a role. Amorphisation of the outer region of a substrate, as observed for non-metal substrates, or the use of an amorphous substrate from the start thus seems a prerequisite for the observation of the ions polar angle dependent orientation of the ripple structure.



# Creation and temporal evolution of ripples on Cu(001)

## 4.1 Introduction

Self organisation provides an efficient route for the homogeneous creation of nanostructures on macroscopic surfaces. During controlled ion bombardment self organisation leads to very regular patterns with nanometer dimensions. These can be composed of either 0D or 1D structures, i.e. dots or lines. Highly regular dot structures in a hexagonal pattern were reported the last few years by several groups [3, 59, 87]. The creation of ripple structures by ion bombardment has been known for some more years, including the ripple orientation dependency on the angle of incidence of the ion beam. This dependency was first explained by Bradley and Harper [48] (BH). Bradley and Harper provided a continuum theory that describes the height evolution of the surface in terms of competing processes. The ion beam induces roughness due to a higher sputter efficiency in valleys, while diffusion processes smoothens corrugations. The effect of the

ion impact on a corrugated surface was described in earlier work by Sigmund [49]. The effect of surface self-diffusion has been extensively studied by considering the coarsening of rough surfaces starting with Mullins [51, 101]. BH showed that the combination of these two effects explains the incidence angle dependent observation of ripple structures. Their continuum approach has been extensively modified by especially Barabási and coworkers [52, 55, 102] in order to explain experimental observations like the saturation of both the ripple amplitude and wavelength. The ion beam induced ripples were shown to occur in many different materials, ranging from oxides to crystalline metals and their wavelength can be set between 100 - 1000nm. The kinetics of ripple formation and the coarsening of ripples were very recently studied for Cu(001) by light scattering [103]. These experiments showed the influence of temperature, ion flux and azimuthal orientation of the crystal on the amplitude and the wavelength of the created ripples. The observed coarsening was attributed attachment detachment limited kinetics.

Ripples with a much shorter wavelength were reported after ion bombardment on Ag(110) [9], Cu(110) [10, 104] and Cu(001) [65, 99]. The smaller length scale in these experiments is due to the relatively low substrate temperature during ion sputtering. The ripples on both (110) surfaces were analyzed in terms of the continuum equation introduced by BH. This theory explained the observed dependence of the ripple orientation on both the polar and azimuthal ion incidence angle. However, not only the ripple amplitude, but also the wavelength of the ripples was found to change with sputter time. The coarsening of such ripples on Ag(110) was studied to observe the temporal behavior of the amplitude of 1D ripples limited by detachment kinetics [105]. Very different ripples, denoted as nanogrooves, were created on Cu(001) through ion bombardment by Van Dijken



[65, 99]. These ripples were created at grazing incidence (polar angle of  $80^\circ$ ). The wavelength of these nanogrooves was shown to depend on temperature and ion energy, but their height remained only 2 layers deep. Also a larger wavelength was reported for sputtering along [100] compared to sputtering along [110] at elevated temperatures [99], indicative of a strong azimuth dependence of the ripple pattern. The conditions under which these patterns were created, i.e. grazing incidence sputtering, imply an ion erosion process very different from that used in the continuum theory for sputtering, i.e., in Sigmund's sputter model [49]. The sputter yield on the terrace and at an ascending step edge are very different at this grazing incidence angle, as discussed in [65] and recently reported also in [61]. Also the crystalline nature of the material leads to a large variety of relevant material transport processes on the surface that will determine the morphology. This has been very clearly illustrated by the observed variation in morphology upon sputtering at normal incidence [88].

In this chapter we report on a systematic study of ripple formation through mild grazing incidence sputtering of the Cu(001) surface. The observed temporal evolution of these ripples can not be explained within present continuum models: The ripple amplitude remains similar, while the ripple wavelength increases with sputter time. Both aspects are in contrast with Barabási's model. Sputtering along [100] resulted in a much larger distance between nanogrooves as compared to sputtering along  $[1\bar{1}0]$  for a given sputter time at temperatures of 235K and above. Also a clear saturation of this distance is observed for sputtering along [100]. Coarsening of these nanogrooves points to detachment processes that are responsible for the increase of the ripple wavelength with time.

## 4.2 Experimental

Our method of choice to characterize the morphology of surfaces is high-resolution low energy electron diffraction (SPA-LEED), with a resolution of  $\sim 0.1\%$  of the Brillouin Zone (BZ). All experiments have been conducted in ultra-high vacuum (pressure  $< 10^{-10}$  mbar). Our Cu(001)-surface, was prepared anew before each experiment by 30 minutes of 800 eV Ar<sup>+</sup> ion sputtering and subsequent annealing up to 800K for 5 minutes. Initially, the surface was checked with Auger electron spectroscopy after several sputter-anneal cycles. After the impurities were below the detection limit of Auger, a subsequent sputtering at 800K has been performed until the FWHM of the (0,0)-beam in SPA-LEED was  $\sim 0.3 - 0.4 \%$  BZ. This corresponds to an average terrace starting width of about 80 nm.

Ripple structures were obtained after sputtering with an Ar<sup>+</sup> ion flux of either  $1.5 \cdot 10^{16}$  ions  $\text{m}^{-2}\text{s}^{-1}$  or  $5 \cdot 10^{16}$  ions  $\text{m}^{-2}\text{s}^{-1}$ , denoted as "low" and "high" flux sputtering, respectively. The substrate temperature is always quenched to about 100K immediately after switching off the etching ion beam, to minimize possible disturbing annealing effects.

## 4.3 Results

### 4.3.1 Ripples along [110]

Upon bombarding the Cu(001) surface with an Ar<sup>+</sup> ion beam with an energy of 800 eV at grazing incidence ( $80^\circ$  from the surface normal) a well defined array of parallel ripples is formed [65, 99]. These ripples are aligned parallel to the plane of incidence of the ion beam. The distance between the ripples and their ordering can be determined

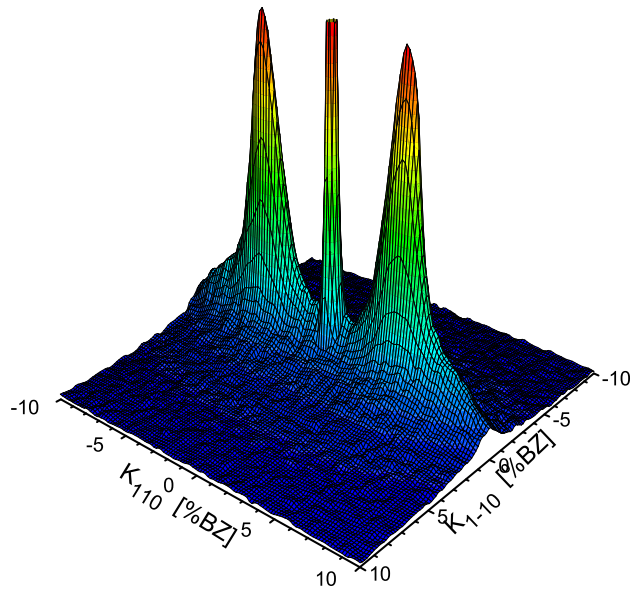


Figure 4.1: Diffraction profile around the specular reflected electron beam after  $Ar^+$  ion bombarding the Cu(001) surface for 2h at 235K along  $[1\bar{1}0]$ . The electron energy was 275 eV and the ion flux was  $1.5 \cdot 10^{16}$  ions  $m^{-2}s^{-1}$ .

from an electron diffraction profile as shown in Fig. 4.1 obtained after sputtering for 2h at a sample temperature of 235K. The ion flux was  $1.5 \cdot 10^{16}$  ions  $\text{m}^{-2}\text{s}^{-1}$  and the ion beam was aligned along the  $[\bar{1}\bar{1}0]$  azimuth. The width of the specularly reflected beam along the  $[\bar{1}\bar{1}0]$  direction, i.e., parallel with the ion beam, has hardly increased compared to the initially flat surface. This indicates that the average length of the ripples is of the same order as the initial mean terrace width on the surface, i.e. 80 nm.

The electron energy dependence of diffraction line scans through the specular spot along the  $[110]$  azimuth is shown in Fig. 4.2a. In this contourplot, the intensity as a function of the parallel wave vector  $k_{110}$  and the perpendicular scattering vector  $S_z$  is shown. The scattering factor  $S_z$  is defined by  $S_z=2d_{001}/\lambda$ , where  $d_{001}$  is the spacing between the atomic planes normal to  $(001)$  and  $\lambda$  the electron wavelength. The image thus shows the diffraction features around the 5<sup>th</sup> in-phase scattering condition. The  $S_z$  independence of the features at 3.5% BZ clearly shows that they are related to periodic 2D-structures at the surface and are not the result of 3D-structures or facets. The height of the parallel ripples can be estimated from recording the intensity variation as a function of  $S_z$  of the specularly reflected electron beam. Within the limits of the kinematic approximation, the FWHM of the peaks near integer  $S_z$  inversely proportional to the height of the structures on the surface [106, 107]. For the homoepitaxial growth at 250K, it is well established that one monolayer high islands are obtained, i.e. a system with only two layers exposed. This is used as a calibration, depicted by the solid line in Fig. 4.2b and gives a FWHM,  $\Delta S_z=0.20$ . The FWHM of the intensity variation of the specular beam of the surface with ripples is  $\Delta S_z=0.10$ , a reduction by a factor 2. This suggests most probably that only 3 layers are involved, i.e. the grooves are only 2 atomic layers deep. Also shown is the intensity

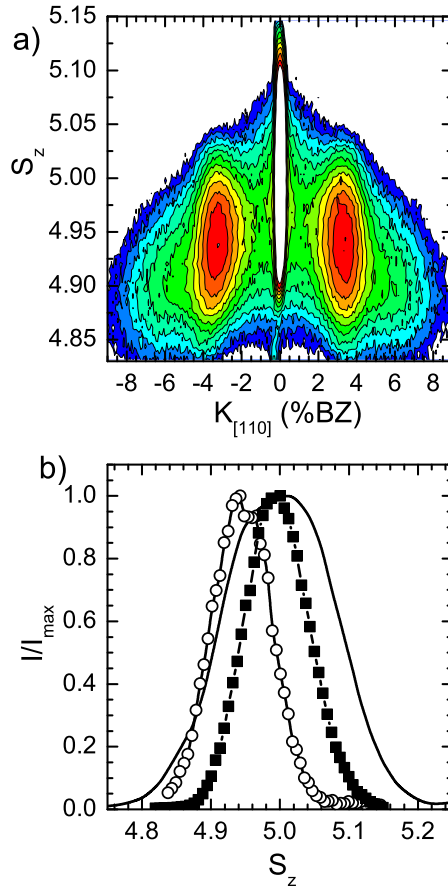


Figure 4.2: a) Contourplot of the diffraction intensity as a function of the parallel and perpendicular wavevector,  $k_{||}$  and  $S_z$  after sputtering along  $[1\bar{1}0]$  for 2h at 235K. b) Normalized intensity as a function of the perpendicular wavevector  $S_z$  after 0.5 ML of homoepitaxial growth on Cu(001) at 250K (solid line), of the specular beam of the profile shown in a) (filled squares) and for the side peak at 3.5% BZ (circles).

variation of the first order diffraction feature, which is directly related to the presence of the ripples. The FWHM of  $\Delta S_z=0.11$  is similar to the one obtained for the specular beam. Sputtering with a flux of  $1.5 \cdot 10^{16}$  ions  $\text{m}^{-2}\text{s}^{-1}$  always resulted in structures with a FWHM of the specular beam around  $\Delta S_z=0.10$ .

The roughness of the surface can also be determined along the route outlined by Yang et al. [79, 80]. The diffuse part of the scattered intensity in one Brillouin zone is considered to be related to the rms roughness  $w$  of the surface (see also chapter 2). The ripples obtained after sputtering also give sharp first order diffraction features. However, in Yang et al. [79, 80] treatment of diffraction through the height-height correlation function, this would not lead to a change in the diffuse part, but rather involve a redistribution of the intensity in the diffracted Bragg peaks. In LEED experiments both energy and incidence / exit angle influence the measured intensity [80]. However, through normalisation of the intensity in this procedure and by considering only small angle variations, such contributions should be negligible. The ratio of the diffuse intensity  $I_{diff}$  and the total intensity  $I_{total}$ , integrated over the Brillouin zone containing the specularly reflected beam as a function of the scattering factor  $S_z$  then gives the roughness related parameter  $\Omega$ :

$$\frac{I_{diff}(S_z)}{I_{total}(S_z)} = 1 - \exp^{-\Omega(S_z)} \quad (4.1)$$

with

$$\sqrt{\Omega} = \pi \frac{w}{d_{001}} S_z \quad (4.2)$$

Figure 4.3 shows the dependence of  $\Omega$  on  $S_z$  after sputtering for

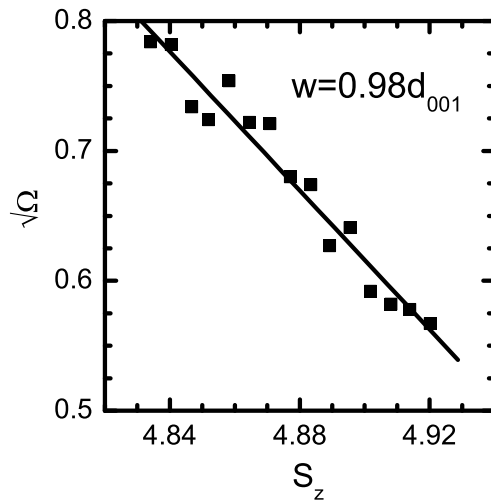


Figure 4.3: Ratio of the diffuse intensity to the total intensity scattered in the Brillouin zone of the specular beam expressed in the value  $\sqrt{\Omega}$  as a function of  $S_z$ . The line is a fit providing the roughness  $w$  in units of  $d_{001}$ .

1h at 235K along  $[1\bar{1}0]$  and the value of  $w$  is determined as  $1 \cdot d_{001} \cong 1.8\text{\AA}$ . This value corresponds well to ripples that are 2 atomic layers deep and occupy half the substrate surface, similar to the previous observation. Also for prolonged sputtering the roughness remains at this value.

The wavelength of the ripples was shown to increase with both the sample temperature and ion energy [65, 99]. However, as we show here, also the ion fluence influences the separation distance. Figure 4.4 shows the temporal behavior of the ripple wavelength  $L$  as evaluated at the indicated temperatures from electron diffraction profiles. Van Dijken et al. [65, 99] showed that diffraction line scans recorded along the  $[1\bar{1}0]$  direction obtained after 1h sputtering at various temperatures scale with respect to each other. This implies that the first order diffraction peaks of linescans obtained at various temperatures coincide perfectly if the parallel wavevector and intensity are multiplied by appropriate numbers. We found that this property also holds for ripples obtained with varying fluence, i.e. we observed scaling behaviour for profiles recorded after sputtering at 235K for 0.5 to 4h. Note that in the temperature range considered here thermal fluctuations of the steps should have led to strongly differing distribution [108]. The wavelengths observed after various sputtering times at different temperatures are thus the result of kinetic processes and not of thermodynamic origin [65].

For low temperatures  $L$  is almost constant in time, while the increase of  $L$  with sputter time at room temperature is about 3 nm/h. Initially, linear increase of  $L$  with time is observed for all temperatures:

$$L(T) = L_0(T) + S(T) \times t \quad (4.3)$$

with  $S(T)$  the rate with which  $L$  increases with time and  $L_0(T)$  the initial wavelength obtained from extrapolating to the start of bom-



barding of the flat surface. Do note that it takes about 10 min. sputtering before a noticeable diffraction feature different from the flat surface can be observed. This diffraction pattern in the early stages already shows the signature of the parallel ripples. The temperature dependence of both  $L_0$  and  $S$  are shown in Fig. 4.5. The temperature dependence of these two parameters is quite similar. Also the distance between adatom islands after growth of 0.5 monolayer of Cu is shown [109, 110] for comparison. In the temperature range from 230 - 275K, the change of  $L_0$  with temperature is quite similar for the creation of the grooves and nuclei in homoepitaxial growth. In homoepitaxy, the energy barrier in this temperature range is determined by adatom diffusion. In the initial sputter phase  $L_0$  is determined by both the diffusion of adatoms and vacancies, which have similar diffusion energies. Below 200K, no temperature dependence is found, the separation rate remains at about 0.4 nm/h and the initial separation distance is 5 nm. These latter values are interpreted as the result of the energy transfer between impinging ions and the surface. This energy transfer results in a locally enhanced "surface temperature" exactly around the position of the ion impact. This local heating effect is strongly supported by the observed linear increase of  $L$  with ion energy [65, 99] in their temperature range. However, their suggestion that below 200K the distance between grooves does not depend on ion flux or fluence can not be sustained. More elaborate measurements between 200K and 175K show a small but non-vanishing value of  $S$ . Above 275K a marked difference in  $L_0$  between sputtering and homoepitaxy is observed. A much smaller effective energy barrier seems to occur in case of sputtering, resulting in a relatively larger distance between initial vacancy islands. The separation rate  $S$  increases even more strongly at higher temperatures.

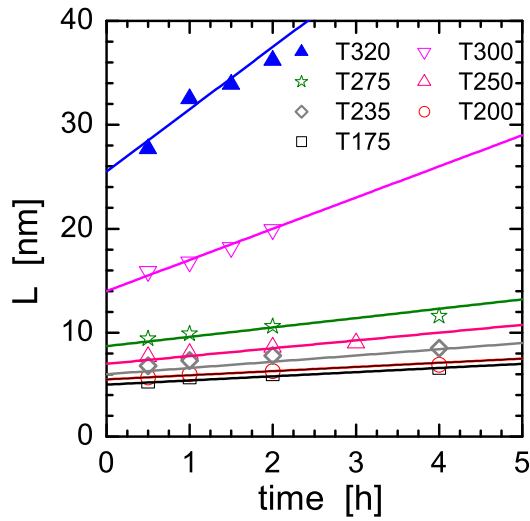


Figure 4.4: Ripple wavelength  $L$  after grazing incidence ion bombardment along  $[1\bar{1}0]$  as a function of sputter time for the indicated temperatures. The lines are a fit of eq. 4.3

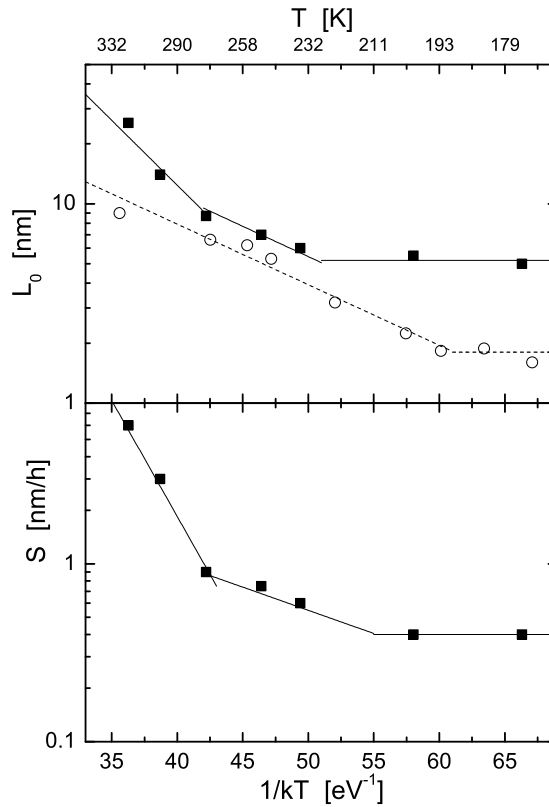


Figure 4.5: Temperature dependence of the initial wavelength  $L_0$  and the rate of increase of the wavelength  $S$  (squares). Also shown is the distance between adatom islands as recorded for 0.5 monolayer of Cu on Cu(001) (open circles) from ref. [109, 110]

### 4.3.2 Scenario

A scenario for the evolution of the regular arrays of parallel linear and shallow grooves was introduced by Van Dijken et al. [65, 99]. In the first stage, the major part of the grazing incident ions is specularly reflected by the surface without any change in morphology. The reflection occurs through a gradual change in path direction in which the ion skims over the surface for several atomic distances before leaving the near surface region. The Cu surface atoms are as a result of thermal fluctuations at slightly different positions from their average position. The ion observes these fluctuations as a snapshot, i.e. a frozen, slightly corrugated surface and inelastic ion surface collisions become possible [111], i.e. the creation of both isolated vacancies and adatoms, as well as atoms injected in the vacuum [14, 64]. The bulk vacancies will be much closer to the surface compared to the situation at normal incidence. Adatoms created through the same impact or diffusing around after being generated previously, may annihilate the freshly produced monovacancy and part of the vacancy islands. This will result in one monolayer deep square vacancy islands with steps preferentially oriented along  $\langle 110 \rangle$ . This result is similar to submonolayer normal incidence sputtering on Cu(001), although the creation rate of vacancy islands is smaller for grazing incidence sputtering [112]. The average distance between vacancy islands will be set by an interplay between the diffusion of both adatoms and vacancies and their rate of creation. Since diffusion on Cu(001) is intrinsically isotropic, also the radial distribution of vacancy islands is expected to be isotropic.

In phase two, the grazing incident ions approach a previously created vacancy island. The ascending step of this vacancy island in the direction of the ion beam as result provides a comparably large target and receives a relatively high flux for geometric reasons and an

anisotropic enlargement of the vacancy island parallel to the direction of the ion beam occurs. Recently, this much larger sputter yield of the ascending step compared to the terrace at grazing incidence was verified [61]. In phase three a preferential coalescence of vacancy structures parallel to the plane of incidence occurs. Immediately after coalescence the edges of the merged clusters are smoothened efficiently for two reasons. First, the edges of the ripples are smoothened by the continuously incoming ions as protruding illuminated kink atoms are eroded with high preference. Second, thermodynamics tends to reduce a high density of kinks, facilitated by the high mobility of adatoms along  $\langle 110 \rangle$  steps on the fcc(001) surface. In this phase the separation distance between the ripples increases, while their amplitude does not increase.

Only phase three is observed in the experiments presented. The density of structures in phases one and two was found to be not large enough to give a reasonable morphology signal for electron diffraction. Indirectly, phase one can be observed as the density of isotropic islands, and thus  $L_0$  in this scenario, should not depend on the azimuth along which the ion gun is oriented. The mechanisms involved in phase two and especially three might lead to an azimuth dependent temporal behavior.

### 4.3.3 Ripples along [100]

Grazing incidence sputtering along the [100] azimuth also results in a diffraction pattern characteristic for ripples. The ordering is not as perfect as obtained after sputtering along  $[1\bar{1}0]$  since the second order diffraction feature is not visible, see Fig. 4.6 in comparison to Fig. 4.1. Energy dependent line scans along [010] were made, which allowed to assign them to 2D-periodic features in contrast to facets.

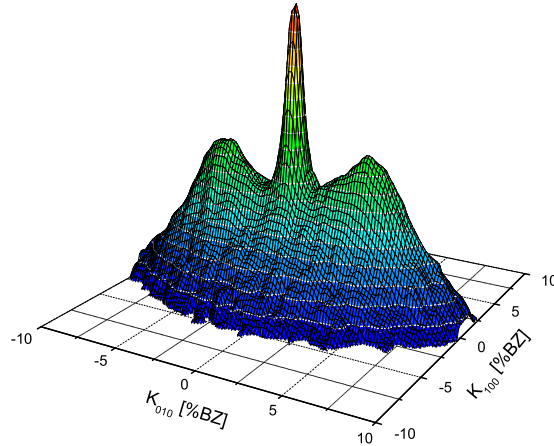


Figure 4.6: Diffraction profile around the specularly reflected electron beam after ion bombardment of the Cu(001) surface for 2h at 235K along [100]. The electron energy was 275 eV.

Figure 4.7 shows a comparison of the temporal evolution of the ripple wavelength  $L$  for sputtering along the [100] and the  $[1\bar{1}0]$  azimuth as evaluated for a sample temperature of 275K . Also for other temperatures in the range 200 - 275K we found comparable similarities and differences between sputtering along the two azimuths:

1. Extrapolation to the start of the ion bombardment gives a similar  $L_0$  at a specific temperature. This findings strongly supports the scenario sketched above.
2. In both cases the ripple wavelength increases with ion fluence.
3. A saturation of the wavelength  $L$  is observed for the [100] az-

imuth within 4h. A linear increase with time is thus not observed.

4. The separation rate of the ripples  $S$  depends on temperature also for sputtering along  $[100]$ . The initial value of  $S$  is at elevated temperatures markedly higher for sputtering along  $[100]$  than along the densely packed  $[1\bar{1}0]$  azimuth. Below 200K, the separation rate is smaller for sputtering along  $[100]$  ( $S_{[1\bar{1}0]} = 0.4$  nm/h versus  $S_{[100]} = 0.3$  nm/h at 200K).
5. The diffraction line scan along  $[010]$  recorded after 4h sputtering, i.e. where saturation of the ripple wavelength is observed, scale with respect to the profiles recorded after short time sputtering. Similar to the scaling observed for sputtering along  $[1\bar{1}0]$ , scaling of the line scans implies that the ratio of the wavelength distribution and the mean wavelength is constant and that also the saturation wavelength is determined by kinetic effects rather than thermodynamics.

#### 4.3.4 Influence of ion flux on the ripple evolution

Increasing the flux to  $5 \cdot 10^{16}$  ions  $\text{m}^{-2}\text{s}^{-1}$  resulted in similar diffraction patterns as the one shown in Fig. 4.1. However, a small difference is observed upon recording the energy dependent line scans for sputtering with higher fluences, as shown in Fig. 4.8a. Similar to the low flux experiments, first order diffraction features are visible indicating a structure of ripples. The intensity variation of the specular beam with  $S_z$  is shown in Fig. 4.8. It shows a slightly smaller FWHM, compared to the low flux situation, replicated from Fig. 4.2b) which amounts to  $\Delta S_z = 0.08$ . For extended sputter times this FWHM

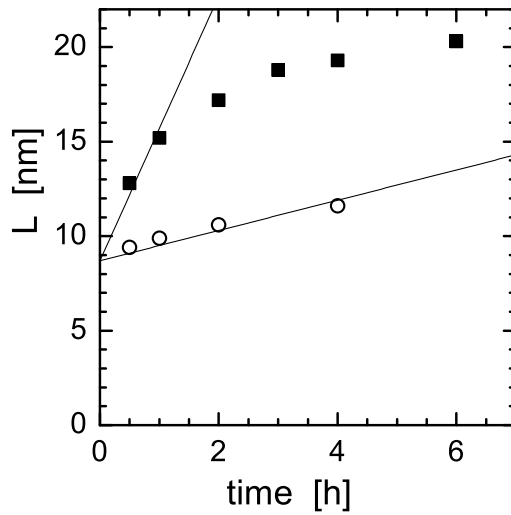


Figure 4.7: Ripple wavelength as a function of sputter time for sputtering along  $[100]$  at 275K (solid squares). Also shown is the result for sputtering along  $[1\bar{1}0]$  (circles) as well as the extrapolation to  $t=0$ .



value becomes smaller and the wings become more pronounced, indicating the formation of facets. The change in  $k_{\parallel}$  of these wing features with variation of  $S_z$  identifies these facets as (113). The higher flux and prolonged sputtering has created deeper ripples, which at first involve four layers, but even increases to five layers for extended sputtering. If four layers are involved in the ripple, the transition from the highest level to the bottom of the ripple can involve two (narrow) terraces. The presence of at least two terraces of similar length is required for observing facets in diffraction. The measurements shown in Fig. 4.8 are characteristic for the "high" flux ( $5 \cdot 10^{16}$  ions  $\text{m}^{-2}\text{s}^{-1}$ ) measurements up to 2h sputtering, with only an onset of facets. The height of these ripples is thus still limited to a few layers.

The temporal evolution of the ripple wavelength for both azimuths for both "high" and "low" flux is shown in Fig. 4.9 at a sample temperature of 235K. This result shows that a higher flux leads to a smaller value of  $L_0$ , which is still similar for both azimuths. This observation is in line with nucleation rate theory [113]. Equivalent to growth, the higher flux leads to a larger density of adatom, respectively vacancy islands. This feature reconfirms the nucleation part of the scenario. The saturation value observed along [100] is indistinguishable for both fluxes. For the  $[1\bar{1}0]$  azimuth the ripple wavelength now deviates markedly from the linear increase with time as suggested by the low flux experiments.

### 4.3.5 Annealing of ripples

The ion flux was shown to have a profound influence on the observed temporal behaviour. However, one may wonder whether the ion beam is a prerequisite for the increase with time of the ripple wavelength. The wavelength of a rippled structure during a mild anneal

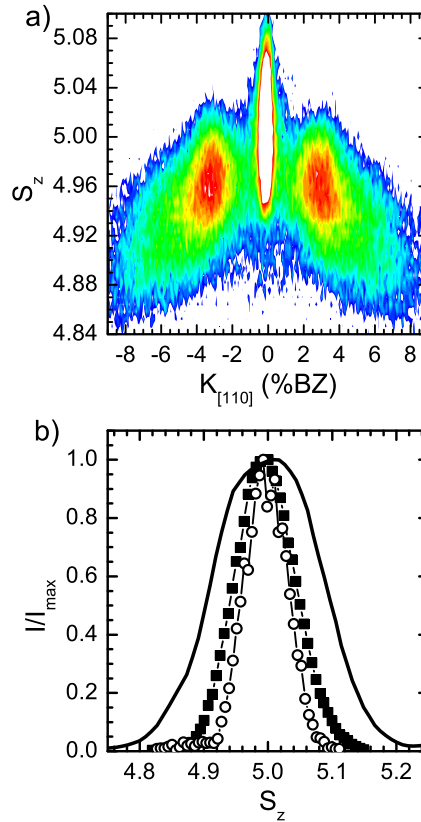


Figure 4.8: a) Contourplot of the diffraction intensity as a function of the parallel and perpendicular wavevector after sputtering along  $[1\bar{1}0]$  for 2h at 235K at 'high' flux. b) Normalized intensity of the specularly reflected beam as a function of the perpendicular wavevector after 0.5 ML of homoepitaxial growth on Cu(001) at 250K (solid line), after "low" flux sputtering (filled squares) and after "high" flux sputtering (circles).

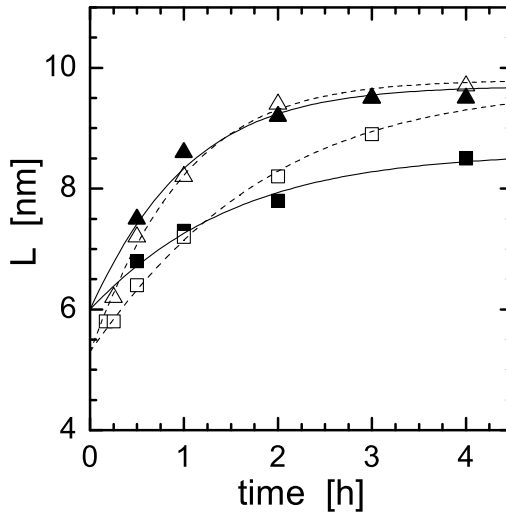


Figure 4.9: Distance between ripples  $L$  as a function of sputter time at a substrate temperature of 235K for a flux of  $1.5 \cdot 10^{16}$  ions  $m^{-2}s^{-1}$  (filled symbols) and  $5 \times 10^{16}$  ions  $m^{-2}s^{-1}$  (open symbols). The sputtering is along  $[1\bar{1}0]$  (square symbols) or  $[100]$  (triangle symbols). The lines are the fits according to eq.4.5.

was therefore investigated. For both ripples created by sputtering at low flux along  $[1\bar{1}0]$  and  $[100]$  for 1h at 235K, the diffraction profiles were recorded while annealing the substrate at 250K, 275K or 290K. Figure 4.10a shows a contourplot of 1D line scans along  $[010]$  during annealing at 250K, created along  $[100]$ . An increase of the specularly reflected intensity is observed (not shown) that indicates an overall smoothening of the surface. Annealing for a substantial time (over 10 min. for ripples oriented along  $[100]$  at this temperature) also results in a gradual deterioration of the ripple structure as noticed by the decrease in intensity of the diffraction side peaks. Before this, the decrease of the diffraction features is hardly noticeable, but a change in ripple wavelength  $L$  occurs. Figure 4.10b shows the diffraction profile before and after annealing for 175 and 350s. The parallel component of the wavevector of the measurements of the annealed substrate were multiplied by 1.06 and 1.10, respectively, to illustrate the self-affine behaviour in the first stage of annealing. A small deterioration in the first stage of the first line scan can be observed in Fig. 4.10a as the sample temperature is increased from 100K to 250K. This temperature change affects the sample alignment and thus influences the parallel wavevector. In subsequent line scans, the sample alignment is corrected automatically by the SPALEED software [81]. From the change in wavelength  $L$  with time as observed in Fig. 4.10 a rate of separation  $S$  of 7 nm/h is evaluated. This value is significantly larger than the one found for the initial rate of separation at 250K during sputtering, which amounts to 2.4 nm/h. The ion sputtering thus not essential for the increase of the wavelength  $L$  with time. Moreover, the annealing experiment suggests that sputtering even slows down the temporal behaviour. At first glance this seems in contrast to the observation that for a higher flux  $S$  is larger.

The annealing of the ripples created by sputtering for 1h at 235K

along  $[1\bar{1}0]$  show a similar increase of  $L$  with time. The separation of these ripples was initially 7.3 nm, quite comparable to the initial 8.5 nm of the ripples created by sputtering along  $[100]$ , used in these annealing experiments. In absence of sputtering the rate of separation as a result of annealing at 250K was 4.7 nm/h. This lower value for the rate of separation, as compared to 7 nm/h for the  $[100]$  case, during annealing for ripples along  $[1\bar{1}0]$  is accompanied by a slower rate of separation during ion sputtering along this azimuth as noted further above. We also note that the ripples created by sputtering along  $[1\bar{1}0]$  are much more anneal resistant. Higher temperatures or prolonged anneal times are required to remove the ripple structure in absence of the ion beam.

## 4.4 Discussion

The experiments presented above provide insight in the temporal evolution of the ripples. Van Dijken et al. [65, 99] limited their study to ripples obtained after sputtering for 1 h at different temperatures. The deconvoluted diffraction profiles were shown to scale to each other, which led to the conclusion that the ripple structure is self-affine. This self-affine property indicates that the process underlying the setting of the wavelength  $L$  is kinetic in origin. Also the diffraction profiles recorded under a variety of circumstances (fluence, flux, temperature and annealing) resulted in a self-affine structure for both azimuths, including those line scans taken after 4h sputtering along the  $[100]$  azimuth, i.e. in the regime where we observed clear saturation behavior. The saturation itself is thus part of the kinetics.

The observed increase of  $L$  during annealing and the scaling of the linescans implies that ripples with a small average size have disintegrated and their mass has been redistributed leading to ripples with

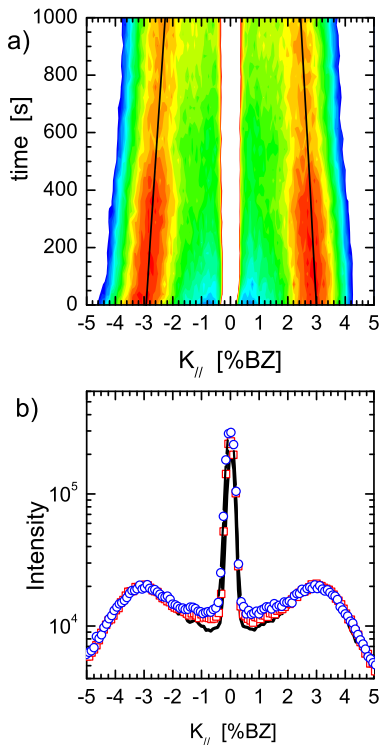


Figure 4.10: a) Sequentially recorded 1D line scans along  $[010]$  and with  $K_{[100]} = 0$  during annealing at 250K of ripples created after 1h low flux sputtering at 235K with the ion beam incident along  $[100]$ . In order to enhance the diffraction features of the ripples, the specularly reflected beam is cut off and shows up as the central white area. b) 1D line scans at the start of the annealing (solid line) and after 175s (squares) and 350s (circles) annealing. The wavevector of the line scans after 175s and 350s are scaled along  $[010]$ , i.e., expanded by factors of 1.06 and 1.1 respectively.

an on average larger wavelength. This implies a massive mass transport across the surface and also that the surviving ripples themselves move across the surface. Such mass transport in absence of the ion beam is at these temperatures only possible due to the creation of both adatoms that traverse the terrace between the ripples as well as through vacancy creation and subsequent diffusion through the high(er) level(s) of ripples. The impact of vacancies in mass transport on Cu(001) was suggested by Hannon et al [114] and several STM experiments have shown the influence of vacancies created at steps [115–117]. The influence of both adatoms and vacancy diffusion on stepped surfaces was considered theoretically by Hare and Roelofs [118]. However, the ripples created in this experiment are markedly different from those on vicinal surfaces. A terrace between two valleys is bound by two ascending steps in contrast to a vicinal surface, where a terrace is bound by both an ascending and a descending step.

The motion of ripples will be first discussed in the absence of the ion beam and we start by considering one atom high ripples. The creation of adatoms on the terrace between two ripples starts with a thermally activated detachment process from one of the edges of the bounding ripples. This detachment from a step edge is a process that requires a relatively high energy compared to diffusion on the terrace of Cu(001) and explains the sharp increase of  $S$  above 275K, see Fig. 4.5. The movement on the terrace itself is a random-walk and the chance that an adatom reaches the opposite ripple decreases strongly with the distance between the ripples. The 1D character of the ripple structure also makes the random-walk process effectively a 1D process, an adatom either reaches the opposite edge or returns to the edge it originated from. The relatively high detachment energy compared to the diffusion energy implies that there is a low density of adatoms on the surface and nucleation of an adatom island is unlikely.

Both bounding step edges of the terrace have the same detachment rate and no net mass flow between the two opposite edges occurs. This process on its own can thus not explain the ripple movement observed. However, the terrace length influences directly the fluctuation of both step edges and the "cross - talk" between them. This fluctuation will scale inversely with the diffusion time on the terrace. The diffusion time on the terrace for this 1D random walk process scales quadratically with the terrace width. For vacancies in the ripples a similar process of the creation of a vacancy and its movement holds. Also in this case no net movement of the ripple will occur just because of the vacancies as the two mass currents from opposite edges cancel, but the fluctuation of the steppedges, i.e. the chance that mass is transported to the opposite edge, will depend on the width of the terrace that facilitates the adatom or vacancy movement. Figure 4.11 illustrates this concept. The movement of both adatoms and vacancies leads to a fluctuation and this provides a net movement of the steppedge. This movement depends on the distance to both next neighbour steppedges. The smaller features denoted as (1) and (2) will rapidly disappear and the number of ripples thus decreases. In our measurement we can not determine the length of the lower and upper terrace separately, but only the average distance  $L$  between ripples.

In reality the ripples are two atoms high and the process is complicated by inter-layer mass transport. However, as these ripples are only two atoms high this only requires a sufficient exchange process between adatoms and vacancies on the intermediate height level. Furthermore residual adatoms on top of the upper terraces and vacancies in the lower terraces between the hills may be present. However, they do not modify the general concept.

The detachment is facilitated by the number of kinks present at the edges of the ripples. For ripples along  $[100]$ , the steppedges are



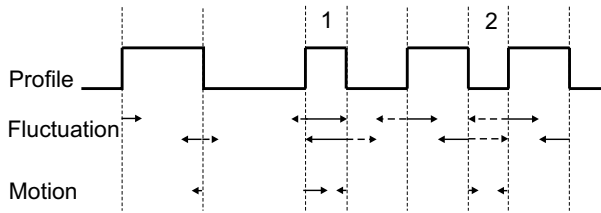


Figure 4.11: Sketch of the movement of the ripple boundaries. Top diagram shows a side view of the ripples. The fluctuation due to adatoms (dashed) and vacancies (solid) on their respective terraces between the ripples and through the ripples are indicated. The strength of the fluctuations is given by the length of the arrow. Below is given the net movement of the step edge.

by definition highly kinked compared to ripples created along [110]. Along [100], the detachment process only involves the breaking of bonds with two next neighbour atoms. Along [110], the steppedge atom is generally bonded by three next neighbours, except for atoms at kinks. Similar argument hold for the generation of vacancies in the high levels. The high kink density is directly reflected in the higher thermally induced separation rate  $S$  observed for ripples along [100]. The distance between two ripples will also influence the observed separation rate  $S$  as the detached material subsequently has to cross the groove and attach to the opposite edge. The specific orientation of the steppedge also explains the more rapid smoothing of ripples created along [100]. The interlayer mass transport is much larger over this step edge compared to [110] step edges [88, 92].

The number of ripples per unit length,  $\#L$ , which is inversely proportional to the average distance between nanogrooves  $L$ , is thus reduced by mass transport at a rate that is proportional to the detachment rate and inversely squared to the present wavelength. The

incident ions will create a new ripple as soon as the distance between two ripples is so large that vacancy islands created by the ions are no longer annihilated at the edges of existing ripples but rather get involved in a new nucleation event. These two ingredients provide a framework for modeling the change in number of ripples per unit length.

$$\begin{aligned}\frac{d(\#L)}{dt} &= -\frac{S}{L^2} + C \\ \frac{dL}{dt} &= S_0 - CL^2\end{aligned}\tag{4.4}$$

In this  $S_0$  is proportional to the rate of detachment processes and  $C$  is the creation probability of new ripples which is assumed to be independent of  $L$ . Without the ion beam, this reduces to  $L = L_0 + S_0t$ , i.e. the observed change of  $L$  for small time scale sputtering and annealing.

A stationary situation occurs when  $S_0 = CL^2$ , i.e. when the distance between ripples has become on average so large that further separation is compensated by the creation of new ripples. This is a competition between two kinetic processes and thus leads to the observed self-affine structures even at the saturation length  $\bar{L} = \sqrt{S_0/C}$ . The apparent higher rate of attachment - detachment processes for ripples along [100] thus also leads to a larger value of  $\bar{L}$ .

The above model leads to a temporal dependence of  $L$  according to

$$L(t) = \bar{L} \frac{\frac{\bar{L}+L_0}{\bar{L}-L_0} - e^{-2S_0t/\bar{L}}}{\frac{\bar{L}+L_0}{\bar{L}-L_0} + e^{-2S_0t/\bar{L}}}\tag{4.5}$$

This relation can be used to describe the data at various temperatures. For sputtering along [100], the strong decoupling of the three parameters allows to obtain fairly accurate values despite the limited

number of datapoints. For sputtering along [110] a linear relation seems to give already a good description of the data for the low flux situation, indicating that a distinction between  $S_0$  and  $\bar{L}$  might not be so simple. For the high flux, also an apparent saturation can be observed. The fit to the ripple separation recorded at 235K for both the high and low flux is depicted in Fig. 4.9. A good description of the temporal evolution of  $L$  is found for all temperatures measured. At 250K,  $S_0$  was found to be 5.5 nm/h, quite close to the value found for annealing, 7 nm/h. The close correspondence of these numbers supports the assumption in our model that ions are not crucial for the increase in wavelength with fluence as observed. The ions facilitate the creation of new ripples and also play a vital role in the shaping of the ripples. Irregularities in the ripple edges are high impact positions for grazing incidence sputtering.

The kinetics of ion-induced ripples on Cu(001) was also recently studied experimentally by Chason and co-workers [103, 119]. They concluded that their ripple structure has the features of a Bradley Harper instability. These ripples were created by 800 eV Ar<sup>+</sup> sputtering at 70° angle of incident with the normal in the temperature range of 415 - 455K and for ion fluxes of 10<sup>18</sup> ions m<sup>-2</sup>s<sup>-1</sup> and similar sputter times. Although it would be tempting to make a direct comparison of their results and the results presented in this work, they are markedly different. First of all the angle of incidence. At an angle of 80°, the shallow ripples are created, while at 70° 1D ripples are only observed for a sample temperatures below 200K [112]. As the incidence angle during sputtering is above the critical angle, these ripples are likely to have a larger amplitude. Above 200K, facets are created both along and perpendicular to the incident ion beam. This is due to the fact that at a polar angle of incidence equal to 80°, total reflection of the ion beam occurs [100], resulting in a larger differ-

ence in sputter yield between terrace and ascending step edge. As already appreciated by Bradley and Harper [48], the different sputter mechanisms at glancing incidence makes their continuum description inapplicable.

A markedly different result between the high and low temperature measurements is the temporal behaviour. We observe that the separation between the ripples  $L$  depends on time, and, certainly for the low flux, the amplitude remains the same. However, above 400K it was found that the wavelength did not depend on time, but instead the amplitude increases. The latter observation complies with the popular BH continuum description of ripples, while the first does not. These differences do point towards a very different temporal regime of the two set of experiments. The low ion flux used in the present experiments leads to a situation that no ripples can be created at temperatures far above 320K. Normal incidence sputtering showed that the annealing effects are so strong at temperatures of 400K and above that no ion induced pattern could be observed [112]. The wavelength in the 400 - 800 nm range of the high temperature measurements is also expected from an extrapolation of the results presented here. The wavelength of nanoripples is rationalized in the extended description of Bradley and Harper theory [48] by Cuerno and Barabási [102]. The wavelength in this description is found to be given by the square root of the ratio of the surface self-diffusion and the flux. The stationary separation between ripples  $\bar{L} = \sqrt{S/C}$  was found to depend in a similar fashion on the ratio of diffusion and sputtering processes.

The similarities between the two sets of experiments makes it tempting to rationalize our experiments in terms of the extended Bradley Harper theory and treat them as the initialisation of ripple formation. However, the Bradley Harper theory considers the change

in roughness  $\partial h/\partial t$  and predicts a constant separation distance. The low flux condition was chosen such that no change in amplitude of the ripples is recorded. The temporal evolution of the rms roughness  $w$  is usually expressed with a critical exponent  $\beta$  in continuum theory, with  $w \propto t^\beta$ . In our measurements  $\beta$  is equal to zero for the time interval studied. Such a value is only achieved when the roughness of an area smaller than the ripple length is considered, as is clearly not the case in our experiments. The observed saturation of  $L$ , cannot be described by a single exponent. This makes it unlikely that the above experimental results can be described within the framework of (initial) ripple formation in (a modified) Bradley Harper theory. In contrast, ripple formation on Cu(110) investigated by Rusponi et al. [104] showed both an increase in ripple wavelength and roughness. They studied the scaling properties of the interface for surfaces with a periodic (mound) morphology. Rusponi et al. followed the surface evolution versus the sputtering time. Ripple structures were obtained after sputtering at grazing incidence  $45^\circ$  and  $70^\circ$  (from the surface normal). The interface roughness  $w$ , defined as the root mean square of the surface height, scales with  $\beta = 0.43$  and  $\beta = 0.20$ , , respectively, and does not saturate.

## 4.5 Conclusion

Grazing incidence sputtering enables the creation of very shallow (2 atomic layers deep) 1D nanostructures on Cu(001) with a wavelength that can be set by controlling the sputter time and temperature, between 5 and 35 nm. The processes on atomic scale that are responsible for the creation of these ripples and the change in wavelength with prolonged sputtering have been identified. The scenario initially proposed by Van Dijken et al. [65, 99] for the creation of these

ripples is supported by the azimuth independent distance between initially created vacancy islands. In further sputtering, the specific azimuth along which the ion beam is aligned determines the rate at which the ripple wavelength changes. This is the direct consequence of the crystalline nature of the substrate surface. The orientation of step edges provide a difference in kink density. The detachment from a kink position is the rate limiting step for the change in wavelength. Moreover, at grazing incidence ions have a very different sputter probability on a flat terraces and for small protrusions. These small protrusions in the form of a step are preferentially removed. This effect leads to an excellent definition of the ripple pattern that counters smoothening diffusion processes. The diffusion of both vacancies and atoms is responsible for the increase in wavelength with time. In the absence of the ion beam this increase is even larger, but also the interface roughness decreases. The ion beam assures a constant creation of new starting points for ripples and thus counterbalances the observed increase in wavelength. The ratio of the diffusion and the creation of new ripples thus eventually leads to a balanced situation that is observed as a saturation of the ripple wavelength.

# Nanogrooves enabled reconstruction on Cu(001)

## 5.1 Introduction

The creation of a surface requires the breaking of atomic bonds. The resulting lower coordination number makes the surface atoms strive for smaller inter-atomic distances as noted first by Pauling [120]. This induces in general an inward relaxation of the exposed layer and considerable tensile in-plane stress. Needs [121] calculated the tensile stresses for Al-metal surfaces as high as  $\sim 10$  GPa! Dodson [122] performed thin slab calculations for the (001)-surfaces of Ni, Ag, Cu, Pd, Au and Pt. He obtained a surface strain of several percents, increasing from Ni to Pt. Indeed, it has been found experimentally [123] that some (001)-surfaces of transition and noble metals do reconstruct. Their termination is a (111)-like overlayer that periodically matches the (001)-bulk structure. The decision whether the (001)-surface does reconstruct or not is quite subtle. The adsorption of small amounts of atoms or molecules can lead to deconstruction

[124, 125]. In an ab-initio density-functional-theory study Fiorentini et al. [126, 127] investigated the tendency for (001)-transition metal surfaces to reconstruct. They find that surfaces of the metals at the end of the 5d transition series such as Ir, Pt and Au reconstruct, whereas their 4d counterparts Rh, Pd and Ag do not. Reconstruction requires bond rearrangements, leading to significant energy losses due to the disruption or stretching of bonds between the mismatched layer and that underneath. The reconstruction results from a delicate balance between surface substrate mismatch and strain related energy gain [126, 127]. Their high strain energy favors reconstruction for the 5d (001) – surfaces, while it is too small for their 4d and 3d counterparts. The surfaces of the 3d and 4d metals remain unreconstructed in agreement with experimental observations.

The claim by Müller et al. [128] of an in-plane reconstruction of clean Cu (001) created a sensation. They found a contraction of about 1% from their LEED IV-analysis. Their finding provided a nice framework for the contraction of 1% found for the pseudomorphic growth of Fe/Cu(001) [129–131]. The Cu(001) in-plane reconstruction was challenged both experimentally [132, 133] and theoretically [134]. Müller et al. [135] conceded and attributed their findings to either a ‘lower lateral crystallinity’ of their surface or ‘systematic errors affecting the accuracy of their analysis’. In a later LEED-IV-study Walter et al. [136] indeed obtained smaller in-plane relaxation by introducing an energy dependent inner potential.

We find experimental evidence for a new local minimum in the free energy of Cu(001). Indeed Cu(001) has a strong tendency for an in-plane lattice contraction of 1%. It only prevails on surfaces with a finite amount of steps, when oriented along the  $\langle 100 \rangle$ -azimuth. Note that  $\langle 100 \rangle$  is the soft direction with respect to deformation [137]. This geometry permits to relieve tensile stress.



This result is of general importance to the 3d and 4d (001)-metal surfaces with implications for the creation of nanostructures on or in these surfaces and the structure of hetero-epitaxial islands.

Our method of choice to characterize the morphology of surfaces is high-resolution low energy electron diffraction (SPA-LEED), with a resolution of  $\sim 0.1\%$  of the Brillouin Zone (BZ). All experiments have been conducted in ultra-high vacuum (pressure  $< 10^{-10}$  mbar). After a standard cleaning procedure, the flat Cu(001) surface has a mean terrace width of 80 nm, as derived from the FWHM of the (0,0)-beam in SPA-LEED. We have extensively looked but in accordance with Refs. [132–134], never found any indication for in-plane lattice reconstruction on the clean and flat Cu(001) surface.

## 5.2 Grazing incidence sputtering

The experiments that led to the observation of an in-plane reconstruction started by bombarding the Cu(001) surface at a selected temperature with 800 eV Ar<sup>+</sup> ions at a flux of  $2 \cdot 10^{14}$  ions/m<sup>2</sup>s. The polar angle of incidence is 80° and the azimuth direction chosen along [100]. Under these conditions highly regular and only two layer deep nanogrooves are formed, running parallel to the plane of incidence of the ions [138]. The distance between the nanogrooves, or better, the periodicity of the one-dimensional nanopattern, depends on temperature, ion energy, flux and fluence. Figure 5.1 shows typical diffraction features as a function of the parallel wavevector  $k_{\parallel}$  in SPA-LEED and the perpendicular scattering factor  $S_z$  after bombardment with a fluence of about  $5 \cdot 10^{18}$  ions/m<sup>2</sup>. The scattering factor  $S_z$  is defined by  $S_z = 2d_{001}/\lambda$ , where  $d_{001}$  is the spacing between the atom planes normal to (001) and  $\lambda$  the electron wavelength. In these data, obtained with the substrate at 235K, two eye-catching features are visible next to the

dominant specular beam. One feature appears at a  $k_{||}$ -value of about 2.4 % BZ. This feature is related to the periodicity of the nanogroove pattern, corresponding to  $102 \pm 6 \text{ \AA}$ . The other feature emerges at about 1 % BZ, i.e. a periodicity of about 250  $\text{\AA}$ . In similar experiments, performed at 200K and 175K, the nanogroove pattern has a periodicity of about 71 $\text{\AA}$  and 69 $\text{\AA}$ , respectively. In all these cases we observe a feature in the specular beam profile that corresponds to a much larger length scale of  $250 \pm 25 \text{ \AA}$ . Within the accuracy the latter feature coincides with that observed after bombardment at 235K (Fig. 5.1). We emphasize that the persistent feature appears at a fixed, temperature independent  $k_{||}$ -value of 1% BZ, in spite of the clear temperature dependence of the nanogroove periodicity.

The specular beam profile obtained in a completely different experiment is shown in Fig. 5.2. The upper panel shows data measured after bombarding Cu(001) again at 235K (cf Fig. 5.1), but now after a six(!) times smaller fluence (bombardment time 3600 s). The well-developed wings indicate a nanogroove separation of 75  $\text{\AA}$ . Subsequently, the substrate is heated to 290K. The evolution of the surface morphology is illustrated by the specular beam profile in the lower panel of Fig. 5.2, obtained after a 500 s anneal at 290K. The initially clearly visible wings not only decrease in intensity but also move towards the central peak, indicating an increase of the periodicity of the nanogroove pattern. Also the intensity of the main peak increases, demonstrating substantial flattening of the surface. We note that again a small maximum, featuring beside the main peak at  $\Delta k_{||} \sim 1\%$  BZ emerges. This feature is persistent and its position does not depend on the annealing time. It remains present even after leaving the sample at 290K for as long as 10.000 s! Annealing of the initial structures at 250K and at 270K leads to a similar appearance of small peaks, corresponding to 250  $\text{\AA}$ .

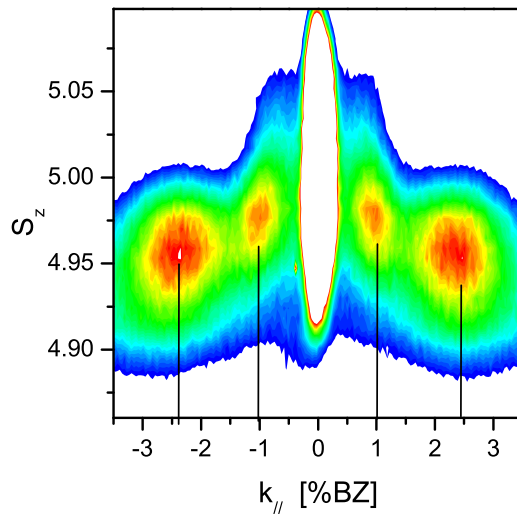


Figure 5.1: Plot of the specular beam profile along the  $[010]$  azimuth after 21600s sputtering at 235K for perpendicular scattering factor  $S_z$  between 4.92 and 5.10. Note that the intensity of the  $(0,0)$  spot is cut off (shown as white) in order to enhance the diffraction features.

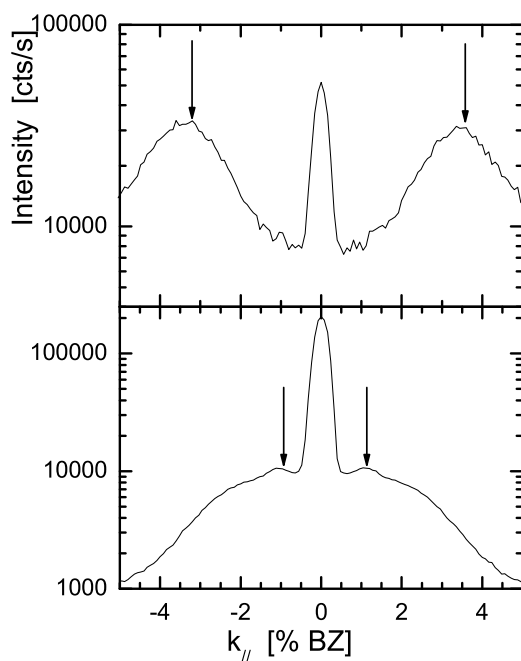


Figure 5.2: SPALeED profile along [010] after sputtering for 3600s at 235K (top) and subsequent annealing at 290K for 500s (bottom).

The experiments described above show a very persistent feature indeed emerging at  $\Delta k_{\parallel} \sim 1\%$  BZ. It corresponds to a length scale of  $250 \pm 25 \text{ \AA}$  along  $[010]$ , i.e. normal to the nanogrooves. Its appearance is independent of the substantially varying thermal history. The diffraction feature does not change its position even at temperatures with many diffusion processes active on the surface. These combined observations demonstrate a thermodynamic origin of this feature.

The observations indicate an in-plane contraction of the lattice parameter of 1%. This phenomenon agrees with the calculated tensile stress of (001)-faces of 3d, 4d and 5d metals [122, 126, 127]. The reconstruction results from a delicate balance between surface-substrate mismatch and strain release [126, 127, 134]. We agree and reiterate that this balance does argue against reconstruction for smooth Cu(001), with Cu being a 3d-metal. However, the actual situation obtained after bombarding the Cu(001) sample at grazing incidence along  $[100]$  deviates from this ideal situation. We stress that satellites are observed only along the  $[010]$ - azimuth but not along  $[100]$ . Instead of an isotropic in-plane surface plane contraction, the striped pattern only allows *uni-axial in-plane* contraction normal to the grooves. The easier accommodation of lattice misfits in the presence of atomic steps was predicted theoretically by Van der Merwe [139].

### 5.3 A first layer reconstruction

In all situations of relevance here, the distance between the nanogrooves is substantially smaller than 100 atomic spacings. The upper level of atoms in a nanogroove structure can relax without the need for the incorporation of additional dislocations. We elaborate now on the uniaxial in-plane contraction a bit further by considering a one-

dimensional model. Following van der Merwe [66, 67, 140], the periodic first-layer atom-substrate potential is approximated by a truncated Fourier series with an amplitude  $W$ . The underlying 1D substrate is assumed completely rigid. The lateral interaction in the first layer is modeled with springs, with a constant  $\gamma$ . The potential energy of a chain of  $N$  atoms, following the notation of Markov [141] is then given by

$$E = \frac{\gamma a^2}{2} \sum_{n=0}^{N-2} (\xi_{n+1} - \xi_n - f)^2 + \frac{W}{2} \sum_{n=0}^{N-1} [1 - \cos(2\pi\xi_n)] \quad (5.1)$$

This model is known as the one-dimensional version of the Frenkel-Kontorova (FK) ball and spring model [142], as depicted in Fig. 5.3. This model has been studied extensively and exact solutions for various situations have been derived [66, 67, 143, 144]. The one-dimensional Frenkel-Kontorova model consists of a linear chain of atoms, subject to two competing interactions with different intrinsic periodicities. The atoms interact via a nearest-neighbor harmonic coupling with a preferred lattice constant  $b$ . In addition, there is an external periodic potential i.e., the potential of the second atomic layer with a bulk periodicity  $a$ . The lattice misfit between the first layer and the substrate is given by  $f = (b - a)/a$ . In the formulation of the FK model in eq. 5.1,  $\xi_n$  is the relative position of the  $n^{\text{th}}$  first layer atom with respect to the minimum of the potential well in units of  $a$ . The first term in the energy balance accounts for residual strain due to the different spacing between the first layer atoms and  $b$ . The last term reflects the energy cost due to the misfit between the first layer and the substrate. The full energy minimum results then in a variation of the parallel lattice constant for the first layer atoms. In this case, the chain runs in the [010] azimuth, i.e. perpendicular to the

grooves. Depending on the strength of the external potential and the magnitude of the spring constant  $\gamma$ , various stable solutions are possible. At only a small difference of  $a$  and  $b$ , and a relative small value of  $\gamma$ , the external periodic potential dominates and all atoms are in potential minima, forming a commensurate phase. At a large difference between  $a$  and  $b$ , the natural periodicity of the atomic chain becomes important. If the external potential is weak compared with the elastic energy needed to stretch the atomic chain, the atoms follow the periodicity  $b$ , forming an incommensurate phase. The Frenkel-Kontorova model is a very crude representation of the real surface. We only use the model in one dimension as we do not observe structural changes parallel to the nanogrooves. The surface region is also treated as a single layer. The interaction modelling between surface atoms and the substrate through a sine wave external potential with strength  $W$  is also quite crude. Accurate values for the quantity  $W$  are not available, but it mimics the energy difference between a Cu atom in the fourfold hollow site and in the on-top position. From this picture, we estimate that  $W=0.8$  eV, about twice the activation energy for diffusion over the bridge site [145].

The positions of the atoms in the first layer are calculated from the derivative of the potential energy  $E$  with respect to all displacements  $\xi_n$ , providing the force acting on the  $n^{th}$  atom. At equilibrium this force is equal to zero and  $dE/d\xi_n = 0$ . Minimizing Eq.5.1 with respect to  $\xi_n$  leads to the following set of recurrent equations:

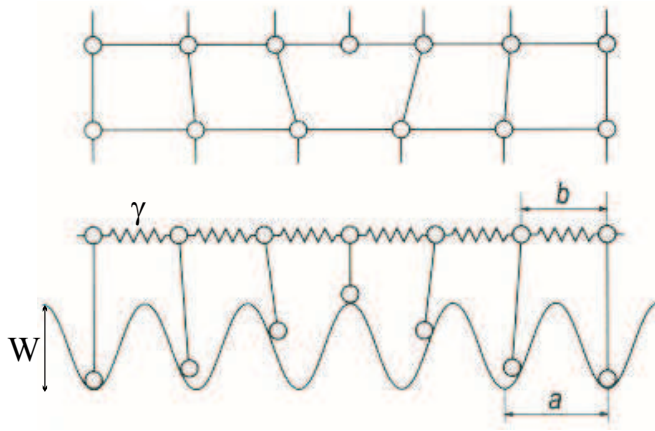


Figure 5.3: Schematic presentation of a chain of particles (atoms), interacting via harmonic springs with the elastic constant  $\gamma$  and subjected to an external sinusoidal potential.

$$\begin{aligned}
 \xi_1 - \xi_0 - f &= \frac{\pi}{2l_0^2} \cdot \sin 2\pi\xi_0 \\
 \xi_{n+1} - 2\xi_n + \xi_{n-1} &= \frac{\pi}{2l_0^2} \cdot \sin 2\pi\xi_n \\
 \xi_{N-1} - \xi_{N-2} - f &= \frac{\pi}{2l_0^2} \cdot \sin 2\pi\xi_{N-1}
 \end{aligned}
 \tag{5.2}$$

where

$$l_0 = \sqrt{\frac{\gamma a^2}{2W}}
 \tag{5.3}$$

is a parameter which accounts for the ratio of the forces between strain and incorporation in the fourfold hollow site. The equations 5.2 are usually rewritten in the form of the Sine-Gordon equation, allowing analytic solutions [141]. However, we are dealing with a



nanogroove of a fixed width and the usual continuous boundary conditions can no longer be applied. For a chain of  $N$  atoms, eq. 5.2 can be solved numerically by reformulating the problem to an iterative problem, eq. 5.4. A better solution  $\xi_n^{j+1}$  is derived from a previous solution  $\xi_n^j$  until a stable solution is derived.

$$\begin{bmatrix} -1 - \left(\frac{\pi}{l_0}\right)^2 \cos(2\pi\xi_0^j) & 1 & 0 & 0 & 0 \\ \cdots & \cdots & \cdots & \cdots & \cdots \\ 0 & 1 & -2 - \left(\frac{\pi}{l_0}\right)^2 \cos(2\pi\xi_n) & 1 & 0 \\ \cdots & \cdots & \cdots & \cdots & \cdots \\ 0 & 0 & 0 & 1 & -1 - \left(\frac{\pi}{l_0}\right)^2 \cos(2\pi\xi_{N-1}^j) \end{bmatrix} \begin{bmatrix} \xi_0^{j+1} \\ \cdots \\ \xi_n^{j+1} \\ \cdots \\ \xi_{N-1}^{j+1} \end{bmatrix} = \begin{bmatrix} f + \xi_0^j - \xi_1^j + \frac{\pi}{2l_0^2} \sin(2\pi\xi_0^j) \\ \cdots \\ 2\xi_n^j - \xi_{n-1}^j - \xi_{n+1}^j + \frac{\pi}{2l_0^2} \sin(2\pi\xi_n^j) \\ \cdots \\ \xi_{N-1}^j - \xi_{N-2}^j - f + \frac{\pi}{2l_0^2} \sin(2\pi\xi_{N-1}^j) \end{bmatrix} \quad (5.4)$$

The pseudomorphic solution is used for the start values,  $\xi_n^0 = 0$  in the iteration scheme, as these start values should not be too far from the stable solution. Figure 5.4 shows solutions to this difference scheme for a chain of 80 atoms. The two extreme situations leading to a pseudomorphic layer and a strain relaxed layer due to strong neighbour bonds is shown.

The total energy of the 1D chains as a function of chain length is shown in Fig. 5.5. The pseudomorphic situation results in a linear increase of the total energy, while the fully relaxed phase has for small chain lengths only a small increase in energy. The value of  $\gamma$  used in these calculations is obtained by comparing the difference in energy between a pseudomorphic layer and the relaxed 1D chain. First principles calculations by Fiorentini et al. [126, 127, 134] of an 1% uniaxially contracted toplayer on Cu(001) show an energy gain that amounts to 1.12eV. They did not incorporate in this energy the energy required for the creation of dislocations, i.e. necessary to let a smooth surface reconstruct [126, 127]. As they argued, this disloca-

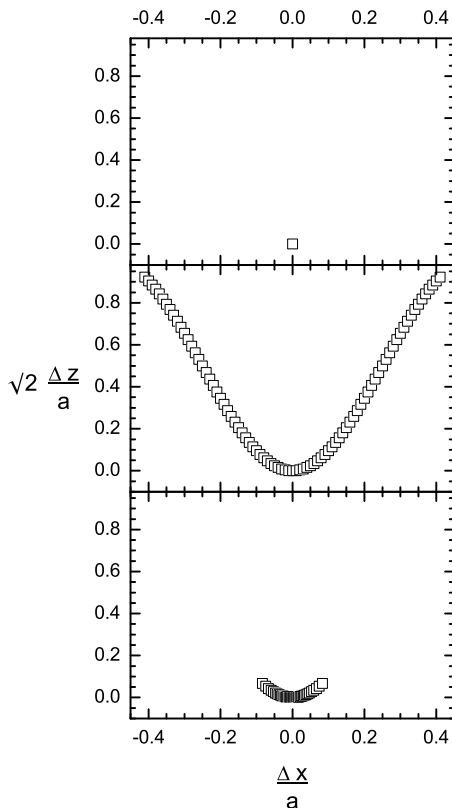


Figure 5.4: Atom positions for a chain of 80 atoms in the Frenkel-Kontorova model. The positions are given by their relative height and the difference in actual position with respect to the substrate lattice position,  $\xi_n$ . Shown are solutions for a) pseudomorphic situation with  $\gamma = 0$  showing all the atoms in the fourfold hollow sites. b) strain free situation and c) the solution that minimizes the energy for a one dimensional chain on Cu(001).

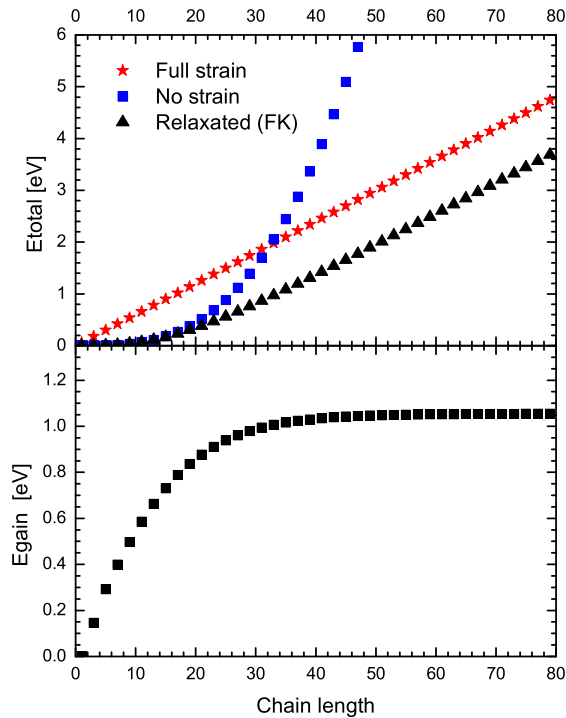


Figure 5.5: (Top) Total energy of the 1D chain on a Cu(001) surface as a function of the chain length. Depicted are the situations for a pseudomorphic layer (Full strain (asterisks)), a relaxed layer with strong lateral interaction (relaxed (triangles)) and the relaxed minimum energy 1D chain on Cu(001) (No strain (squares)). (Bottom) Difference in total energy between the pseudomorphic layer and the relaxed minimum energy 1D chain.

tion energy clearly outweighs the strain relief energy, assuring that no reconstruction of the intact surface is observed [134]. However, the starting situation in our experiments is not the smooth but rather the nanogrooved surface. Their energy difference can thus be used to evaluate the gain in energy between the pseudomorphic and relaxed chain. This gives  $\gamma = 185\text{eV}/\text{\AA}^2$  or 0.06 eV per atom for a 1% strained chain.

The limited chain results in a situation in which the system can fully profit from the energy gain predicted by the Frenkel-Kontorova expression and the numbers quoted above: the presence of atomic steps on the surface allows local in-plane contraction. This holds even more if, as in our case, the steps alternate from step-down to step-up. The atoms on the higher of the two levels will lock in around the minimum energy positions and the unfavourable positions are not occupied. This effect can be seen in Fig. 5.4. Most of the atoms for the chain of length 80 concentrate in the pseudomorphic position, leading to a minority that is in a strain relaxed position. The number of atoms in the latter position are the outer approximately 20 atoms in the chain, as can be derived from Fig. 5.5, i.e. the chain length beyond which the increase in energy of the chain is similar to the pseudomorphic situation.

The morphology of the real nanogrooved surface is quite complex, even within a simple two-level model in which only the upper level is reconstructed. To obtain insight in the resulting beam profile we have simulated two basic cases with different characteristics. To mimic the effect of corrugation we have calculated the diffraction profile obtained from a chain of 100 atoms, their lateral positions on bulk lattice positions and the vertical positions varying as a cosine with amplitude  $a\sqrt{2}$ , i.e. approximately the fully relaxed layer. The chain is positioned on a 1D bulk crystal. The diffraction has been

calculated using the kinematic approximation and an electron mean free path of 0.8 nm. This results in strong symmetric features at 1%, with a FWHM corresponding to the instrumental resolution, see Fig. 5.6 (dashed line). Note that a height variation of the atoms leads to the observation of a lateral periodicity. In accordance with the Frenkel-Kontorova model (Eq.5.1), both the lateral and height position of part of the first layer atoms deviate from the bulk position. This dispersion was also simulated within the same framework (solid line). The dispersion in lateral position leads to a strongly reduced feature compared to the intensity of the (0,0) beam. This intensity reduction can simply be explained by the fact that the effective height distribution of the atoms is narrower, see also Fig. 5.4. Additional calculations for various fractions occupied by the upper level (coverage), varying from 10 to 50%, show a small but strongly persistent spectral density at 1 % of the first Brillouin Zone. This spectral density remains rather constant with coverage. The latter can be understood easily: For ‘low’ coverage the atoms can fully relax and still remain quite near to the bottom of the potential wells. The effective upper layer lattice distance is then close to  $0.99 a$ . For “high” coverage the situation is similar to the relaxed long chain length shown in Fig. 5.4 and, as discussed above, approximately 20 atoms are in a strain relaxed position with a height position different from the pseudomorphic one. In the latter case the density at 1% BZ is mainly caused by the intrinsic length scale of  $100 a$  of the corrugation profile of part of the chain. The reduced number of atoms in this different height position compared to the cosine height chain also reduces the intensity considerable, in line with the experimental observation.

We note that Stepanyuk et al. [146, 147] have calculated in-plane (and out-of-plane) relaxation of lattice parameters near the edges of two-dimensional close packed adatom islands. In-plane contractions

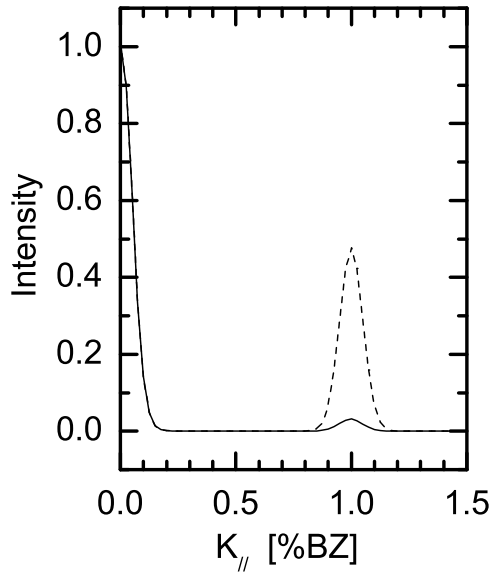


Figure 5.6: Simulated diffraction intensity at  $S_Z = 4.97$  of an atomic chain that only shows a height variation (dashed line) and an additional variation in lateral interatomic distance according to the Frenkel-Kontorova model (solid line). The calculated results have been convoluted with the instrumental response function.

in the order of also 1% have been obtained, the actual value being dependent on the size of the islands. We note that our stable diffraction feature at  $\sim 1\%$  BZ has a distinctly different origin. Neither its position nor its magnitude do depend on the size of the structures.

Van der Merwe and Kunert [148] also predicted that relieve of the misfit energy facilitated by atomic steps does depend on their orientation. We also confirm this result experimentally. We observe the feature at  $\Delta k_{\parallel} = 1\%$  BZ only after bombarding the surface along  $\langle 100 \rangle$ . Bombarding along the  $\langle 110 \rangle$  azimuth does never lead to additional diffraction features. Relieving tensile stress is thus facilitated by pre-existing  $\langle 100 \rangle$  and not by  $\langle 110 \rangle$  oriented steps. This observation is rationalized in terms of anisotropic elastic properties of the Cu(001) surface. Calculations by Ozolins et al [137] show that  $\langle 100 \rangle$  is the soft direction with regard to lattice deformation. In contrast, the  $\langle 111 \rangle$  and the  $\langle 110 \rangle$  directions are hard directions.

From the width of the diffraction patterns along the grooves, we estimate the average length of the grooves at several hundred Å. Reconstruction parallel to the grooves would thus involve accommodation of a much higher mismatch energy. We also note that relaxation of tensile stress normal to the grooves poses a *local* minimum of the free energy. A relatively mild anneal at 400K is sufficient to overcome the energy barrier separating the local minimum from the global free energy minimum leading to extended smooth (001) terraces.

## 5.4 Conclusion

In conclusion, we have observed an in-plane lattice parameter that is 1% smaller than the bulk lattice parameter. This is due to the relieve of the tensile stress inherent to (001)-surfaces of metals. The

reconstruction, not observed for macroscopic (001)-terraces, is enabled by the presence of  $\langle 100 \rangle$  oriented atomic steps and not by  $\langle 110 \rangle$ -steps. This is attributed to anisotropic resistance against elastic deformations. The local free energy minimum, associated with the in-plane lattice contraction, is separated from the global one, leading to unreconstructed Cu(001) surface, by a relatively low energy barrier, which can be overcome by a mild anneal at 400K. Our results reconcile quite recent controversies in literature. They are considered important for the delicate interplay between mismatch and tensile stress energies on fcc (001) metal surfaces in general.





## Bibliography

- [1] Y. Q. Cai, A. M. Bradshaw, Q. Guo, and D. W. Goodman, *Surf. Sci.* **399**, L357 (1998).
- [2] T. Lopez Rios, D. Mendoza, F. J. Garcia Vidal, J. Sanchez Dehesa, and B. Pannetier, *Phys. Rev. Lett.* **81**, 665 (1998).
- [3] S. Facsko et al., *Science* **285**, 1551 (1999).
- [4] N. Ueda, K. Sudoh, L. I. Nan, T. Yoshinobu, and H. Iwasaki, *Jap. J. Appl. Phys.* **38**, 5236 (1999).
- [5] K. Wilder, C. F. Quate, D. Adderton, R. Bernstein, and V. Elings, *Appl. Phys. Lett.* **73**, 2527 (1998).
- [6] H. Brune, *Surf. Sci. Rep.* **31**, 121 (1998).
- [7] K. Bromann, H. Brune, H. Roder, and K. Kern, *Phys. Rev. Lett.* **75**, 677 (1995).
- [8] Z. Zhang and M. G. Lagally, *Science* **276**, 377 (1997).
- [9] S. Rusponi, C. Boragno, and U. Valbusa, *Phys. Rev. Lett.* **78**, 2795 (1997).

- [10] S. Rusponi, G. Costantini, C. Boragno, and U. Valbusa, *Phys. Rev. Lett.* **81**, 2735 (1998).
- [11] A. Levandovsky and L. Golubovic, *Phys. Rev. B* **69**, 241402 (2004).
- [12] C. Teichert, C. Ammer, and M. Klaua, *Phys. Stat. Sol. A* **146**, 223 (1994).
- [13] P. Sigmund, *Phys. Rev.* **184**, 383 (1969).
- [14] T. Michely and C. Teichert, *Phys. Rev. B* **50**, 11156 (1994).
- [15] G. Costantini, S. Rusponi, R. Gianotti, C. Boragno, and U. Valbusa, *Surf. Sci.* **416**, 245 (1998).
- [16] A. Eklund, J. Bruinsma, R. Rudnick, and R. Williams, *Phys. Rev. Lett.* **67**, 1759 (1991).
- [17] E. Eklund, E. Snyder, and R. Williams, *Surf. Sci.* **285**, 157 (1993).
- [18] J. Krim, I. Heyvaert, C. Van-Haesendonck, and Y. Bruynseraede, *Phys. Rev. Lett.* **70**, 57 (1993).
- [19] H.-N. Yang, G.-C. Wang, and T.-M. Lu, *Phys. Rev. B* **50**, 7635 (1994).
- [20] S. X. Wang, R. J. Pechman, and J. Weaver, *Surf. Sci.* **364**, L511 (1996).
- [21] D.-M. Smilgies, P. Eng, E. Landemark, and M. Nielsen, *Surf. Sci.* **377**, 1038 (1997).
- [22] A.-T. Chan and G.-C. Wang, *Surf. Sci.* **414**, 17 (1998).

- [23] P. Konarski and M. Hautala, *Vacuum* **47**, 1111 (1996).
- [24] Z. Csahok, Z. Farkas, M. Menyhard, G. Gergely, and C. Daroczi, *Surf. Sci.* **364**, L600 (1996).
- [25] A. L. Barabási and H. Stanley, *Fractal Concepts in Surface Growth*, Cambridge University Press, Cambridge, 1995.
- [26] D. Barber, F. Frank, M. Moss, J. Steeds, and I. Tsong, *J. Mater. Sci.* **8**, 1030 (1973).
- [27] F. Vasiliu, I. Teodorescu, and F. Glodeanu, *J. Mater. Sci.* **10**, 399 (1975).
- [28] R. Behrisch, *Sputtering by Particle Bombardment Vol. II*, Springer-Verlag Berlin, 1983.
- [29] F. Stevie, P. Kahora, D. Simons, and P. Chi, *J. Vac. Sci. Tech.* **A6**, 76 (1988).
- [30] A. Karen, K. Okuno, F. Soeda, and A. Ishitani, *J. Vac. Sci. Technol.* **A4**, 2247 (1991).
- [31] A. Karen, Y. Nakagawa, M. Hatada, K. Okuno, and A. Soeda, F. Ishitani, *Surf. Interf. Anal.* **23**, 506 (1995).
- [32] K. Wittmaack, *J. Vac. Sci. Technol.* **A8**, 2246 (1990).
- [33] S. MacLaren, J. Baker, N. Finnegan, and C. Loxton, *J. Vac. Sci. Technol.* **A10**, 468 (1992).
- [34] C. Umbach, R. Headrick, B. Cooper, J. Balkely, and E. Chason, *Bull. Am. Phys. Soc.* **44** (1), 706 (1999).
- [35] G. Carter and V. Vishnyakov, *Phys. Rev. B* **54**, 17647 (1996).

- [36] E. Chason, T. Mayer, B. Kellerman, D. McIlroy, and A. Howard, *Phys. Rev. Lett.* **72**, 3040 (1994).
- [37] T. Mayer, E. Chason, and A. Howard, *J. Appl. Phys.* **76**, 1633 (1994).
- [38] E. Chason, T. Mayer, and B. Kellerman, *Mat. Res. Soc. Symp. Proc.* **396**, 143 (1996).
- [39] J. Vajo, R. Doty, and E.-H. Cirlin, *J. Vac. Sci. Technol.* **A14**, 2709 (1996).
- [40] J. D. Erlebacher, M. J. Aziz, E. Chason, M. B. Sinclair, and J. A. Floro, *Phys. Rev. Lett.* **82**, 2330 (1999).
- [41] E. Chason, J. D. Erlebacher, M. J. Aziz, J. A. Floro, and M. B. Sinclair, *Nucl. Instrum. Methods Phys. Res. B* **178**, 55 (2001).
- [42] K. Elst, W. Vandervorst, J. Alay, J. Snauwaert, and L. Hellemans, *J. Vac. Sci. Technol.* **A11**, 1968 (1993).
- [43] K. Elst and W. Vandervorst, *Vac. Sci. Technol.* **A12**, 3205 (1994).
- [44] H. Shichi, K. Ohnishi, and S. Nomura, *Jpn. J. Appl. Phys.* **30**, L927 (1991).
- [45] S. Rusponi, C. Boragno, and U. Valbusa, *Phys. Rev. Lett.* **78**, 2795 (1996).
- [46] E.-H. Cirlin, J. Vajo, R. Doty, and T. Hasenberg, *J. Vac. Sci. Technol.* **A9**, 1395 (1991).
- [47] E.-H. Cirlin, *Thin Solid Films* **220**, 197 (1992).

- [48] R. M. Bradley and J. M. E. Harper, *J. Vac. Sci. Technol. A* **6**, 2390 (1988).
- [49] P. Sigmund, *J. Mater. Sci.* **73**, 1545 (1973).
- [50] C. Herring, *J. Appl. Phys.* 21 (1950) 301 **21**, 301 (1950).
- [51] W. W. Mullins, *J. Appl. Phys.* **28**, 333 (1957).
- [52] M. A. Makeev, R. Cuerno, and A. L. Barabási, *Nucl. Instrum. Methods Phys. Res. B* **197**, 185 (2002).
- [53] T. Aste and U. Valbusa, *New Journal of Physics* **7**, 122 (2005).
- [54] M. Rost and J. Krug, *Phys. Rev. Lett.* 75 (1995) 3894 **75**, 3894 (1995).
- [55] S. Park, B. Kahng, H. Jeong, and A. L. Barabási, *Phys. Rev. Lett.* **83**, 3486 (1999).
- [56] Y. Kuramoto and T. Tsuzuki, *Prog. Theor. Phys.* 55 (1977) 356; **55**, 356 (1977).
- [57] G. Sivashinsky, *Acta Astronaut.* **6**, 569 (79).
- [58] M. Kardar, G. Parisi, and Y.-C. Zhang, *Phys. Rev. Lett.* **56**, 889 (1986).
- [59] S. Facsko, H. Kurz, and T. Dekorsy, *Phys. Rev. B* **63**, 165329 (2001).
- [60] M. Strobel, K. H. Heinig, and T. Michely, *Surf. Sci.* **486**, 136 (2001).
- [61] H. Hansen, C. Polop, M. Michely, A. Friedrich, and H. M. Urbassek, *Phys. Rev. Lett.* **92**, 246106 (2004).

- [62] C. Busse, H. Hansen, U. Linke, and T. Michely, Phys. Rev. Lett. **85**, 326 (2000).
- [63] C. Busse, C. Engin, H. Hansen, U. Linke, and T. Michely, Surf. Sci. **488**, 346 (2001).
- [64] G. Costantini, F. Buatier de Mongeot, C. Boragno, and U. Valbusa, Phys. Rev. Lett. **86**, 838 (2001).
- [65] S. van Dijken, D. de Bruin, and B. Poelsema, Phys. Rev. Lett. **86**, 4608 (2001).
- [66] F. C. Frank and J. H. van der Merwe, Proc. R. Soc. London, Ser. A **198**, 205 (1949).
- [67] F. C. Frank and J. H. van der Merwe, Proc. R. Soc. London, Ser. A **198**, 216 (1949).
- [68] J. Pendry, *Low Energy Electron Diffraction*, Academic Press, London, 1974.
- [69] M. van Hove and S. Y. Tong, *Surface Crystallography by LEED*, Springer, Berlin, 1979.
- [70] M. Horn-vonHoegen, Z. Kristallogr. **214**, 1 (1999).
- [71] J. Cowley, *Diffraction Physics*, North-Holland, Amsterdam, 1981.
- [72] M. Henzler, Appl. Phys. **9**, 11 (1976).
- [73] M. Henzler, Appl. Phys. **A 34**, 205 (1984).
- [74] J. Houston and R. Park, Surf. Sci. **21**, 209 (1970).
- [75] J. Houston and R. Park, Surf. Sci. **26**, 169 (1971).

- [76] J. Wollschlager, J. Falta, and M. Henzler, *Applied Physics A (Solids and Surfaces)* **A50**, 57 (1990).
- [77] A. Myers-Beaghton, *Surf. Sci.* **241**, 439 (1991).
- [78] C. Lent and Cohen, *Surf. Sci.* **139**, 121 (1984).
- [79] H.-N. Yang, T.-M. Lu, and G.-C. Wang, *Phys. Rev. B* **47**, 3911 (1993).
- [80] H.-N. Yang, G.-C. Wang, and T.-M. Lu, *Diffraction from rough surfaces and dynamic growth fronts*, World Scientific, 1993.
- [81] M. Esser, *Kinetically controlled Si-epitaxy on Si(100) and Ge(100)*, PhD thesis, University of Twente, 2001, ISBN 90-365-1641-2.
- [82] G. Comsa, *Surface Science* **81**, 57 (1979).
- [83] R. Gago et al., *Nanotechnology* **13**, 304 (2002).
- [84] J. Kim, B. Kahng, and Barabasi, *Appl. Phys. Lett.* **81**, 3654 (2002).
- [85] T. K. Chini, M. K. Sanyal, and S. R. Bhattacharyya, *Phys. Rev. B* **66**, 153404 (2002).
- [86] C. Teichert, *Appp. Phys. A-Mater. Sci. Process.* **76**, 653 (2003).
- [87] F. Frost and B. Rausenbach, *Appl. Phys. A* **77**, 1 (2003).
- [88] P. Broekmann, A. A. Mewe, H. Wormeester, and B. Poelsema, *Phys Rev. Lett.* **89**, 146102 (2002).
- [89] W. Kleber, *Einführung in die Kristallographie 17th edition*, Verlag Technik GmbH Berlin, 1990.

- [90] T. Michely, M. Hohage, M. Bott, and G. Comsa, Phys. Rev. Lett. **70**, 3943 (1993).
- [91] M. Kalff, G. Comsa, and T. Michely, Phys. Rev. Lett. **81**, 1255 (1998).
- [92] M. Li, J. F. Wendelken, B. G. Liu, E. G. Wang, and Z. Zhang, Phys. Rev. Lett. **86**, 2345 (2001).
- [93] M. Kalff, G. Comsa, and T. Michely, Surf. Sci. **486**, 103 (2001).
- [94] G. Costantini, S. Rusponi, F. Buatier de Mongeot, C. Boragno, and U. Valbusa, J. Phys. Condens. Matter **13**, 5875 (2001).
- [95] T. Michely, M. Kalff, G. Comsa, M. Strobel, and K. H. Heinig, Phys. Rev. Lett. **86**, 2589 (2001).
- [96] J. C. Girard, Y. Samson, S. Gauthier, S. Rousset, and J. Klein, Surf. Sci. **302**, 73 (1994).
- [97] M. Ritter, M. Stindtmann, M. Farle, and K. Baberschke, Surf. Sci. **348**, 243 (1996).
- [98] H. J. Ernst, Surf. Sci. **383**, L755 (1997).
- [99] S. van Dijken, *Pattern formation and magnetic anisotropy in thin metal films*, PhD thesis, University of Twente, 2000, ISBN 90-365-1459-2.
- [100] H. Niehus, W. Heiland, and E. Taglauer, Surf. Sci. Rep. **17**, 213 (1993).
- [101] W. W. Mullins, J. Appl. Phys. **30**, 77 (1959).
- [102] R. Cuerno and A. L. Barabási, Phys. Rev. Lett. **74**, 4746 (1995).



- [103] W. L. Chan, N. Pavenayotin, and E. Chason, *Phys. Rev. B* **69**, 245413 (2004).
- [104] S. Rusponi, G. Costantini, C. Boragno, and U. Valbusa, *Phys. Rev. Lett.* **81**, 4184 (1998).
- [105] L. Pedemonte, G. Braco, C. Boragno, F. Buatier de Mongeot, and U. Valbusa, *Phys. Rev. B* **68**, 115431 (2003).
- [106] M. Horn, U. Gotter, and M. Henzler, *J. Vac. Sci. Technol. B* **6**, 727 (1988).
- [107] R. Altsinger, H. Busch, M. Horn, and M. Henzler, *Surf. Sci.* **200**, 235 (1988).
- [108] E. D. Williams and N. C. Bartelt, *Science* **251**, 393 (1991).
- [109] L. C. Jorritsma, *Growth anisotropy in Cu(001) homoepitaxy*, PhD thesis, University of Twente, 1997, ISBN 90-365-1021-1.
- [110] L. C. Jorritsma, M. Bijmagne, G. Rosenfeld, and B. Poelsema, *Phys. Rev. Lett.* **78**, 911 (1997).
- [111] B. Poelsema, L. K. Verhey, and A. L. Boers, *Surf. Sci.* **55**, 445 (1976).
- [112] A. A. Mewe, M. M. Ovsyanko, P. Broekmann, H. Wormeester, and B. Poelsema, Unpublished.
- [113] J. A. Venables, *Philos. Mag.* **27**, 697 (1973).
- [114] J. B. Hannon et al., *Phys. Rev. Lett.* **79**, 2506 (1997).
- [115] T. Flores, S. Junghans, and M. Wuttig, *Surf. Sci.* **371**, 1 (1997).

- [116] T. Flores, S. Junghans, and M. Wuttig, *Surf. Sci.* **371**, 14 (1997).
- [117] R. van Gastel, E. Somfai, S. van Albada, W. Saarloos, and J. Frenken, *Surf. Sci.* **521**, 10 (2002).
- [118] G. Hare and L. Roelofs, *Surf. Sci.* **511**, 283 (2002).
- [119] V. B. Shenoy et al., *Phys. Rev. Lett.* **92**, 256101 (2004).
- [120] L. Pauling, *The Nature of the Chemical Bond*, Cornell University Press, Ithaca, NY, 1960.
- [121] R. J. Needs, *Phys. Rev. Lett.* **58**, 53 (1987).
- [122] B. W. Dodson, *Phys. Rev. Lett.* **60**, 2288 (1988).
- [123] K. Heinz, G. Schmidt, L. Hammer, and K. Muller, *Phys. Rev. B* **32**, 6214 (1985).
- [124] D. G. Fedak and N. J. Gjostein, *Phys. Rev. Lett.* **16**, 171 (1966).
- [125] C. Romainczyk et al., *Surf. Sci.* **336**, 362 (1995).
- [126] V. Fiorentini, M. Methfessel, and M. Scheffler, *Phys. Rev. Lett.* **71**, 1051 (1993).
- [127] V. Fiorentini, M. Methfessel, and M. Scheffler, *Phys. Rev. Lett.* **81**, 2184 (1998).
- [128] S. Müller et al., *Phys. Rev. Lett.* **75**, 2859 (1995).
- [129] P. Bayer, S. Müller, P. Schmailzl, and K. Heinz, *Phys. Rev. B* **48**, 17611 (1993).
- [130] S. Müller, P. Bayer, A. Kinne, P. Schmailzl, and K. Heinz, *Surf. Sci.* **322**, 21 (1995).

- [131] H. Magnan, D. Chanderis, B. Vilette, O. Hechmann, and J. Lecante, *Phys. Rev. Lett.* **67**, 859 (1991).
- [132] A. P. Baddorf, A. K. Swan, and J. F. Wendelken, *Phys. Rev. Lett* **76**, 3658 (1996).
- [133] K. Robinson, W. Moritz, F. Jona, and M. A. van Hove, *Phys. Rev. Lett.* **76**, 3659 (1996).
- [134] S. Oppo and V. Fiorentini, *Phys. Rev. Lett.* **81**, 4278 (1998).
- [135] S. Müller, M. Kottcke, L. Hammer, and K. Heinz, *Phys. Rev. Lett.* **76**, 3660 (1996).
- [136] S. Walter et al., *Surf. Sci.* **458**, 155 (2000).
- [137] V. Ozolins, C. Wolverton, and A. Zunger, *Appl. Phys. Lett.* **72**, 427 (1998).
- [138] S. van Dijken, G. Di Santo, and B. Poelsema, *Physical Review B (Condensed Matter)* **63**, 104431 (2001).
- [139] J. H. van der Merwe, *Phys. Rev. B* **37**, 2892 (1988).
- [140] J. H. van der Merwe, *Philos. Mag. A* **45**, 145 (1982).
- [141] I. V. Markov, *Crystal growth for beginners*, World Scientific, 1995.
- [142] J. Frenkel and T. Kontorova, *Phys. Z. Sovjetunion* **13**, 1 (1938).
- [143] P. Bak, *Phys. Rev. Lett.* **46**, 791 (1981).
- [144] P. Bak and V. L. Pokrovsky, *Phys. Rev. Lett.* **47**, 958 (1981).
- [145] H. Dürr and J. F. Wendelken, *Surf. Sci.* **328**, L527 (1995).

- [146] O. V. Lysenko, V. S. Stepanyuk, W. Hergert, and J. Kirschner, Phys. Rev. Lett. **89**, 126102 (2002).
- [147] V. S. Stepanyuk, D. I. Bazhanov, W. Hergert, and J. Kirschner, Phys. Rev. B **63**, 153406 (2001).
- [148] J. H. van der Merwe and H. Kunert, Phys. Rev. B **37**, 2902 (1988).

# Summary

In this thesis a comprehensive investigation of low - energy ion bombardment of the (001) surface of copper is presented. The experimental investigations focus on the surface morphology emerging as a result of ion bombardment. It is quantified by average distances and the formation and orientation of facets. These aspects are identified with High Resolution Low Energy Electron Diffraction (HR-LEED). The profile of the reflected electron beam in the vicinity of the specular beam is therefore measured. The influence of temperature and fluence is investigated, and special attention is given to the impact of variations of the angles of incidence of the ion beam, both polar and azimuth. Especially the choice of the polar angle influences dramatically the ion - surface interaction. The nanopatterns emerging as a result of oblique incidence sputtering are described first. At normal incidence, inverse pyramid-like structures are created through sputtering. The orientation of their base, however, depends on temperature. Below 230K, facets with step edges along  $\langle 100 \rangle$  azimuths are observed, while above 300K the facets have step edges along the thermodynamically favorable  $\langle 110 \rangle$  azimuths. It has been verified ex-

perimentally that the facets, with  $\langle 110 \rangle$  oriented steps, are the result of a dramatic rearrangement of the surface as a result of annealing effects during the freeze in period that occurs between the end of sputtering and morphology analysis. The occurrence of kinetically favored facets with step edges along  $\langle 100 \rangle$  azimuths during sputtering at all temperatures is analyzed in terms of well known growth and etching rules for the formation of preferred orientations of 3D crystals under kinetic growth or etching conditions. The application to the 2D situation of this thesis requires a strong orientation dependent interlayer mass transport. This anisotropy in mass transport is readily available as the result of the difference in Ehrlich-Schwoebel barrier associated with  $\langle 100 \rangle$  and  $\langle 110 \rangle$  step edges. Up to almost  $80^\circ$  polar angle of incidence, annealing effects can be observed, highlighting the importance of the multitude of atomic diffusion processes on the Cu(001) surface. This angle of about  $80^\circ$  is determined by the critical angle of incidence beyond which the ions can no longer penetrate the surface. Beyond this critical angle, on a flat surface the sputter yield decreases by orders of magnitude. Also the observed nanopatterns change as a result of this.

In previous research it has been found that grazing incidence sputtering on Cu(001) leads to the creation of very well ordered shallow nanogrooves. A dependence of the wavelength of these grooves on the temperature and azimuth has been found. In this work, also the dependence on the ion fluence is investigated. At first glance a very different temporal evolution of the nanogrooves is observed for sputtering along  $\langle 110 \rangle$  and  $\langle 100 \rangle$  azimuths. Along both azimuths, increase of fluence and temperature leads to an increase of the wavelength. However, sputtering along the  $\langle 100 \rangle$  azimuth shows a much faster increase of the wavelength with fluence and a clear saturation of this wavelength. The influence of both ion beam and temperature on

the increase of the wavelength is investigated by observing the behaviour of a prepared grooved surface in absence of the ion beam. Next to the expected smoothening of the groove structure, also the wavelength still increases with time. Also the thermal stability of grooves is much higher if oriented along  $\langle 110 \rangle$ . The latter is attributed to the inhibited interlayer mass transport over  $\langle 110 \rangle$  step edges, as also observed in the oblique incidence measurements. A model that describes the evolution of the wavelength is proposed. This model is based on the presence of both mobile adatoms and vacancies. Neighboring step edges can thus exchange material and as a result fluctuate in position with time. This fluctuation provides the framework that enables the gradual annihilation of grooves with small wavelengths and thus the creation of grooves with larger wavelengths.

The preparation of nanogrooves along  $\langle 100 \rangle$  results after prolonged sputtering or annealing at several temperatures of grooved patterns created after relative small fluences in the observation of an additional feature in the diffraction pattern. The various preparation routes leading to the same feature point to its of thermodynamic origin. It is explained with the possibility of the nanogrooved surface to relieve the tensile stress inherent to (001)-surfaces of metals. The reconstruction, not observed for macroscopic (001)-terraces, is enabled by the presence of  $\langle 100 \rangle$  oriented atomic steps and not by  $\langle 110 \rangle$  -steps. This is attributed to anisotropic resistance against elastic deformations. The presence of the nanogrooves thus provides a local free energy minimum, associated with an in-plane lattice contraction. It is separated from the global one, observed for the unreconstructed, flat Cu(001) surface, by a relatively low energy barrier. It can be overcome by a mild anneal at 400K. This feature is considered to be important for the delicate interplay between mismatch and tensile stress energies on fcc (001) metal surfaces in general.







# Samenvatting

Dit proefschrift beschrijft een uitgebreid experimenteel onderzoek naar de mogelijkheid om metaaloppervlakken te patroneren via bombardement met laag energetische ionen. Het koper (001)-oppervlak wordt hiervoor representatief geacht. De morfologie van het oppervlak na het ionenbombardement wordt gekarakteriseerd door de gemiddelde afstanden tussen, alsmede de vorming en oriëntatie van facetten. Deze aspecten worden met behulp van Hoge Resolutie Lage Energie Elektronen Diffractie (HR-LEED) geïdentificeerd. Daartoe wordt de intensiteitsverdeling van de bijna spiegelend gereflecteerde elektronen, d.w.z. het profiel van de speculaire bundel, gemeten. De invloed van de substraattemperatuur en de ionendosis op de oppervlakte morfologie zijn onderzocht met speciale aandacht voor de richting van de invallende ionen bundel, zowel polair als azimutaal. Met name de keuze van de polaire invalshoek blijkt een dramatische invloed te hebben op de zich ontwikkelende morfologie. De nanopatronen die ontstaan als gevolg van een scheef invallende ionenbundel worden als eerste beschreven. Bij bombardement met een loodrecht invallende bundel ontstaat een oppervlak dat kan worden omschreven

als bestaande uit omgekeerde piramides. De oriëntatie van hun bases wordt bepaald door de temperatuur van het substraat. Beneden 230K worden facetten waargenomen gevormd door atomaire stappen langs de  $\langle 100 \rangle$  azimut, terwijl boven 300K de atomaire stappen preferentieel langs de thermodynamisch gunstige  $\langle 110 \rangle$  azimut gericht zijn. Het is experimenteel geverifieerd, dat de facetten met  $\langle 110 \rangle$  georiënteerde stap randen het resultaat zijn van een dramatische herschikking van het oppervlak ten gevolge van anneal effecten tijdens de invries periode tussen het einde van het sputterproces en de analyse van de morfologie. De evolutie van kinetisch bepaalde facetten met stapranden langs de  $\langle 100 \rangle$  azimut tijdens sputteren bij alle temperaturen is consistent met de welbekende regels, die het ontstaan van geprefereerde oriëntaties van 3D kristallen onder kinetische groei- en etscondities verbinden met groeisnelheden voor de diverse facetten. Het toepassen van deze regels op de 2D situatie in dit proefschrift vergt een sterke afhankelijkheid van de stap oriëntatie op het transport van adatomen tussen lagen. Deze anisotropie in massa transport wordt verklaard door de veel lagere Ehrlich-Schwoebel barrière, geassocieerd met transport over  $\langle 100 \rangle$  stappen, t.o.v.  $\langle 110 \rangle$  stappen.

Bij het voorgaande onderzoek is tevens gebleken, dat bombardement m.b.v. scherend invallende ionen leidt tot het ontstaan van goed geordende, ondiepe nanogroeven. Dit verschijnsel wordt gerelateerd aan het feit dat boven een kritische polaire hoek, afhankelijk van substraat, ion soort, en - invalrichting (polair en azimuthaal) de overgrote meerderheid van de ionen spiegelen gereflecteerd wordt aan een terras. Dit betekent dat de sputter opbrengst op het terras en aan een opstaande rand sterk verschilt, hetgeen leidt tot een sterke anisotropie van de beschadigingssnelheid. De golflengte van de nanogroeven hangt sterk af van de substraattemperatuur en azimutale richting van het invalsvlak van de ionen. In dit werk is ook de

invloed van de dosis van de ionen op de ontstane structuren onderzocht. Op het eerste gezicht is een zeer verschillende tijdsafhankelijkheid voor de ontwikkeling van de nanogroeven waargenomen voor sputteren langs de  $\langle 110 \rangle$  en  $\langle 100 \rangle$  azimut. Langs beide azimut richtingen leiden zowel een toename van ionen dosis als een hogere substraat temperatuur tot een toename van de golflengte. Sputteren langs de  $\langle 100 \rangle$  azimut vertoont een veel snellere toename van de golflengte met de ionen dosis en een duidelijke verzadiging van deze golflengte. De invloed van zowel ionenbundel als substraat temperatuur op de toename van de golflengte is onderzocht door het bestuderen van het gedrag van een gegroefd oppervlak bij afwezigheid van de ionen bundel. Er wordt een duidelijke toename van de golflengte waargenomen. De thermische stabiliteit van de groeven is duidelijk het hoogst wanneer de stappen langs  $\langle 110 \rangle$  georiënteerd zijn. Ook dit laatste wordt toegeschreven aan de hoge activeringsbarrière voor interlaag massa transport over  $\langle 110 \rangle$  stapranden. Een model voor de evolutie van de golflengte wordt tevens voorgesteld. Dit model is gebaseerd op de aanwezigheid van zowel mobiele adatomen, als vacatures. Naburige stapranden kunnen zodoende materie uitwisselen, wat resulteert in een fluctuatie van hun positie in de tijd. Deze fluctuatie levert een raamwerk voor het begrijpen van een gelijkmatige verdwijning van groeven met korte golflengte, het geen resulteert in het overblijven en ontstaan van groeven met grotere golflengte.

Nanogroeven langs  $\langle 100 \rangle$  ontstaan tijdens sputteren of annealen bij verschillende temperaturen. Hierbij wordt veelal een zwak maar hardnekkig additioneel verschijnsel in het diffractiepatroon rond de gespiegelde bundel waargenomen. Deze kleine piek bevindt zich onveranderlijk op een afstand van circa één procent van de Brillouin zone van het centrum van de (0,0)-piek. Het verschijnsel is grosso modo onafhankelijk van de ontstaansgeschiedenis van het groevenpa-

troon, zelfs na grote verschillen in het afgelegde thermische traject. Dit duidt duidelijk op een thermodynamische oorspong van het additionele diffractieverschijnsel. Het wordt gerelateerd aan een laterale contractie van de bovenste atoomlaag tussen de groeven van 1% ter relaxatie van de inherente trekspanning in de bovenste kristallaag. Deze reconstructie wordt niet waargenomen op macroscopische (001)-oppervlakken en wordt mogelijk gemaakt door de aanwezigheid van  $\langle 100 \rangle$  georiënteerde atomaire stappen. De aanwezigheid van  $\langle 110 \rangle$ -stappen leidt niet tot reconstructie. Dit feit is consistent met de anisotrope weerstand tegen elastische vervormingen op metallische FCC(001)-oppervlakken. De gevonden reconstructie in aanwezigheid van de nanogroeven is het gevolg van een lokaal minimum in de vrije energie. Het globale minimum in de vrije oppervlakte energie voor Cu(001) is gerelateerd aan een grotendeels stapvrij oppervlak zonder rooster contractie in de bovenste laag. De gevonden feiten zijn consistent met eerdere theoretische voorspellingen en worden relevant geacht voor schone en met ultradunne films bedekte FCC(001) metaaloppervlakken.



# Acknowledgements

A dissertation does not just appear out of nowhere, and although it stands as a contribution of one person, it could never have been done without a lot of people who have helped me out over the years. I have been fortunate enough to have had the support of so many people and without it this would not have been possible. While most people did not help directly on the project, every one of them contributed in some way toward helping me to get where I am today, even things like just being a friend and going out and having fun. Others were responsible for giving me a push in the right direction in life, and for everyone listed here I am eternally grateful for their help.

I would like to thank Prof. Dr. Ir. Bene Poelsema, my supervisor and promotor, from whom I have learn not only the scientific knowledge, but also the rigorous academic attitude that will benefit me forever. Time and time again he comments on my notes, corrects my language with patience. I feel lucky to have had the opportunity to work with him. I am deeply grateful to Bene Poelsema for providing an opportunity to work in his group and for his support during my PhD work.

My special thanks go to Dr. Herbert Wormeester for supervising my PhD work, for his attention and patience in guiding my work from the very beginning till writing this manuscript. Without his help and support this work would not have been completed in the way it is. I thank Dr. Cora Salm and Fiona Wormeester for "Herbert's time" that should have belonged to them.

Many people in the Solid State Physics Group have helped to make my work much easier. I would like to thank some of them especially: Herman Oerbekke, Hans Bevers, Geert Mentink and Gerard Kip for providing me with instant help whenever I came with one of my many requests on technical matters, for their support and encouragement.

I am also grateful to Rianne Nales, secretary of Solid State Physics Group, for her prompt help at time-sensitive moments and for general administrative support rendered to me during my research.

I also gratefully acknowledge my colleagues from the Solid State Physics Group: Stefan Kooij, Raoul van Gastel, Robert Ramchal, Harold Zandvliet, Andrei Zinine, Marko Sturm, Ruben Sharpe, Arie van Houselt, Nuri Öncel, Ann-Sofie Hallbäck, Frits Rabbering, Aurelian Galca, Ester van Vroonhoven, Martijn Brouwer, Fawad Khokhar, Jiong Yang, for their support and help and for making the time I spent here so enjoyable and productive. Learning a complex UHV instrument is not a simple thing and Peter Broekmann and Agnes Mewe introduced me to experimenting with the "Kater" and especially the diffraction measurements. The ability to join their project was the key to ion sculpting experiments described in this project. In the later stage, Georgiana Stoian helped as a student in "grooving" the surface. She and Frank van Dijk were also wonderful roommates and I want to thank them for their pleasant company and good friendship. They were always there for me. I would also like to thank former members of Solid State Physics Group: Erwin Zoethout, Mar-

cus Eßer, Ronny van Moere and Oguzhan Gürlü, who helped me in the beginning of my work in The Netherlands.

I want to say thank you to my parents for their believe in me and to all my friends.

Finally, I would like to thank my wife Alla and my daughter Lisa, for their love, support, patience, and understanding they allowed me to spend so much time on this thesis.

*Mikhail Ovsyanko*

December, 2005, Enschede, The Netherlands





# Curriculum Vitae

Mikhail Mikhaylovich Ovsyanko was born in Simferopol, Creamea, Soviet Union, on April 28, 1974.

**September 1989 - June 1991**

Richelieu Lyceum, Odessa, Ukraine

**September 1991 - July 1996**

Student of Physics Faculty of Odessa State University, Ukraine  
Experimental Physics Department (Physics of semiconductors and dielectrics)

**June 1995 - October 1998**

Joint Venture "Everest", Odessa, Ukraine

**November 1998 - July 2000**

Odessa National Polytechnic University, Ukraine  
Theoretical and Experimental Nuclear Physics Group,  
Postgraduate research project: "Multiplicity distribution in in-elastic hadron's interactions at high energies"

**August 2000 - July 2005**

University of Twente, Enschede, The Netherlands

Solid State Physics Group,

PhD research project: "Low dimensional metallic and magnetic structures: composition, structure and properties."

**Since August 2005**

Philips Research Laboratories, Eindhoven, The Netherlands

Department Healthcare Devices & Instrumentation











